



**HAL**  
open science

## Effect of melt/mantle interactions on MORB chemistry at the easternmost Southwest Indian Ridge (61°-67°E)

M. Paquet, M. Cannat, D. Brunelli, C. Hamelin, E. Humler

► **To cite this version:**

M. Paquet, M. Cannat, D. Brunelli, C. Hamelin, E. Humler. Effect of melt/mantle interactions on MORB chemistry at the easternmost Southwest Indian Ridge (61°-67°E). *Geochemistry, Geophysics, Geosystems*, 2016, 17 (11), pp.4605 - 4640. 10.1002/2016GC006385 . insu-01827721

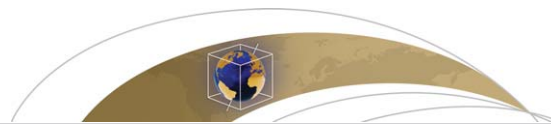
**HAL Id: insu-01827721**

**<https://insu.hal.science/insu-01827721>**

Submitted on 2 Jul 2018

**HAL** is a multi-disciplinary open access archive for the deposit and dissemination of scientific research documents, whether they are published or not. The documents may come from teaching and research institutions in France or abroad, or from public or private research centers.

L'archive ouverte pluridisciplinaire **HAL**, est destinée au dépôt et à la diffusion de documents scientifiques de niveau recherche, publiés ou non, émanant des établissements d'enseignement et de recherche français ou étrangers, des laboratoires publics ou privés.



## RESEARCH ARTICLE

10.1002/2016GC006385

## Effect of melt/mantle interactions on MORB chemistry at the easternmost Southwest Indian Ridge (61°–67°E)

M. Paquet<sup>1</sup>, M. Cannat<sup>1</sup>, D. Brunelli<sup>2,3</sup>, C. Hamelin<sup>4</sup>, and E. Humler<sup>5</sup>

## Key Points:

- At the easternmost SWIR, ultramafic seafloor basalts have lower CaO and Al<sub>2</sub>O<sub>3</sub> contents at a given MgO than most volcanic seafloor basalts
- Both types of basalts are derived from similar parental melts, but ultramafic seafloor basalts are more affected by melt-mantle reactions
- The principal effect of these reactions is to enrich the asthenospheric melts in MgO through olivine dissolution

## Supporting Information:

- Supporting Information S1
- Figure S1
- Figure S2
- Figure S3
- Figure S4
- Figure S5
- Figure S6
- Table S1
- Table S2
- Table S3
- Table S4
- Table S5
- Table S6
- Table S7
- Table S8

## Correspondence to:

M. Paquet,  
paquet@ipgp.fr

## Citation:

Paquet, M., M. Cannat, D. Brunelli, C. Hamelin, and E. Humler (2016), Effect of melt/mantle interactions on MORB chemistry at the easternmost Southwest Indian Ridge (61°–67°E), *Geochem. Geophys. Geosyst.*, 17, 4605–4640, doi:10.1002/2016GC006385.

Received 5 APR 2016

Accepted 27 SEP 2016

Accepted article online 3 OCT 2016

Published online 21 NOV 2016

<sup>1</sup>Equipe de Géosciences Marines, Institut de Physique du Globe de Paris, Sorbonne Paris Cité, Université Paris Diderot, UMR7154 CNRS, Paris, France, <sup>2</sup>Dipartimento di Scienze Chimiche e Geologiche, Università di Modena e Reggio Emilia, Modena, Italy, <sup>3</sup>Institute for Marine Sciences, CNR – ISMAR, Bologna, Italy, <sup>4</sup>Centre for Geobiology, University of Bergen, Bergen, Norway, <sup>5</sup>Laboratoire de Planétologie et Géodynamique, UMR 6112, CNRS, Université de Nantes, Nantes, France

**Abstract** The easternmost part of the Southwest Indian Ridge (61°–67°E) is an end-member of the global ridge system in terms of very low magma supply. As such, it is a good laboratory to investigate the effect of melt/mantle interactions on the composition of erupted basalts: for a given volume of erupted basaltic melt, the volume of reacted mantle is potentially greater than at more magmatically robust ridges. We analyzed major, trace element and isotopic compositions in three groups of rocks: plagioclase-bearing ultramafic and gabbroic rocks dredged in nearly amagmatic spreading corridors; basalts from the sparse volcanic cover of these corridors (“ultramafic seafloor basalts”); and basalts dredged from the intervening, more volcanically active domains (“volcanic seafloor basalts”). Ultramafic seafloor basalts have significantly lower CaO and Al<sub>2</sub>O<sub>3</sub> contents at a given MgO than most volcanic seafloor basalts. We propose that both types of basalts are derived from similar parental melts, but that the ultramafic seafloor basalts are more affected by reactions between these parent melts and the mantle rocks in the lithosphere below the ridge. We infer that these reactions occur in the walls of conduits that allow the aggregated melts extracted from the melting mantle to rise through the axial lithosphere and to the eruption sites. The principal effect of these reactions is to enrich the asthenospheric melts in MgO through olivine dissolution. This effect is not expected to be as noticeable, but could still play a role in basalt petrogenesis at more magmatic regions of the global slow-spreading MOR system.

## 1. Introduction

During its ascent beneath mid-ocean ridges, hot mantle material undergoes decompression and partial melting [Bottinga and Allègre, 1973; Carmichael *et al.*, 1974]. Mid Ocean Ridge basalts (MORB) result from the eruption of these melts at the seafloor. Their chemical composition depends on the composition of the mantle source [Jaques and Green, 1980; Kinzler and Grove, 1992a, 1992b, 1993] and on the degree and depth of partial melting [e.g., Dick *et al.*, 1984; Klein and Langmuir, 1987; Langmuir *et al.*, 1992]. However, several other processes also determine MORB composition: mixing and aggregation of melts during their ascent to the eruption site [e.g., Grove *et al.*, 1992], melt/rock interactions in the melting mantle and in the axial lithospheric mantle and crust [e.g., Kelemen *et al.*, 1990b; Rubin and Sinton, 2007; Lissenberg and Dick, 2008], and fractional crystallization [e.g., Klein and Langmuir, 1987; Langmuir *et al.*, 1992; Grove *et al.*, 1992]. Unraveling the chemical effects of these processes is key to better constrain the composition of the Earth’s mantle. It is also a way to approach the dynamics of mid-ocean ridge magmatic systems. This paper focuses on melt/rock reactions in the axial mantle lithosphere, and is based on a petrological and geochemical study of a suite of ultramafic, gabbroic and MORB samples collected on- and off-axis the Southwest Indian Ridge (SWIR) between longitude 61°E and 67°E (Figure 1).

Melt/rock interactions inferred to have occurred in the mantle part of the lithosphere at mid-ocean ridges have been documented from the study of troctolite-olivine gabbro suites sampled in ophiolites [Kelemen *et al.*, 1995, 1997; Borghini *et al.*, 2007; Borghini and Ramponi, 2007; Renna and Tribuzio, 2011; Sanfilippo and Tribuzio, 2013; Sanfilippo *et al.*, 2014] and at present-day ridges [Cannat *et al.*, 1990; Suhr *et al.*, 2008; Drouin *et al.*, 2009; Sanfilippo *et al.*, 2013]. The interpretation that prevails, particularly in the most recent studies, is that these troctolite-olivine gabbro suites result from assimilation and fractional crystallization processes involving MORB-like melts and a dunitic residual host rock [e.g., Cannat *et al.*, 1990; Kelemen *et al.*, 1995, 1997;

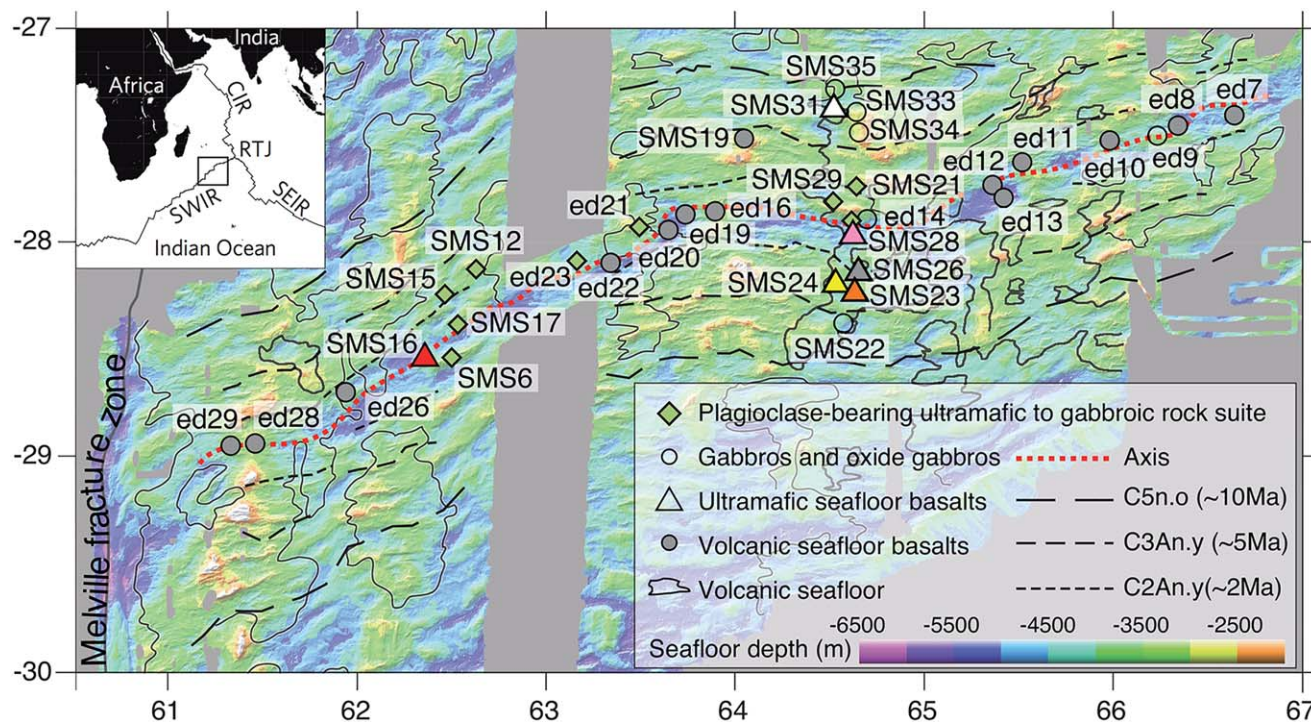


**Figure 1.** Location of the dredged samples considered in this study on a bathymetric map of the 61°–67°E region of the Southwest Indian Ridge (east of the Melville FZ). SMS6 to SMS35 are dredges from the Smoothseafloor cruise [Sauter et al., 2013]; ed7 to ed29 are dredges from the EDUL cruise [Mével et al., 1997]. The outlines of the volcanic seafloor domains are from Cannat et al. [2006].

Suhr et al., 2008; Drouin et al., 2009; Renna and Tribuzio, 2011; Sanfilippo and Tribuzio, 2013; Sanfilippo et al., 2013, 2014]. These dunites are proposed by many authors to have formed at an earlier stage, due to the reaction between Si-depleted melts and mantle harzburgite or lherzolite [e.g., Dick, 1977; Hopson et al., 1981; Quick, 1982; Kelemen et al., 1990; Suhr, 1999]. Trace element modeling consistently supports a MORB-like chemistry for the melt involved in forming the studied troctolites and olivine gabbros [Suhr et al., 2008; Drouin et al., 2009; Renna and Tribuzio, 2011; Sanfilippo et al., 2013, 2014]. However, the possible effects of such melt/rock interactions on the composition of erupted basalts have not yet been investigated. In fact, several authors suggest that the reacted melts have remained trapped in the axial lithosphere [Godard et al., 2009; Drouin et al., 2009; Renna and Tribuzio, 2011; Sanfilippo et al., 2014], and have therefore no effect on the composition of erupted basalts.

Interactions have also been proposed to occur between MORB-type melts and harzburgitic or lherzolitic mantle peridotites in the axial lithosphere [Cannat and Casey, 1995; Cannat et al., 1995, 1997b; Seyler et al., 2007]. Experimental studies by Tursack and Liang [2012], and Saper and Liang [2014] show that MORB-type melts reacting with residual lherzolites, over the range of temperatures and pressures expected for the base of the mantle lithosphere at slow-spreading ridges, are indeed capable of producing the clinopyroxene-rich mineral assemblages and the textures observed in natural melt-impregnated and reacted mantle rock suites, be they plagioclase-bearing as in the case of the troctolite-olivine gabbro suites, or plagioclase-free. In particular, their experiments produce clinopyroxene oikocrysts that enclose olivine, very similar to what is observed in natural samples (see microphotographs in Suhr et al. [2008]; Drouin et al. [2009]; or Sanfilippo et al. [2013]).

Seyler et al. [2007] proposed that clinopyroxene-rich harzburgites drilled at 15°N at the Mid-Atlantic Ridge (MAR) formed due to a reaction with MORB-like melts, leading to the dissolution of residual orthopyroxene (opx) and its replacement by clinopyroxene (cpx), olivine (ol) and spinel (sp). These authors also proposed that a two-stage partial melting-melt/rock reaction history, involving depletion and refertilization after an earlier high pressure melting followed by remelting and reequilibration of the melt with residual harzburgites, could explain why residual peridotites in the 15°N region of the MAR have more refractory

compositions than predicted from the composition of erupted MORBs sampled in the same region. They did not, however, investigate the effects these reactions could have on erupted MORB composition.

In this paper, we discuss the potential for melt/mantle interactions in the axial lithosphere to produce the suite of gabbroic and plagioclase-bearing ultramafic rocks sampled in the 61°–67°E SWIR region (Figure 1) and to modify the composition of erupted basalts. The two types of seafloor (volcanic and nearly amagmatic) exposed in this region have been dredged during the EDUL [Meyzen *et al.*, 2003; Seyler *et al.*, 2003], and Smoothseafloor [Sauter *et al.*, 2013] cruises. This study is based on samples from both cruises (Figure 1): plagioclase-bearing ultramafic and gabbroic rocks dredged from nearly amagmatic corridors, basalts dredged from the sparse volcanic cover of these corridors (“ultramafic seafloor basalts”), and basalts dredged from the intervening, more volcanically active domains (“volcanic seafloor basalts”). This sample set allows us to address the following questions: are basalts from nearly amagmatic corridors different from those erupted at the volcanic centers? If so, could the difference be explained by enhanced interactions of the parent melts with residual ultramafic rocks, to produce the plagioclase-bearing ultramafic to gabbroic rock suite? What could then be the range of melt to rock ratio in the melt/mantle reaction zones beneath nearly amagmatic spreading corridors? And what would this tell us about the axial magma plumbing system? Being aware that the eastern SWIR nearly amagmatic corridors represent an extremely low melt budget end-member for mid-ocean ridges, we then introduce a discussion of the extent to which these observations in the SWIR 61°–67°E region may be significant for other, more magmatically active ridges.

## 2. Geological and Basalt Geochemistry Background of the Study Area

The easternmost region of the ultraslow SWIR ( $\sim 14 \text{ mm.yr}^{-1}$ ) [Patriat and Segoufin, 1988] is an end-member of the global ridge system in terms of its very low magma supply. As such, it is a good laboratory to investigate the effect of melt/mantle interactions on the composition of erupted basalts: for a given volume of erupted basaltic melt, the volume of reacted mantle is potentially greater than at more magmatically robust ridges.

The low overall melt budget of the SWIR in the 61°–67°E (east of the Melville Fracture Zone) region is supported by the seismic crustal structure [Muller *et al.*, 1999], and by gravity data [Cannat *et al.*, 1999, 2006]. Underway geophysics, seafloor imagery and dredging [Cannat *et al.*, 2006; Sauter *et al.*, 2013] in the 61°–67°E region show that the modes of seafloor spreading are variable along-axis. There are large volcanic centers, where most of the low overall melt influx to the ridge is actually focused [Cannat *et al.*, 2003; Standish *et al.*, 2008], leaving corridors of essentially amagmatic spreading. In these corridors, the seafloor exposes wide expanses of partially serpentinized mantle-derived peridotites, with a small proportion of gabbroic rocks (<4% in volume of the dredged material [Sauter *et al.*, 2013]) and a thin and discontinuous basaltic cover (Figure 2). Off-axis dredging shows that mantle-derived material has been continuously exhumed in these corridors over the past 8 to 10 Myrs. The proposed tectonic interpretation is that mantle exhumation is accommodated by successive large offset normal faults that persist for 1 to 3 Myrs and dip alternatively to the north beneath the African-Somalian plate, or to the south beneath the Antarctic plate [Sauter *et al.*, 2013].

Microseismicity data recorded at the SWIR axis near 66°E [Schlindwein and Schmid, 2016], indicate that the seismogenic (i.e., brittle) part of the axial lithosphere there is substantially thicker than at the faster-spreading Mid-Atlantic Ridge (15 to 20 km-thick against about 8 km-thick at the MAR [Toomey *et al.*, 1988; Wolfe *et al.*, 1995; de Martin *et al.*, 2007]). In this thick lithosphere context, focusing of the melts toward volcanic areas can be enhanced [Cannat *et al.*, 2003; Standish *et al.*, 2008], favoring the formation of large axial volcanoes and further depleting the intervening nearly amagmatic ridge domains.

Basalt major element compositions in the 61°–67°E region of the SWIR [Meyzen *et al.*, 2003; Cannat *et al.*, 2008] also support a very low degree of melting of the source mantle. Basalt samples included in these earlier studies come from volcanic seafloor domains. They plot at the lowest  $\text{CaO}/\text{Al}_2\text{O}_3$  end of the global MORB trend (which can be interpreted in terms of the degree of partial melting [Klein and Langmuir, 1987]). They also have low FeO contents at a given MgO, and are enriched in most incompatible elements, including  $\text{Na}_2\text{O}$ . However, these basalts differ from the global MORB trend in that they contain significantly less  $\text{TiO}_2$  at a given MgO content, and have peculiar Rare Earth Elements (REE) compositions, depleted in heavy REE. [Meyzen *et al.*, 2003]. Meyzen *et al.* [2003] recognized that these characteristics could not be simply

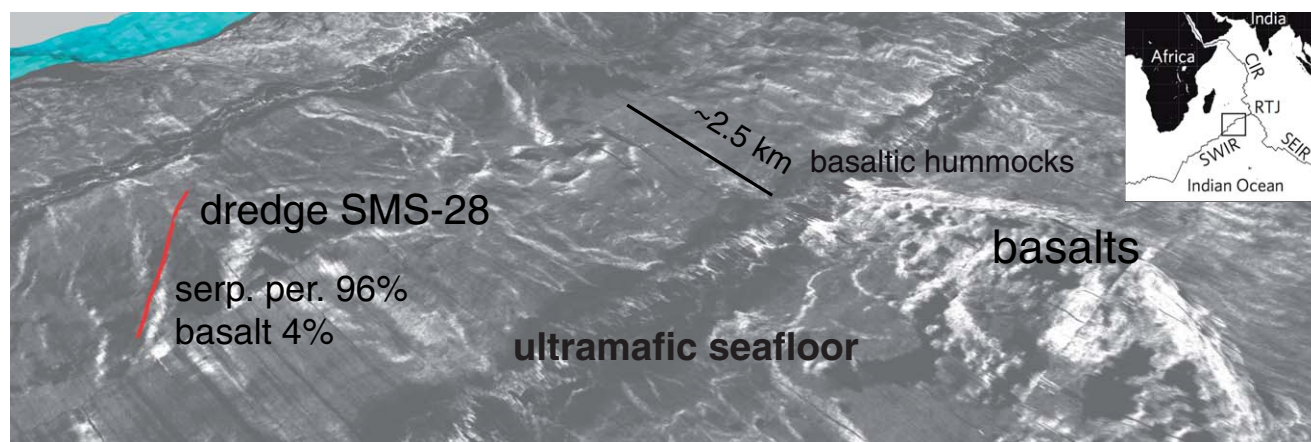


**Figure 2.** Perspective view of the reflectivity of the axial valley seafloor at 64°E on the Southwest Indian Ridge (side-scan sonar imagery acquired with the Towed Ocean Bottom Instrument, TOBI [Sauter *et al.*, 2013]). The track line for dredge SMS28 is shown in red. The smooth grey areas correspond to outcrops of tectonically exhumed serpentinized peridotites, and the more reflective hummocky areas are basalts directly erupted on these serpentinized peridotites (“ultramafic seafloor basalts”).

explained by low-degree melting of a typical mid-ocean ridge source mantle and proposed that the local mantle source had been depleted by an old melting event, and then refertilized prior to remelting below the SWIR. It is worth noting that these eastern SWIR basalts are similar in major element composition to the so-called low K/Ti basalts sampled in the most oblique section of the SWIR between 9 and 16°E [Standish *et al.*, 2008]. The composition of residual peridotites sampled in the 61°–67°E region also points to complexities in the melting and metasomatic history of the subaxial mantle [Seyler *et al.*, 2003, 2011], suggesting that low degrees of decompression melting in this region were accompanied by pervasive percolation of enriched liquids produced in the garnet field [Brunelli *et al.*, 2014].

### 3. Analytical Methods

In situ major element concentrations in basaltic fresh glasses and in olivine, plagioclase, clinopyroxene, orthopyroxene and spinel from the gabbroic and plagioclase-bearing ultramafic rocks were measured using the Cameca SX-100 electron microprobe (CAMPARIS service, Paris).

In situ trace element compositions in basaltic samples were determined at Montpellier 2 University on a ThermoFinnigan Element 2 High Resolution-Inductively Coupled Plasma-Mass Spectrometer (HR-ICP-MS) using a single collector double-focusing sector field Element XR (eXtended Range) coupled with laser ablation (LA) system, a Geolas (Microlas) automated platform housing a 193 nm Compex 102 laser from LambdaPhysik.

In situ trace element compositions of clinopyroxene, orthopyroxene and plagioclase in the impregnated and reacted ultramafic rocks were measured at the CIGS (Centro Interdipartimentale Grandi Strumenti) in Modena University on a Thermo Fisher Scientific Quadrupole- Inductively Coupled Plasma-Mass Spectrometer (Q-ICP-MS) XSeries 2 coupled with laser ablation (LA) system UP213.

Nd and Pb isotopic compositions in basalts were measured at Institut de Physique du Globe de Paris using a Thermo-Scientific Neptune.

Details on the analytical methods can be found in the supporting information Text S1.

### 4. Composition of Basalts From Volcanic and Nearly Amagmatic Seafloor

We consider the whole set of 95 available basaltic glass samples from 20 dredges at locations shown in Figure 1. Most samples are aphyric, with variable amounts of vesicles. Only 14 samples come from six dredges in nearly amagmatic corridors. The other 81 samples come from 14 dredges in volcanic domains. Of these volcanic seafloor basalt samples, 21 have been analyzed as part of the earlier work of Meyzen *et al.* [2003, 2005]. We have acquired major and trace element data for the other EDUL cruise samples, as well as for the

16 volcanic seafloor and nearly amagmatic seafloor basalts (“ultramafic seafloor basalts”) collected during the Smoothseafloor cruise. We also acquired isotopic data for 27 samples (13 from the EDUL cruise, and 14 from the Smoothseafloor cruise). This new isotopic data complements the data published by *Meyzen et al.* [2005]. Upon publication of this paper, this compiled data set will be contributed to the Petrological Database ([www.earthchem.org/petdb](http://www.earthchem.org/petdb) [Lehnert et al., 2000]). A selection of the most representative basalt compositions is presented in Table 1 (see supporting information Table S1 for complete data set).

In order to discuss the composition of the eastern SWIR basalts relative to global MORB trends, we have also compiled published major and trace element data for basalt glasses from other regions of the SWIR [Meyzen et al., 2003; Standish et al., 2008], from the ultraslow Gakkal Ridge [Gale et al., 2014], from Cayman Trough, from the Mid-Atlantic Ridge and from the East Pacific Rise (Petrological Database; [Lehnert et al., 2000]). Further details on the selection of these samples and complete references may be found in the supporting information Text S2.

#### 4.1. Major Elements

Compared to the global MORB trend, volcanic and ultramafic seafloor basalts from the 61°–67°E region plot in the highest Na<sub>2</sub>O and Al<sub>2</sub>O<sub>3</sub>, and lowest CaO and FeO ranges (Figure 3). Basalts from most dredges also have maximum MgO contents (up to 8.64%) that are significantly lower than basalts from the compilation for the MAR and EPR and for other regions of the SWIR (with the exception of the so-called low K/Ti basalts from the 9°E and 16°E SWIR region [Standish et al., 2008]). However, basalts dredged at three locations in volcanic seafloor domains (ED20, ED22, and ED26; Figure 1) have higher maximum MgO contents (up to 9.52 wt%; Figure 3). Several samples from these three dredges also have lower CaO and higher FeO at a given MgO content than the other 61°–67°E SWIR basalts.

Most 61°–67°E SWIR basalts are richer in Na<sub>2</sub>O and Al<sub>2</sub>O<sub>3</sub> at a given MgO content than basalts from other ridges, including other ultraslow and deep ridges such as Cayman Trough or Gakkal (Figures 3a and 3c), suggesting that they represent a global end-member in terms of low degrees of mantle partial melting. Their CaO/Al<sub>2</sub>O<sub>3</sub> ratio is also in the lowermost range (<0.67) for the global MOR system (Figures 4b and 4c). However, they are not, as could be expected for melts produced by low degree of mantle melting, also richer in TiO<sub>2</sub> at a given MgO content (Figure 3f). This led *Meyzen et al.* [2003] to propose that the 61°–67°E SWIR basalts derive from a titanium-depleted mantle source.

Ultramafic seafloor basalts have high Na<sub>2</sub>O contents (3.76–4.16 wt%) and low CaO contents (9.35–10.2 wt%) over a range of MgO contents (6.48 and 8.64 wt%). Compared to the volcanic seafloor basalts, they tend to have higher Na<sub>2</sub>O and TiO<sub>2</sub> contents at a given MgO content (Figures 3a and 3f), which would be consistent with a lower degree of mantle melting. Yet most also have lower Al<sub>2</sub>O<sub>3</sub> and higher FeO contents at a given MgO content (Figures 3c and 3d), which is not consistent with the lower degree of melting interpretation. Their CaO content is also significantly lower at a given MgO than most volcanic seafloor basalts (Figure 3b).

Basalt major element compositions are homogeneous in most nearly amagmatic seafloor dredges. Dredge SMS16, however, shows significant variability, with one sample (SMS16-3-14) that has a lower MgO content than the other 4 analyzed samples, and CaO, Al<sub>2</sub>O<sub>3</sub>, FeO and TiO<sub>2</sub> contents in the range of most volcanic seafloor basalts (Figure 3).

#### 4.2. Trace Elements

Most basalts from the 61°–67°E SWIR region, including the ultramafic seafloor basalts, have flat to slightly LREE-enriched REE patterns (Figure 4a). The (Ce/Sm)<sub>n</sub> ratio in these samples is  $\geq 1$  and they plot in the high (Ce/Sm)<sub>n</sub> and low CaO/Al<sub>2</sub>O<sub>3</sub> range, compared to other MORBs (Figure 4b). However, their (Sm/Yb)<sub>n</sub> ratio is generally lower, at a given CaO/Al<sub>2</sub>O<sub>3</sub> ratio, than that of basalts from other ultraslow and deep ridge regions (Gakkal or Cayman Trough; Figure 4c). This indicates a slight relative enrichment in the heaviest REE, which has been interpreted by *Meyzen et al.* [2003] as due to melting of a refertilized depleted mantle.

A small number of basalt samples from the volcanic domains have LREE-depleted patterns (Figure 4a and Table 2). These depleted samples come from dredges ED20, ED22 and ED26 (Figure 1) and also have higher maximum MgO contents, as well as lower CaO, Na<sub>2</sub>O, TiO<sub>2</sub> and SiO<sub>2</sub> and higher FeO at a given MgO content than the other 61°–67°E SWIR basalts (Figure 3). We have not recovered ultramafic seafloor basalts with such depleted REE patterns (Figure 4).

**Table 1.** Major Element Compositions (wt%) of Representative Ultramafic and Volcanic Seafloor Basalts From the 61°–67°E SWIR Region<sup>a</sup>

Sample Lat. (°) Long. (°) Depth (m) Age (My)	ED10-3-16		ED12-2-2		ED22-2-1		ED26-1-2		SMS19-4-4		SMS16-3-5		SMS16-3-14		SMS23-2-2		SMS24-2-3		SMS26-3-1		SMS28-3-3		SMS31-2-4	
	n=15	±	n=25	±	n=26	±	n=25	±	n=25	±	n=28	±	n=25	±	n=15	±	n=15	±	n=15	±	n=10	±	n=27	±
Seafoor	volcanic		volcanic		volcanic		volcanic		volcanic		ultramafic													
SiO <sub>2</sub>	50.78	0.78	50.29	0.49	49.00	0.27	48.73	-	51.14	0.26	50.42	0.41	50.73	0.30	50.53	0.01	50.43	0.01	50.67	0.06	50.54	0.09	51.37	0.20
TiO <sub>2</sub>	1.45	0.01	1.24	0.01	0.95	0.02	0.89	-	1.28	0.01	1.34	0.01	1.39	0.02	1.31	0.02	1.61	0.02	1.65	0.02	1.30	0.02	2.02	0.03
Al <sub>2</sub> O <sub>3</sub>	16.82	0.20	17.30	0.14	17.77	0.08	17.52	-	17.09	0.14	17.24	0.13	17.62	0.10	16.91	0.02	16.15	0.05	16.12	0.09	17.09	0.07	15.12	0.04
MnO	0.14	0.01	0.17	0.01	0.19	0.02	0.17	-	0.15	0.01	0.14	0.00	0.14	0.00	0.15	0.00	0.16	0.00	0.17	0.01	0.15	0.00	0.18	0.01
FeO	7.93	0.11	8.78	0.06	9.90	0.17	8.56	-	7.66	0.05	7.59	0.04	7.54	0.04	7.92	0.10	8.98	0.06	8.98	0.06	7.96	0.05	10.05	0.04
MgO	8.05	0.15	8.14	0.19	8.08	0.09	8.31	-	7.85	0.09	8.64	0.11	7.56	0.15	8.23	0.06	7.92	0.12	7.56	0.13	8.37	0.18	6.48	0.05
CaO	10.18	0.09	10.43	0.13	10.44	0.10	10.44	-	10.28	0.09	9.76	0.08	10.19	0.13	10.15	0.12	9.82	0.07	9.80	0.07	10.03	0.07	9.35	0.11
Na <sub>2</sub> O	3.95	0.10	3.88	0.12	3.25	0.07	3.15	-	3.79	0.09	4.16	0.09	4.17	0.09	3.81	0.10	4.05	0.08	4.04	0.07	3.90	0.10	4.08	0.10
K <sub>2</sub> O	0.27	0.01	0.21	0.01	0.11	0.01	0.04	-	0.14	0.01	0.18	0.01	0.18	0.01	0.19	0.02	0.26	0.01	0.25	0.02	0.21	0.02	0.21	0.01
P <sub>2</sub> O <sub>5</sub>	0.20	0.01	0.17	0.00	0.09	0.01	0.15	-	0.16	0.01	0.18	0.01	0.19	0.01	0.17	0.03	0.22	0.02	0.21	0.02	0.17	0.01	0.24	0.01
Cl	0.00	0.01	0.00	0.00	0.00	0.00	-	-	0.00	0.01	0.01	0.01	0.00	0.00	0.00	0.01	0.01	0.01	0.01	0.01	0.01	0.01	0.01	0.00
Total	99.79	1.24	99.98	0.96	100.04	0.55	99.15	-	99.55	0.51	99.68	0.63	99.73	0.57	99.38	0.01	99.63	0.24	99.47	0.24	99.74	0.23	99.14	0.29

<sup>a</sup>Error bars: ± 1 std.

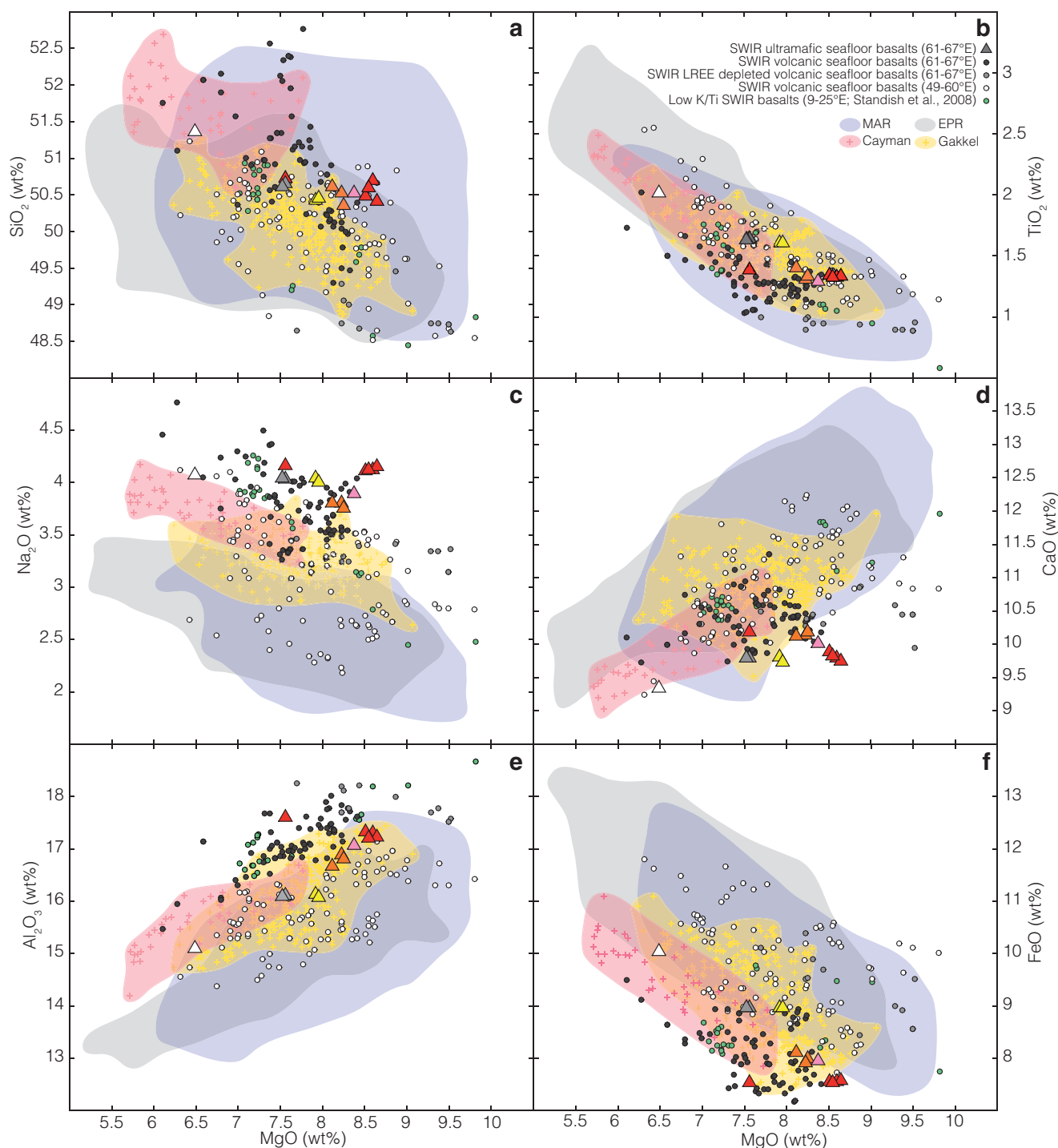


**Figure 3.** Major element compositions for basaltic samples from the easternmost part of the Southwest Indian Ridge (SWIR; 61° to 67°E), and from other regions of the SWIR and global mid-ocean ridge (MOR) system. (a) SiO<sub>2</sub>, (b) TiO<sub>2</sub>, (c) Na<sub>2</sub>O, (d) CaO, (e) Al<sub>2</sub>O<sub>3</sub> and (f) FeO contents as a function of MgO content. Triangles represent basalts collected in ultramafic seafloor areas of the 61°–67°E SWIR region (colored by dredge number as in Figure 1), and dark grey circles correspond to basalts collected in volcanic seafloor areas (pale grey symbols correspond to the LREE-depleted basalts sampled in dredges ED20, ED22 and ED26; Figure 1). The open circles are basalts collected in other regions of the Southwest Indian Ridge [Meyzen *et al.*, 2003; Humler *et al.*, unpublished data]. The green circles correspond to the low K/Ti basalts of Standish *et al.* [2008]. All the crosses correspond to PetDB ([www.earthchem.org/petdb](http://www.earthchem.org/petdb)), Lehnert *et al.*, 2000) data for the Mid-Atlantic Ridge (MAR), East Pacific Rise (EPR), Mid-Cayman Rise, and Gakkel ridge (PetDB) [Gale *et al.*, 2014]. Details on the selection of these other samples and complete references can be found in the supporting information.

A striking characteristic of the 61°–67°E SWIR basalts, which was also reported by Meyzen *et al.* [2003], is that the flat to slightly enriched REE patterns are nearly parallel. They do not, therefore, show evidence for a progression from less to more LREE-depleted samples, as would be expected for a suite of melts derived

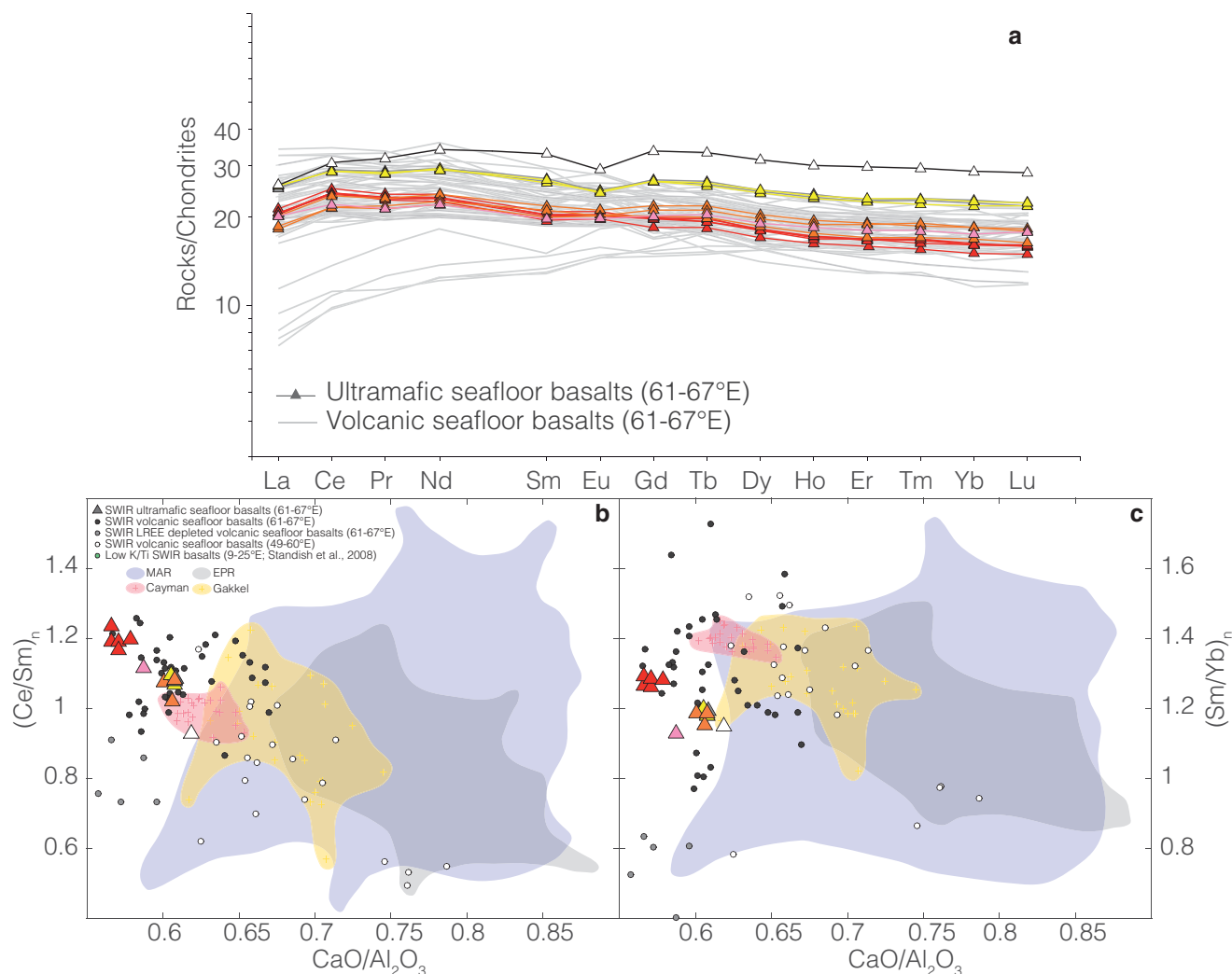


**Figure 4.** (a) Chondrite-normalized Rare Earth Element (REE) concentrations in basalts of the 61°–67°E region of the Southwest Indian Ridge. Ultramafic seafloor basalts are colored by dredge number as in the map of Figure 1. Volcanic seafloor basalts (Meyzen *et al.*, 2003; this study) are shown as thinner lines and a green field. (b)  $(Ce/Sm)_n$  and (c)  $(Sm/Yb)_n$  (normalized to chondrites) as a function of  $CaO/Al_2O_3$  (same symbols as in Figure 3). Normalizing values from McDonough and Sun [1995]. The open and green circles and the crosses are basalts from the SWIR and global mid-ocean ridge (MOR) system, as in Figure 3.

from different degrees of partial melting of a clinopyroxene-rich harzburgitic or lherzolitic mantle. Moreover, the most enriched patterns, with rock to chondrite ratios  $\geq 25$  for most REE (Figure 4a) also present distinctly negative Eu anomalies (Figure 4a), suggesting fractionation of plagioclase. Among ultramafic seafloor basalts, this is the case for samples from dredges SMS24, SMS26 and SMS31. By contrast, REE patterns for ultramafic seafloor basalts from dredges SMS16 (including the sample that plots at lower MgO than the other 4 analyzed samples; Figure 3), SMS23, and SMS28 have lower rock to chondrite ratios, and no Eu anomaly (Figure 4a).

The trace element abundances for the 61°–67°E SWIR basalts show the expected depletion for Rb, Ba, Th, U, Nb, Ta and Pb compared to LREE, as these trace elements are more incompatible than LREE. Ultramafic and volcanic seafloor basalts have similar contents in Sr (between 116 and 260 ppm), Sc (between 29 and 39 ppm) and Zr (between 49.9 and 152.7 ppm). Moreover, we note that the compositions measured in basalt samples from a given dredge are in most cases homogeneous.

#### 4.3. Isotopic Signature

Pb, and Nd isotopic data for ultramafic seafloor basalts (Table 3) are ranging from 17.69 to 17.79 for  $^{206}Pb/^{204}Pb$ , from 15.44 to 15.45 for  $^{207}Pb/^{204}Pb$ , from 37.5 to 37.59 for  $^{208}Pb/^{204}Pb$ , and from 0.513082 to

**Table 2.** Trace Element Compositions (ppm) of Representative Ultramafic and Volcanic Seafloor Basalts

Sample	ED12-2-2	ED22-2-1	ED26-1-2	SMS19-4-4	SMS16-3-5	SMS16-3-14	SMS23-2-2	SMS24-2-3	SMS26-3-1	SMS28-3-3	SMS31-2-4
Lat. (°)	-27.74	-28.11	-28.80	-27.51	-28.54	-28.54	-28.23	-28.19	-28.15	-27.96	-27.38
Long. (°)	65.35	63.36	61.93	64.06	62.36	62.36	64.63	64.54	64.65	64.63	64.55
Depth (m)	5550	4950	4600	2650	3850	3850	3870	3830	3960	4550	3200
Age (My)	<0.78	<0.78	<0.78	5.30	<0.78	<0.78	4.90	3.80	2.60	<0.78	8.80
Seafloor	volcanic	volcanic	volcanic	volcanic	ultramafic						
Sc	34	39	35	33	29	30	32	35	35	33	39
V	207	157	164	223	204	212	214	237	249	203	305
Cr	307	286	343	309	372	355	357	297	292	335	174
Co	44	50	51	38	42	41	40	40	39	40	47
Ni	156	145	221	129	213	175	162	151	127	159	166
Cu	66.2	96.5	93.8	61.7	64.3	64.5	67.2	65.9	64.2	64.2	56.9
Zn	67.5	62.6	56.2	59.4	61.4	62.0	62.7	72.8	72.1	58.4	81.9
Rb	2.5	0.8	0.4	1.2	1.0	1.1	1.6	3.1	2.6	1.6	2.0
Sr	160.3	116.3	117.6	180.1	220.3	229.6	171.6	173.9	177.8	198.5	145.7
Y	31.3	27.7	28.1	30.5	37.7	38.3	23.2	31.2	31.1	24.2	25.4
Zr	85.6	55.5	49.9	91.3	101.5	107.6	94.4	127.7	128.6	100.6	151.6
Nb	3.5	1.6	0.9	2.2	2.6	2.7	2.8	4.9	4.3	3.2	3.5
Ba	21.7	7.9	5.2	12.4	11.3	11.6	16.4	28.7	25.2	17.5	18.8
La	4.3	2.2	1.7	4.1	4.8	5.1	4.3	6.1	6.0	4.8	6.1
Ce	12.8	6.8	6.0	12.6	14.8	15.4	13.2	17.6	17.9	13.5	18.9
Pr	1.9	1.0	1.0	1.9	2.1	2.2	2.0	2.6	2.7	2.0	3.0
Nd	9.3	5.6	5.7	9.7	10.3	10.9	10.1	13.4	13.5	10.1	15.7
Sm	2.8	1.9	2.0	2.9	2.9	3.1	3.0	4.0	4.0	2.9	4.9
Eu	1.0	0.8	0.8	1.1	1.1	1.2	1.1	1.4	1.4	1.1	1.6
Gd	3.7	3.1	3.1	3.9	3.7	3.9	4.0	5.3	5.4	4.0	6.7
Tb	0.7	0.6	0.6	0.7	0.7	0.7	0.7	1.0	1.0	0.7	1.2
Dy	4.6	4.6	3.9	4.5	4.2	4.5	4.6	6.1	6.1	4.7	7.8
Ho	1.0	1.1	0.9	0.9	0.9	0.9	1.0	1.3	1.3	1.0	1.6
Er	2.9	3.2	2.6	2.7	2.5	2.7	2.7	3.7	3.7	2.9	4.8
Tm	0.5	0.5	0.4	0.4	0.4	0.4	0.4	0.6	0.6	0.4	0.7
Yb	3.0	3.5	2.7	2.6	2.4	2.6	2.7	3.7	3.7	2.8	4.6
Lu	0.5	0.5	0.4	0.4	0.4	0.4	0.4	0.5	0.5	0.4	0.7
Hf	2.0	1.4	1.3	2.2	2.2	2.3	2.1	3.0	3.0	2.2	3.8
Ta	0.2	0.1	0.1	0.2	0.2	0.2	0.2	0.3	0.3	0.2	0.2
Pb	0.7	0.4	0.3	0.7	0.8	0.8	0.7	0.9	0.9	0.7	0.9
Th	0.3	0.1	0.1	0.2	0.2	0.2	0.2	0.4	0.3	0.2	0.3
U	0.1	0.0	0.0	0.1	0.1	0.1	0.1	0.1	0.1	0.1	0.1

0.513098 for  $^{143}\text{Nd}/^{144}\text{Nd}$ , similar to the isotopic compositions reported by Meyzen *et al.* [2005] for volcanic seafloor basalts. The ultramafic seafloor basalts we have analyzed do, however, have  $^{206}\text{Pb}/^{204}\text{Pb}$  ratios lower than 17.8, whereas the measured  $^{206}\text{Pb}/^{204}\text{Pb}$  ratios for volcanic seafloor basalts mostly range between 17.8 and 18.1 (except for two samples ED29-1-1 and ED29-1-2, which have  $^{206}\text{Pb}/^{204}\text{Pb}$  ratios of 17.7). The isotopic variability of basalts, and of their mantle source in the easternmost part of the SWIR will be detailed in a forthcoming paper (Paquet, Hamelin *et al.*, in preparation).

### 5. Petrology and Composition of the Plagioclase-Bearing Ultramafic and Gabbroic Rock Suite

For this work we examined thin sections of 107 samples (supporting information Table S2) of plagioclase-bearing ultramafic and gabbroic rocks dredged in the nearly amagmatic corridors at locations shown in Figure 1. Based on cursory examination of the 107 samples in thin section, we selected 19 of the least altered samples (Table 4) for detailed petrological and chemical analyses. We excluded from this selection several samples of gabbros and oxide gabbros from dredges ED9, ED14, SMS22, SMS33, SMS34 and SMS35 (Figure 1). These gabbros have more evolved mineral compositions than the suite of rocks presented in this paper and are best interpreted as products of MORB fractional crystallization in the shallower axial lithospheric mantle of the nearly amagmatic corridors [Paquet *et al.*, 2014].

Modal proportions of the principal mineral phases in the plagioclase-bearing ultramafic and gabbroic suite were determined using line drawings made from high-resolution photographs of whole thin sections. The primary assemblage for all the samples consists of clinopyroxene + plagioclase ± olivine ±

**Table 3.** Isotopic Compositions of Representative On-Axis Ultramafic and Volcanic Seafloor Basalts

Sample	Seafloor	Lat. (°)	Long. (°)	Depth (m)	Age (My)	<sup>143</sup> Nd/ <sup>144</sup> Nd	2σ	<sup>206</sup> Pb/ <sup>204</sup> Pb	2σ	<sup>207</sup> Pb/ <sup>204</sup> Pb	2σ	<sup>208</sup> Pb/ <sup>204</sup> Pb	2σ
ED8-1-2	Volcanic	-27.35	66.34	4550	<0.78	0.513039	0.000005	17.78	0.00050	15.45	0.00044	37.71	0.00110
ED10-3-16	Volcanic	-27.57	65.98	4320	<0.78	0.513044	0.000005	17.80	0.00054	15.45	0.00049	37.70	0.00120
ED12-2-2	Volcanic	-27.74	65.35	5550	<0.78	0.513049	0.000004	17.89	0.00047	15.46	0.00041	37.81	0.00107
ED22-2-1	Volcanic	-28.11	63.36	4950	<0.78	0.513110	0.000005	17.90	0.00062	15.46	0.00056	37.73	0.00142
ED26-1-2	Volcanic	-28.80	61.93	4600	<0.78	0.513053	0.000005	17.96	0.00662	15.47	0.00558	37.84	0.01418
SMS16-3-4	Ultramafic	-28.54	62.36	3850	<0.78	0.513098	0.000004	17.77	0.00093	15.44	0.00068	37.59	0.00197
SMS16-3-5	Ultramafic	-28.54	62.36	3850	<0.78	0.513093	0.000004	17.76	0.00105	15.44	0.00058	37.50	0.00171
SMS16-3-7	Ultramafic	-28.54	62.36	3850	<0.78	0.513082	0.000005	17.79	0.00099	15.45	0.00094	37.52	0.00246
SMS16-3-9	Ultramafic	-28.54	62.36	3850	<0.78	0.513087	0.000004	17.76	0.00087	15.44	0.00091	37.53	0.00220
SMS16-3-14	Ultramafic	-28.54	62.36	3850	<0.78	0.513098	0.000004	17.76	0.00070	15.44	0.00058	37.58	0.00135
SMS28-3-3	Ultramafic	-27.96	64.63	4550	<0.78	0.513078	0.000004	17.69	0.00042	15.44	0.00034	37.55	0.00097

orthopyroxene ± spinel. Samples from most dredges display a great variability in terms of modal composition, ranging from plagioclase lherzolites, plagioclase websterites, to troctolites, olivine gabbros, gabbros and gabbroonorites (Figures 5 and 6). This variability commonly occurs over scales of a few centimeters to a few decimeters, within a single sample (Figures 5b and 5c), suggesting that the most plagioclase-rich assemblages form veins or irregular impregnations in the ultramafic rocks.

In order to compare the mineral composition of these samples to other ultramafic and gabbroic rock suites from slow spreading ridges, we compiled published major and trace element data for residual plagioclase-free peridotites from the 61–67°E region of the SWIR [Seyler et al., 2003], for the troctolite to olivine gabbros suite drilled at ODP Site U1309D at 30°N at the MAR [Drouin et al., 2009], and for the gabbros drilled at ODP Site 735 at 57°E on the SWIR [Ozawa et al., 1991; Dick et al., 2002].

### 5.1. Petrographic Description

#### 5.1.1. Plagioclase

Plagioclase-bearing lherzolites (Figures 5e and 6a) and websterites (Figures 5d and 6b) have less than 10% of plagioclase, while troctolites (Figure 5b), olivine gabbros (Figures 5a, 5c, and 6c) and gabbros (Figure 6d) have more than 40% (Table 4). The plagioclase distribution is heterogeneous even at the scale of a thin section (Figures 5b and 5c). Plagioclase forms small interstitial grains (<500 μm) associated with mafic minerals, or larger grains (up to one cm) in plagioclase-rich lenses (Figures 5a and 6c). In some samples, these plagioclase-rich

**Table 4.** Mineral Abundances for Selected Representative Samples of Plagioclase-Bearing Ultramafic to Gabbroic Rocks

Samples	Lithologies	Mineral Abundances (vol%)				
		Olivine	Orthopyroxene	Clinopyroxene	Spinel	Plagioclase
SMS6-2-1	Olivine gabbro	27.74	0.06	13.59	0.00	57.76
SMS6-5-2	Plagioclase-bearing lherzolite	62.79	30.27	4.54	0.002	2.03
SMS6-5-7A	Plagioclase-bearing websterite	7.43	12.89	70.60	0.16	8.93
SMS6-5-7B	Gabbro	0.00	21.24	20.70	0.00	58.05
SMS6-5-7C	Gabbro	0.30	11.74	32.47	0.00	55.22
SMS7-4-2	Troctolite	P	-	P	P	P
SMS10-2-1	Gabbro	-	-	P	-	P
SMS12-3-1B	Olivine gabbro	P	P	P	-	P
SMS15-3-20	Olivine gabbro	43.98	0.45	8.45	1.49	40.93
SMS17-4-22	Plagioclase-bearing websterite	P	P	P	P	P
SMS17-4-53	Olivine gabbro	P	P	P	-	P
SMS17-5-6	Olivine gabbro	22.64	5.03	28.57	1.64	40.23
SMS21-3-1	Olivine gabbro	17.12	0.95	16.11	0.00	65.24
SMS29-3-5	Plagioclase-bearing websterite	P	P	P	-	P
SMS29-3-9	Plagioclase-bearing websterite	0.00	43.10	28.62	0.51	27.77
ED14-1-1	Plagioclase-bearing lherzolite	P	P	P	-	P
ED14-1-3	Plagioclase-bearing lherzolite	P	P	P	P	P
ED21-4-1	Plagioclase-bearing lherzolite	P	P	P	P	P
ED21-10-3	Troctolite	17.64	0.00	1.94	0.00	80.43
ED23-3-6	Plagioclase-bearing lherzolite	79.82	12.14	5.32	0.02	0.08
ED23-4-1	Plagioclase-bearing lherzolite	41.18	11.11	4.29	0.28	2.13

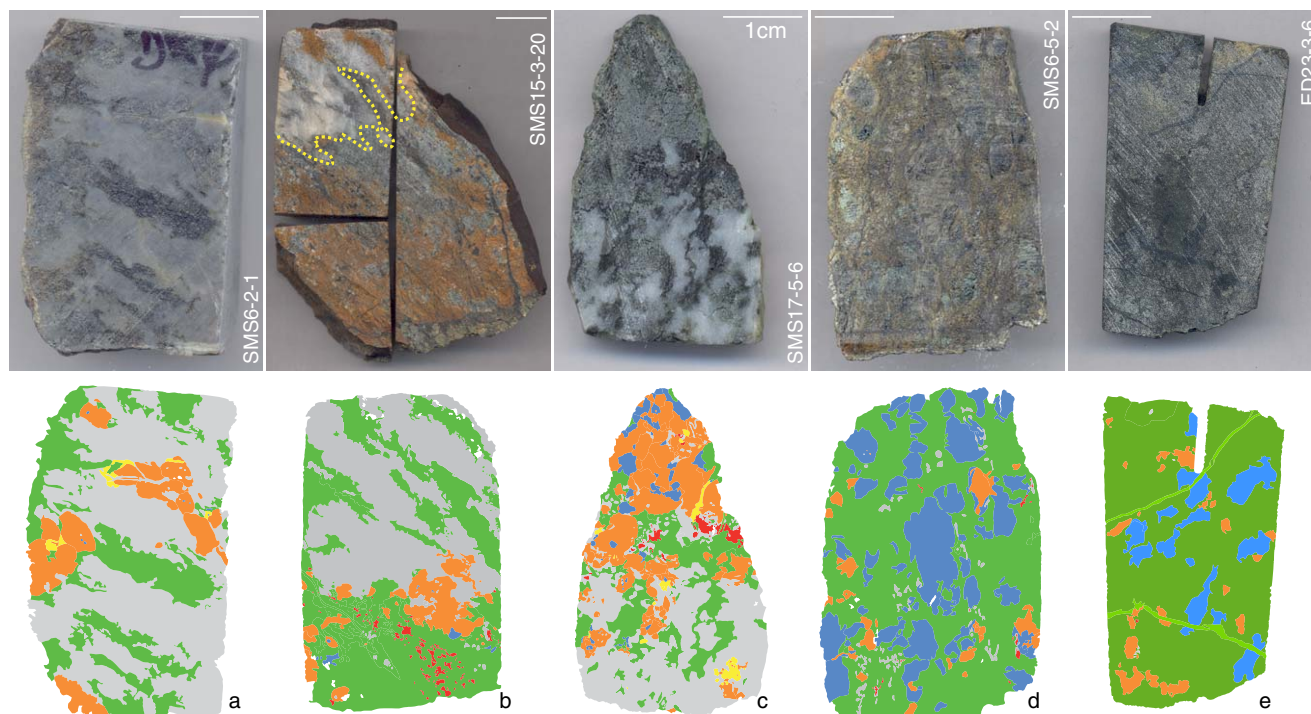


**Figure 5.** Representative photographs and line drawings of samples of the plagioclase-bearing ultramafic to gabbroic suite. Modal proportions of plagioclase increase from (e) right (plagioclase-bearing lherzolite) to (a) left (olivine gabbro) and within a few centimeters in Figures 5b and 5c. Line drawings made from high resolution photographs of whole thin sections are used to determine the modal proportions of the principal mineral phases in each sample (Table 4): plagioclase or altered plagioclase in grey, olivine or serpentine after olivine in green, orthopyroxene or serpentine after orthopyroxene in blue, clinopyroxene in orange and spinel in red. Altered phases with undetermined protolith in yellow; serpentine veins in pale green.

lenses have a preferred orientation (Figure 5a). Plagioclase grains are irregular in shape, with widespread evidence for intracrystalline deformation (mechanical twins and undulose extinction) and for dynamic recrystallization into smaller grains (Figures 6c and 6d). Interstitial plagioclase also forms rims around spinel in the most ultramafic samples (Figure 7a), or crystallizes as small irregular grains that appear to partially replace orthopyroxene (Figure 7b).

#### 5.1.2. Clinopyroxene

Clinopyroxene forms millimeter-sized anhedral to poikilitic crystals that commonly contain inclusions of orthopyroxene and plagioclase, and orthopyroxene exsolution lamellae (Figures 7a and 7b). Orthopyroxene inclusions within a given clinopyroxene commonly share the same crystallographic orientation. These textural relations suggest that clinopyroxene replaced former orthopyroxene porphyroclasts, following plagioclase crystallization. Some of the orthopyroxene relicts in clinopyroxene show kink bands (Figure 7d) or undulose extinction, while the host clinopyroxene appears undeformed. This indicates that clinopyroxene crystallized after an episode of deformation of the orthopyroxene porphyroclasts. However, in several samples, clinopyroxene grains are also kinked, bent (e.g., in Figures 6c and 6d) and locally recrystallized in association with plagioclase neoblasts.

#### 5.1.3. Orthopyroxene

Orthopyroxene porphyroclasts comprise up to 43.1% of the mode in the plagioclase-bearing websterites, and typically 10 to 30% of the mode in plagioclase-bearing lherzolites (Figures 5d and 5e; Table 4). They are kinked and commonly contain thin clinopyroxene exsolution lamellae (Figure 7d). In gabbroic samples, we also observed small (<300  $\mu\text{m}$ ) irregularly shaped to oval orthopyroxene in the plagioclase and clinopyroxene matrix, and as inclusions in the clinopyroxenes (Figure 7c). These small orthopyroxene grains tend to share a common crystallographic orientation (Figures 7a–7d) and probably represent isolated relicts from preexisting orthopyroxene porphyroclasts. Finally, rims of secondary orthopyroxene (up to 50  $\mu\text{m}$ -thick) are common between olivine and plagioclase (Figure 7e).

#### 5.1.4. Olivine

Olivine occurs as irregularly shaped grains, from a few tens of micrometers to one centimeter in size, with subgrain boundaries and undulose extinction (Figure 7f). Olivine grains tend to have curvilinear contacts

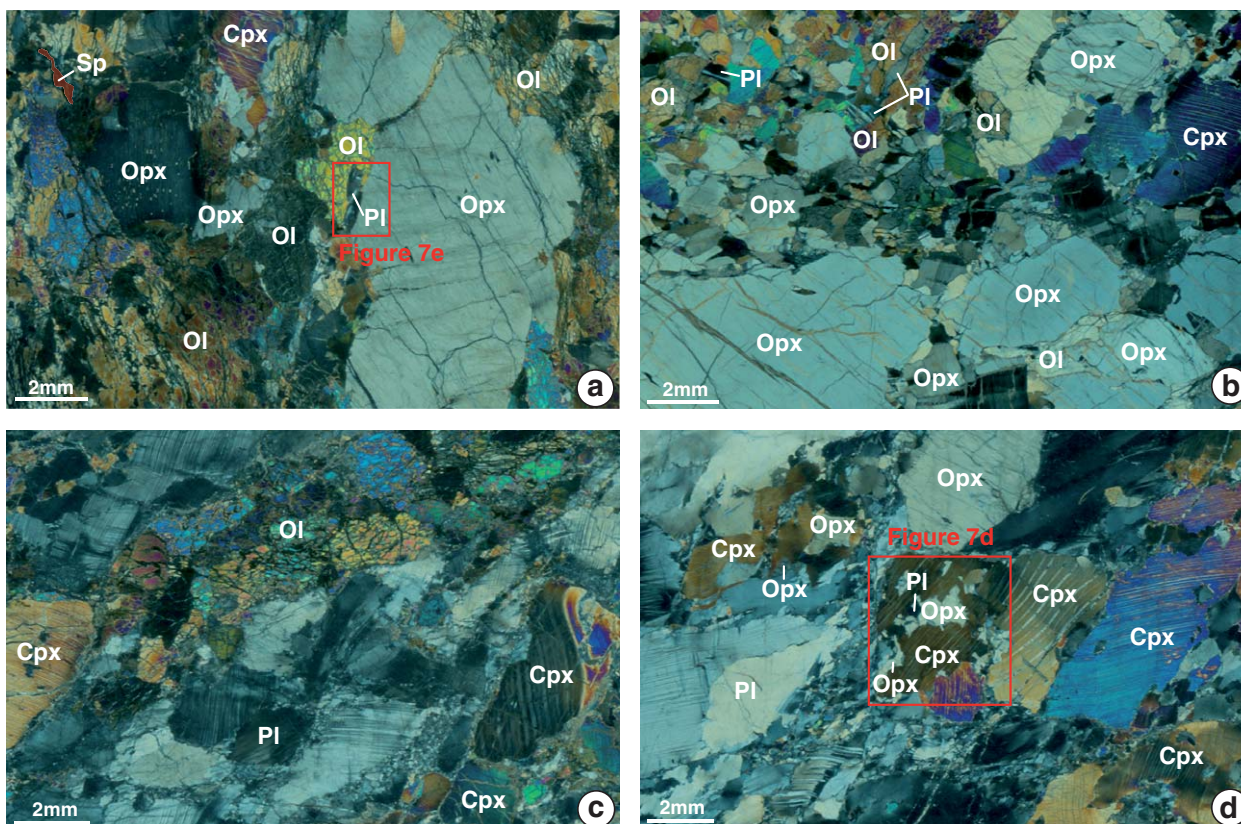


**Figure 6.** Representative microphotographs of samples of the plagioclase-bearing ultramafic to gabbroic suite. Crossed nicols. (a) Sample SMS6-5-2 (Figure 5d): plagioclase-bearing Iherzolite with small interstitial grains of plagioclase (Pl) and large orthopyroxenes (Opx) with fine clinopyroxene (Cpx) exsolutions; olivines (Ol) are irregularly shaped with subgrains boundaries and undulose extinction; contacts between olivine and orthopyroxene are lobate; spinels (Sp) appear with elongated shapes. (b) Sample SMS17-4-22: plagioclase-bearing websterite with large kinked orthopyroxenes which have lobate contacts with olivine; plagioclase appear as small droplets (<1mm) between olivines, clinopyroxenes and orthopyroxenes. (c) Sample SMS6-2-1 (Figure 5a): olivine gabbro with plagioclase-rich lenses, kinked clinopyroxenes and equant to elongated olivines. (d) Sample SMS6-5-7: gabbro with a large proportion of orthopyroxene which occurs as large grains, smaller grains in the plagioclase matrix or next to a clinopyroxene crystal enclosing orthopyroxene and plagioclase inclusions. In Figures 6c and 6d, plagioclase occurs as relatively large grains, with common mechanical twins, and small (few tens of  $\mu\text{m}$  to hundred of  $\mu\text{m}$ ) recrystallised neoblasts, and clinopyroxenes show orthopyroxene exsolutions and undulose extinction.

with orthopyroxenes (Figure 7f), a texture that is common in residual abyssal peridotites and has been interpreted as resulting from incongruent melting of the pyroxene [e.g., Seyler *et al.*, 2007]. In plagioclase-rich samples, olivine forms lens-shaped aggregates (Figure 6c), with grain shapes and subgrains that are similar to those observed in the more ultramafic samples.

### 5.1.5. Spinel

Spinel is present in several samples (Table 4), forming amoeboid to vermicular grains that range in size between a few tens of micrometers and a few millimeters. These spinels are brown and partially altered into magnetite. One sample (SMS6-2-1) contains very small spinels (<100  $\mu\text{m}$ ), enclosed in olivine grains. Most spinels are larger and surrounded by plagioclase. We did not observe the large poikilitic grains enclosing olivine described by Seyler *et al.* [2003] in plagioclase-free serpentinized Iherzolites from the same region.

## 5.2. Mineral Major Element Compositions

### 5.2.1. Plagioclase

Plagioclase anorthite (An) contents range between 80.60 and 91.60% in plagioclase Iherzolite or plagioclase websterite, and between 58.76 and 69.68% in troctolites, olivine gabbros, gabbros and gabbroonites (Figures 8a and 8b; Table 5). An content therefore appears to be inversely correlated with the modal proportion of plagioclase.

In order to further investigate this relation, we selected a sample in which plagioclase abundance varies significantly over scales of a few centimeters, and in which the range of measured An values is large (66.54 to

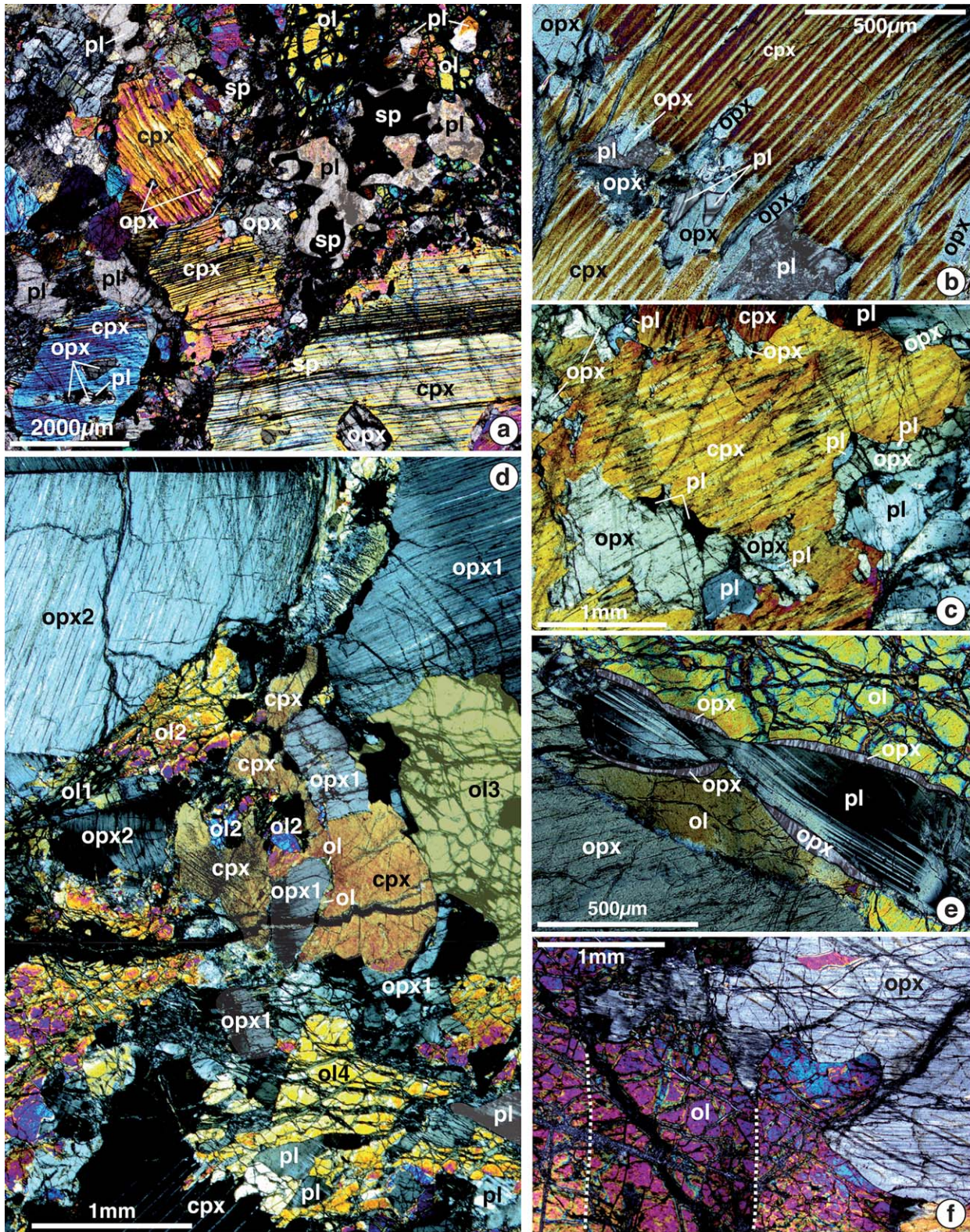


**Figure 7.** Representative microphotographs of samples of the plagioclase-bearing ultramafic to gabbroic suite. Crossed nicols. (a) Sample SMS17-5-6: olivine gabbro. Clinopyroxene with orthopyroxene exsolutions forms millimeter-sized anhedral to poeikilitic crystals that commonly contain inclusions of plagioclase and orthopyroxene (fragments that share a common crystallographic orientation). Spinel appear to be amoeboid to vermicular, and mostly surrounded by plagioclase aureoles. (b) Sample SMS6-2-1: olivine gabbro. (c) Sample SMS6-5-7: gabbro. In Figures 7b and 7c, clinopyroxenes with orthopyroxene exsolutions are enclosing orthopyroxene and plagioclase inclusions. Additionally, in Figure 7c, orthopyroxenes also occur as irregularly shaped to oval in the plagioclase matrix, or next to a clinopyroxene crystal with orthopyroxene and plagioclase inclusions; all the orthopyroxene fragments have the same crystallographic orientation. These textures indicate that clinopyroxene replaced orthopyroxene porphyroclasts, following plagioclase-forming melt/rock reactions. (d) Sample SMS6-5-2: plagioclase-bearing lherzolite. Orthopyroxenes form large grains with fine clinopyroxene exsolutions, and kinks. Plagioclase occurs as small interstitial grains. In the center of the picture, the clinopyroxene is enclosing relics of two different olivine grains and of orthopyroxene. The fragments of olivine and orthopyroxene share a common crystallographic orientation with Ol2 and Ol3 (small grains trapped between the clinopyroxene and the orthopyroxene fragment), and Opx1 respectively. Some of the orthopyroxene relicts in clinopyroxene show kink bands or undulose extinction, while the host clinopyroxene appears undeformed. This indicates that clinopyroxene crystallized after an episode of deformation of the orthopyroxene porphyroclasts. (e) Sample SMS6-5-2: plagioclase-bearing lherzolite. Contacts between olivine and plagioclase are commonly underlined by reactional orthopyroxene. These rims of secondary orthopyroxene are observed in most samples, independently of the modal proportion of plagioclase and indicate that the impregnating melt was Si-enriched relative to the host peridotite. (f) Sample ED23-3-6: plagioclase-bearing lherzolite. Relations between residual kinked (dashed lines) olivine with undulose extinction and orthopyroxene show lobate contacts possibly due to episodes of incongruent melting [e.g., Kelemen, 1990; Kinzler and Grove, 1992b; Seyler et al., 2007].

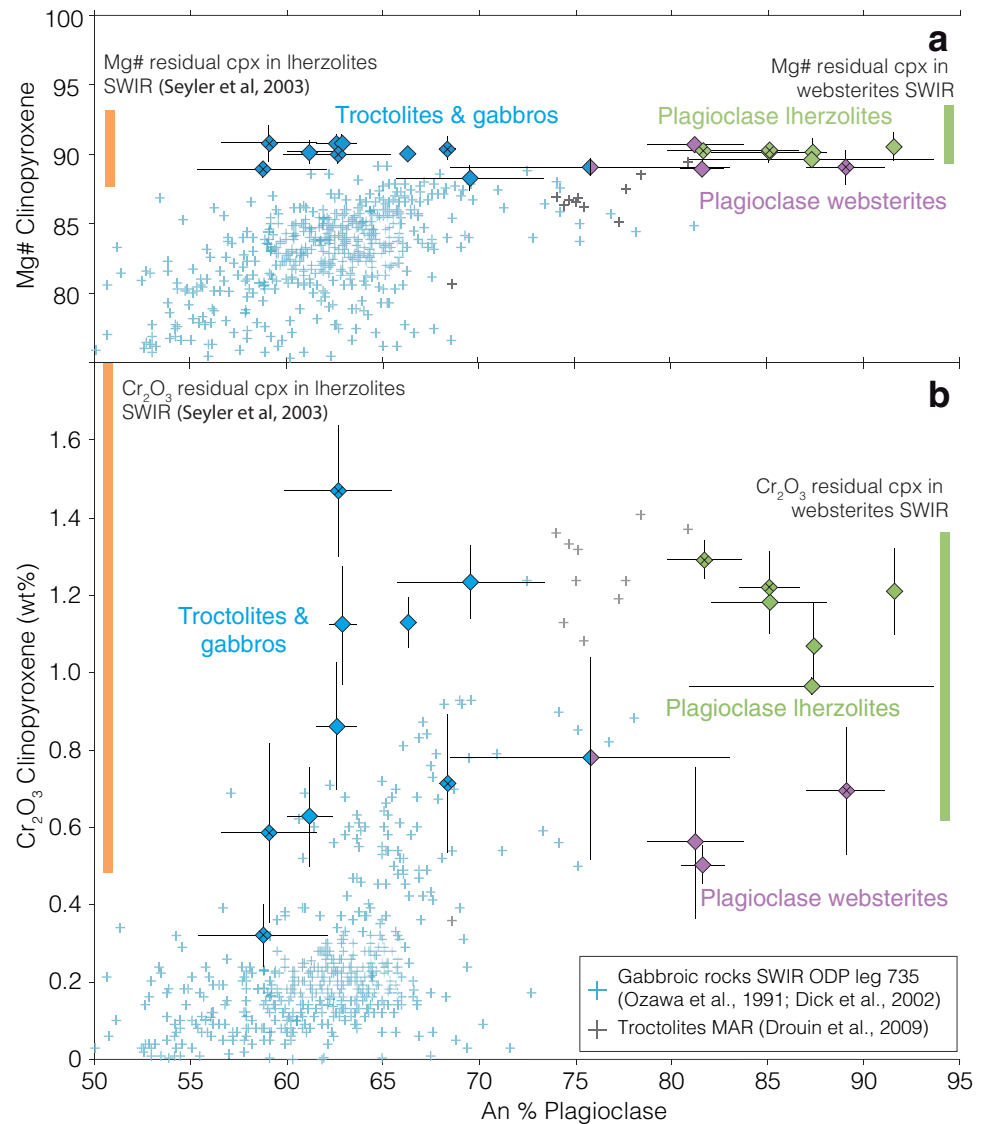


**Figure 8.** Clinopyroxene and plagioclase major element compositions in samples of the plagioclase-bearing ultramafic to gabbroic suite. (a) Clinopyroxene Mg# and (b) Clinopyroxene Cr<sub>2</sub>O<sub>3</sub> content as a function of plagioclase anorthite content. Diamond data point corresponds to the average composition of several grains in each sample (n values in Tables 5 and 6; supporting information Tables S3 and S4). Error bars: ±1 std. Diamonds are colored according to modal mineralogy: plagioclase-bearing Iherzolites in green, plagioclase-bearing websterites in purple, troctolites, olivine gabbros and gabbros in blue. The blue-purple diamond corresponds to hybrid sample SMS6-5-7 described in Figure 9b. Diamonds with a cross inside correspond to samples for which we also analyzed in-situ trace elements. Orange and green bars show ranges of composition reported for residual clinopyroxenes in plagioclase-free peridotite samples [Seyler *et al.*, 2003] and in plagioclase-free websterites (Brunelli *et al.*, unpublished data) respectively. The Mg# of clinopyroxenes in the plagioclase-bearing samples appears buffered by that of the reacted residual peridotite. The Cr<sub>2</sub>O<sub>3</sub> content of clinopyroxenes shows a greater variability, with lower values in the plagioclase-bearing websterites, and in some troctolites, olivine gabbros and gabbros. Points for ODP Site 735 correspond to a subset of the data with plagioclase An contents > 50%.

85.19%; Figure 9a). In this sample, we compared the composition of plagioclase grains measured in two parallel thin sections cut within 1.5 centimeters of one another, one with a plagioclase-websterite modal mineralogy (A), the other with a gabbro-norite mineralogy (B; Figure 9b). Plagioclase grains belong to three types: small grains isolated in the mafic mineral assemblage (thin section A), small grains enclosed into clinopyroxenes (thin sections A and B), and larger grains (≥ 500 μm to 1 mm; thin section B). The small plagioclase grains (inclusions in the clinopyroxenes or in the mafic groundmass) have similar anorthite contents, between 73.54 and 85.19% (mean An value of 80.77 ± 4.06%) (Figure 9c). The larger grains have lower anorthite content, between 66.54 and 74.12% (mean An value of 68.82 ± 2.36%) (Figure 9c).

**Table 5.** Major Element Compositions (wt%) of Plagioclases of Representative Plagioclase-Bearing Ultramafic and Gabbroic Rocks<sup>a</sup>

	SMS6-2-1 Core		SMS6-5-2 Core		SMS6-5-7 Core		SMS7-4-2 Core		SMS17-4-22 Core		SMS17-5-6 Core		SMS29-3-9 Core		ED21-10-3 Core		ED23-3-6 Core	
	(n=26)	±	(n=13)	±	(n=40)	±	(n=2)	±	(n=10)	±	(n=11)	±	(n=3)	±	(n=14)	±	(n=12)	±
SiO <sub>2</sub>	52.92	1.00	46.13	1.71	48.48	1.95	52.07	0.69	46.97	0.54	50.28	1.07	45.09	0.74	51.05	0.94	47.60	0.85
TiO <sub>2</sub>	0.05	0.03	0.04	0.02	0.03	0.02	0.04	0.00	0.03	0.02	0.04	0.03	0.03	0.02	0.03	0.02	0.02	0.02
Al <sub>2</sub> O <sub>3</sub>	30.34	0.64	34.83	1.17	32.81	1.18	30.68	0.10	33.46	0.51	31.72	0.66	35.23	0.30	31.36	0.40	33.87	0.25
FeO <sub>tot</sub>	0.10	0.10	0.07	0.05	0.08	0.04	0.16	0.02	0.10	0.03	0.16	0.06	0.25	0.03	0.14	0.05	0.20	0.08
MnO	0.01	0.02	0.01	0.01	0.01	0.02	0.01	0.01	0.01	0.01	0.01	0.01	0.01	0.01	0.01	0.02	0.01	0.02
MgO	0.01	0.05	0.00	0.00	0.00	0.00	0.01	0.00	0.00	0.00	0.00	0.01	0.00	0.00	0.03	0.03	0.03	0.04
CaO	12.34	0.70	17.94	1.24	15.70	1.42	13.27	0.22	16.65	0.46	14.38	0.78	18.22	0.43	14.04	0.40	16.81	0.35
Na <sub>2</sub> O	4.77	0.39	1.44	0.74	2.77	0.85	4.36	0.12	2.12	0.29	3.46	0.44	1.23	0.22	3.58	0.25	2.07	0.19
K <sub>2</sub> O	0.02	0.01	0.01	0.01	0.01	0.01	0.03	0.00	0.01	0.01	0.02	0.01	0.01	0.01	0.01	0.01	0.01	0.01
Cr <sub>2</sub> O <sub>3</sub>	0.01	0.01	0.01	0.01	0.01	0.01	0.01	0.01	0.00	0.00	0.02	0.01	0.00	0.00	0.01	0.01	0.01	0.01
NiO	0.01	0.02	0.02	0.02	0.01	0.02	0.00	0.00	0.02	0.01	0.01	0.02	0.01	0.01	0.01	0.02	0.04	0.07
Cl	0.00	0.00	0.01	0.01	0.01	0.01	0.00	0.00	0.00	0.00	0.01	0.01	0.00	0.00	0.00	0.00	0.00	0.00
F	0.06	0.08	0.01	0.09	0.05	0.11	0.00	0.00	0.09	0.10	0.01	0.01	0.11	0.07	0.01	0.02	0.03	0.05
Total	100.65	0.43	100.51	0.94	99.96	0.95	100.66	0.68	99.47	0.45	100.12	0.34	100.19	0.48	100.28	0.71	100.71	0.63
Ab %	41.11	3.33	12.66	6.36	24.15	7.26	37.19	1.07	18.66	2.50	30.30	3.79	10.88	1.96	31.56	1.95	18.23	1.57
An %	58.76	3.36	87.27	6.37	75.80	7.27	62.62	1.04	81.26	2.49	69.58	3.82	89.06	2.02	68.35	1.94	81.70	1.59
Or %	0.13	0.07	0.07	0.04	0.05	0.06	0.19	0.02	0.07	0.05	0.12	0.06	0.06	0.06	0.08	0.05	0.06	0.06

<sup>a</sup>Average composition of several plagioclase grains in each sample. Error bars: ±1 std.

Plagioclase in this sample, similar to other samples that plot in the 65–91.6 range of An contents, has low (<0.03 wt%) K<sub>2</sub>O contents (the dispersion is interpreted as due to analytical error at these low concentrations). By contrast, large plagioclase grains in several samples of troctolite, olivine gabbro and gabbro have yet lower plagioclase An contents (58.76 to 62.91%), and slightly higher K<sub>2</sub>O (and TiO<sub>2</sub>) contents (up to 0.05 wt% for K<sub>2</sub>O, and between 0.03 and 0.08 wt% for TiO<sub>2</sub>) (Figure 9a). This sample-scale study therefore indicates that the highest An values (73.54 to 85.19%) are measured in small plagioclase grains isolated in mafic mineral assemblages, and that these small An-rich grains can be preserved as inclusions in clinopyroxenes in gabbroic samples that also contain plagioclase-rich domains with lower An contents. Additionally, we identify a subgroup of troctolites, olivine gabbros and gabbros that contains plagioclase with yet lower An content (58.76 to 62.91%) and higher K<sub>2</sub>O contents (Figure 9a).

### 5.2.2. Clinopyroxene

The Mg# of clinopyroxene remains in a very narrow range (88.28 to 90.85%) over the wide range of measured plagioclase An contents (Figure 8a; Table 6 and supporting information Table S4). This range of Mg# is similar to that of clinopyroxene measured in plagioclase-free residual lherzolites in the same region (between 87.63 and 93.21% [Seyler *et al.*, 2003]). The Cr<sub>2</sub>O<sub>3</sub> content of clinopyroxenes in these samples shows a greater variability (Figure 8b): Cr<sub>2</sub>O<sub>3</sub> values between 0.97 and 1.29 wt% are measured in plagioclase-lherzolites, similar to values measured in clinopyroxenes from plagioclase-free residual lherzolites in the same region (between 0.48 and 1.80 wt% [Seyler *et al.*, 2003]). The Cr<sub>2</sub>O<sub>3</sub> content of clinopyroxenes in plagioclase-websterites is lower (0.50 to 0.69 wt%), within the range of Cr<sub>2</sub>O<sub>3</sub> contents measured in a selection of plagioclase-free websterites from the same region (between 0.62 and 1.36 wt%) (Brunelli *et al.*, unpublished data). The Cr<sub>2</sub>O<sub>3</sub> contents of clinopyroxenes in samples of troctolite, olivine gabbro and gabbro spans a 0.32 to 1.47 wt% range.

Clinopyroxene Al<sub>2</sub>O<sub>3</sub>, Na<sub>2</sub>O and TiO<sub>2</sub> contents (Table 6 and supporting information Table S4) in plagioclase-bearing samples vary respectively between 3.01 and 6.40 wt%, between 0.31 and 0.59 wt%, and between 0.33 and 0.78 wt%. There is no systematic difference in Al<sub>2</sub>O<sub>3</sub>, Na<sub>2</sub>O and TiO<sub>2</sub> contents between plagioclase-bearing lherzolites and plagioclase-bearing websterites. Nevertheless, clinopyroxenes of the plagioclase-bearing lherzolites and websterites tend to have higher Al<sub>2</sub>O<sub>3</sub> (from 4.88 to 6.40 wt% for Al<sub>2</sub>O<sub>3</sub>) contents, and slightly lower Na<sub>2</sub>O and TiO<sub>2</sub> (from 0.31 to 0.51 wt% for Na<sub>2</sub>O, and from 0.33 to 0.68 wt% for TiO<sub>2</sub>) contents than those of the troctolites, olivine gabbros and gabbros (from 3.01 to 5.89 wt% for Al<sub>2</sub>O<sub>3</sub>; from 0.36 to 0.59 wt% for Na<sub>2</sub>O; from 0.34 to 0.78 wt% for TiO<sub>2</sub>). Clinopyroxene Al<sub>2</sub>O<sub>3</sub>, Na<sub>2</sub>O and TiO<sub>2</sub> contents in the plagioclase-bearing ultramafic to gabbroic suite samples are within the range of values measured in residual clinopyroxenes from plagioclase-free peridotites of the region (between 3.38 and 8.81 wt% for Al<sub>2</sub>O<sub>3</sub>, between 0.09 and 1.47 wt% for Na<sub>2</sub>O, between 0.05 to 0.63 wt% for TiO<sub>2</sub> [Seyler *et al.*, 2003]). The values, reported in

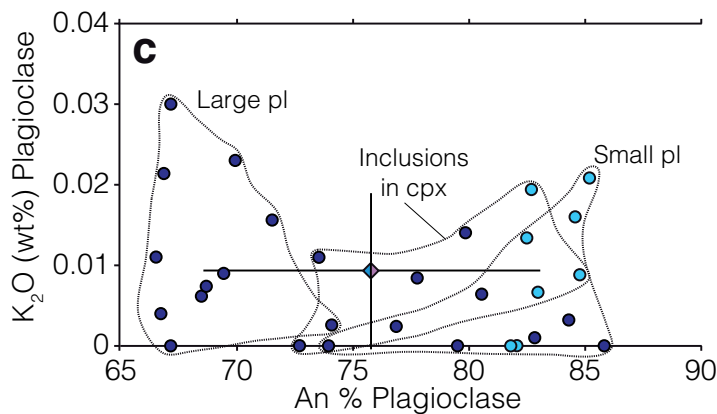
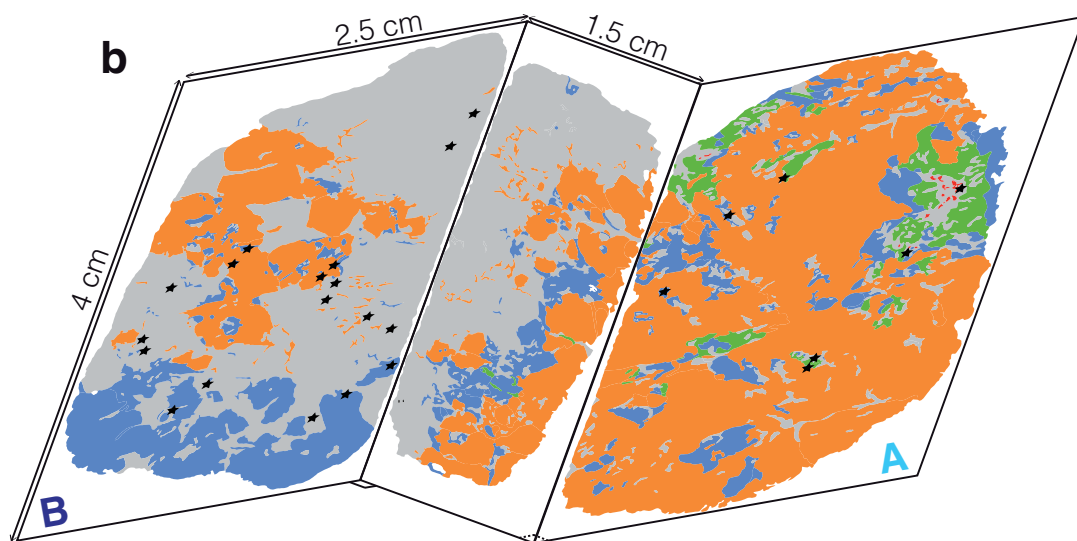
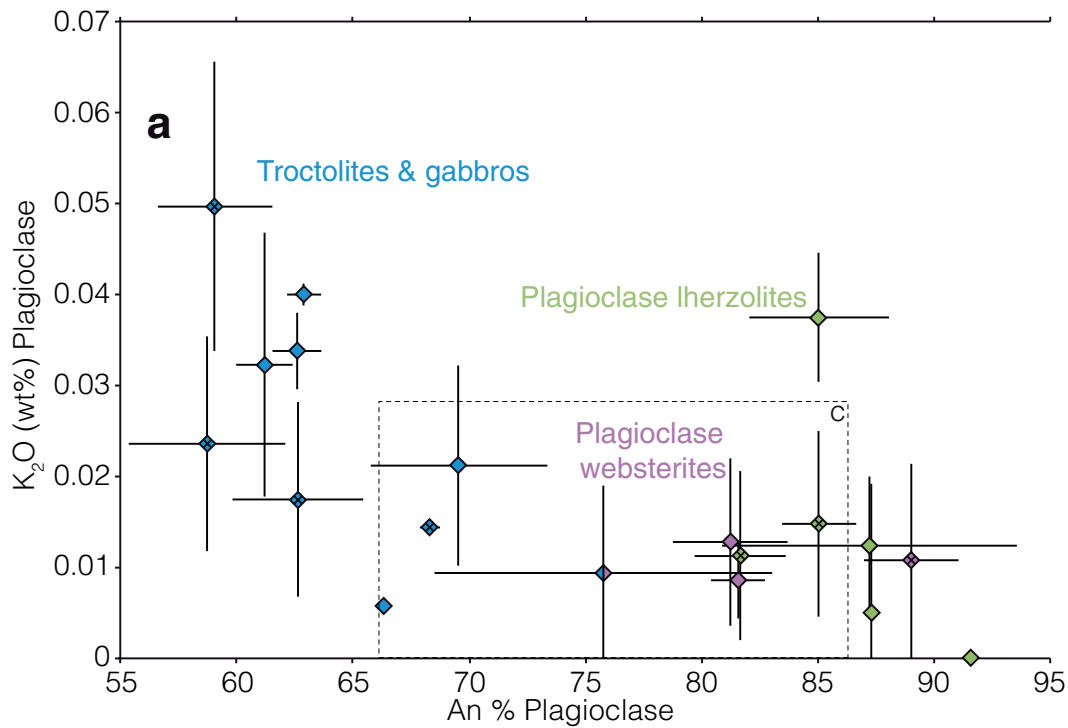


**Figure 9.** Plagioclase compositional variations in samples of the plagioclase-bearing ultramafic to gabbroic suite. (a) Plagioclase  $K_2O$  content as a function of anorthite content. Diamond data point corresponds to the average composition of several plagioclase grains in each sample ( $n$  values in Table 5). Error bars:  $\pm 1$  std. Samples for which we analyzed plagioclase and/or clinopyroxene trace element compositions are shown as diamonds with a cross inside. Same symbols as in Figure 8. (b) Line drawing showing mineral modal abundances (plagioclase or altered plagioclase in grey, olivine or serpentine after olivine in green, orthopyroxene or serpentine after orthopyroxene in blue, clinopyroxene in orange, spinel in red) in three orthogonal thin sections cut in sample SMS6-5-7. Plagioclase abundances in this sample vary significantly over scales of a few centimeters: modal mineralogy corresponds to a plagioclase-bearing websterite in thin section A (light blue), and to a gabbroic in thin section B (dark blue). Plagioclase occurs as small interstitial grains in thin section A, and as small inclusions in clinopyroxene or as larger grains in thin section B. Dots correspond to microprobe measurements plotted in Figure 9c. Small plagioclase grains (interstitial or inclusions in cpx) have higher An contents than the larger plagioclase grains. This spread of An contents explains the large standard deviation obtained for the average plagioclase An content in this sample (diagram a).

**Table 6.** Major Element Compositions (wt%) of Clinopyroxenes of Representative Plagioclase-Bearing Ultramafic and Gabbroic Rocks<sup>a</sup>

	SMS6-2-1		SMS6-5-2		SMS6-5-7		SMS7-4-2		SMS17-4-22		SMS17-5-6		SMS29-3-9		ED21-10-3		ED23-3-6	
	Core		Core		Core		Core		Core		Core		Core		Core		Core	
	(n=17)	±	(n=5)	±	(n=36)	±	(n=5)	±	(n=13)	±	(n=16)	±	(n=16)	±	(n=8)	±	(n=7)	±
SiO <sub>2</sub>	51.69	0.48	50.91	0.98	51.51	1.11	52.52	0.72	50.92	1.00	50.81	0.50	51.06	0.60	52.79	0.75	51.19	0.61
TiO <sub>2</sub>	0.78	0.09	0.46	0.03	0.43	0.08	0.40	0.10	0.68	0.17	0.57	0.11	0.51	0.13	0.34	0.09	0.35	0.02
Al <sub>2</sub> O <sub>3</sub>	4.16	0.60	5.99	1.13	4.44	1.54	3.35	0.99	5.45	1.45	5.71	0.74	4.93	1.07	3.02	0.83	5.76	0.39
FeO <sub>tot</sub>	3.47	0.28	3.13	0.09	3.39	0.32	2.95	0.23	2.76	0.09	3.76	0.84	3.63	0.78	3.09	0.25	3.12	0.36
MnO	0.13	0.03	0.07	0.01	0.11	0.04	0.10	0.01	0.12	0.02	0.10	0.05	0.11	0.04	0.11	0.06	0.09	0.05
MgO	16.20	0.47	15.58	0.59	16.03	0.78	16.86	0.41	15.81	0.64	16.16	2.12	16.92	1.59	17.10	0.55	16.68	1.45
CaO	22.62	0.78	22.80	0.65	22.55	0.98	22.21	0.73	22.38	0.40	20.97	3.03	21.15	2.68	22.19	0.74	21.14	1.44
Na <sub>2</sub> O	0.51	0.07	0.46	0.02	0.42	0.09	0.43	0.09	0.51	0.03	0.57	0.14	0.35	0.04	0.36	0.06	0.48	0.06
K <sub>2</sub> O	0.01	0.01	0.01	0.00	0.01	0.01	0.01	0.01	0.01	0.01	0.01	0.01	0.01	0.01	0.01	0.01	0.01	0.01
Cr <sub>2</sub> O <sub>3</sub>	0.32	0.08	0.96	0.02	0.78	0.26	0.86	0.16	0.56	0.20	1.23	0.09	0.69	0.16	0.71	0.18	1.29	0.05
NiO	0.04	0.03	0.04	0.01	0.05	0.03	0.07	0.04	0.04	0.02	0.06	0.04	0.05	0.02	0.02	0.01	0.06	0.04
Cl	0.00	0.00	0.00	0.00	0.01	0.01	0.01	0.01	0.01	0.01	0.01	0.03	0.00	0.00	0.00	0.00	0.00	0.00
F	0.04	0.09	0.09	0.17	0.04	0.05	0.04	0.04	0.03	0.05	0.04	0.07	0.11	0.11	0.01	0.02	0.01	0.02
Total	99.97	0.45	100.51	0.59	99.76	0.53	99.78	0.17	99.28	0.45	100.01	0.54	99.53	0.34	99.75	0.58	100.17	0.20
X <sub>Mg</sub>	88.92	0.63	89.67	0.31	89.11	0.61	90.84	0.70	90.72	0.53	88.28	0.90	89.06	1.22	90.48	0.85	90.25	0.34
X <sub>Fe</sub>	10.67	0.63	10.10	0.29	10.56	0.60	8.87	0.67	8.90	0.52	11.41	0.88	10.60	1.18	9.19	0.79	9.46	0.39
X <sub>Cr</sub>	0.05	0.01	0.10	0.02	0.11	0.03	0.15	0.02	0.07	0.03	0.13	0.02	0.09	0.03	0.14	0.01	0.13	0.01
Cr#	9.04		17.23		18.48		24.92		11.73		21.80		15.39		23.35		22.46	

<sup>a</sup>Average composition of several clinopyroxene grains in each sample. Error bars: ±1 std.

Table 6 and supporting information Table S4 (see supporting information Figures S1 and S2), correspond to crystal cores. Clinopyroxenes rims have very similar compositions except for lower CaO contents.

### 5.2.3. Orthopyroxene

Orthopyroxenes are present as porphyroclasts, as inclusions in clinopyroxenes, as small grains that are probably relicts of partially reacted porphyroclasts, and as reaction rims between olivine and plagioclase. Mg# are similar for all orthopyroxene types (from 87.59 to 90.14 wt%), and similar to those reported for orthopyroxenes in plagioclase-free peridotites of the same region (from 89.29 to 92.14 wt% [Seyler *et al.*, 2003]). Orthopyroxene reaction rims stand out by distinctly lower Al<sub>2</sub>O<sub>3</sub> and TiO<sub>2</sub> contents (Table 7 and supporting information Table S5). As in clinopyroxenes, the Cr<sub>2</sub>O<sub>3</sub> content of orthopyroxenes is lower in plagioclase websterites than in plagioclase lherzolites, and spans the whole range (0.20 to 0.87 wt%) in plagioclase-rich samples (troctolites, olivine gabbros, gabbros; see supporting information Figure S3). Also similar to clinopyroxenes, orthopyroxene rims are similar in composition to orthopyroxene cores, except for lower CaO contents. The values reported in Table 7 correspond to crystal cores.

**Table 7.** Major Element Compositions (wt%) of Orthopyroxenes of Representative Plagioclase-Bearing Ultramafic and Gabbroic Rocks<sup>a</sup>

	SMS6-2-1				SMS6-5-2				SMS6-5-7				SMS17-4-22		SMS17-5-6		SMS29-3-9		ED23-3-6	
	Core		Secondary rim		Core		Secondary rim		Core		Secondary rim		Core		Core		Core		Core	
	(n=12)	±	(n=3)	±	(n=11)	±	(n=4)	±	(n=48)	±	(n=4)	±	(n=13)	±	(n=14)	±	(n=1)	±	(n=8)	±
SiO <sub>2</sub>	55.82	0.89	57.33	0.34	55.15	1.03	57.92	0.46	55.06	0.98	53.87	0.44	55.33	0.80	54.57	0.88	53.00	0.45	55.63	0.80
TiO <sub>2</sub>	0.24	0.07	0.05	0.03	0.18	0.03	0.04	0.03	0.17	0.05	0.06	0.05	0.23	0.07	0.18	0.04	0.14	0.03	0.15	0.02
Al <sub>2</sub> O <sub>3</sub>	2.10	1.10	0.64	0.35	4.05	1.46	0.63	0.28	2.94	0.84	1.36	1.03	3.39	1.00	4.01	1.21	6.81	0.13	3.51	0.84
FeO <sub>tot</sub>	9.03	0.77	7.93	0.14	7.24	0.26	7.53	0.25	7.79	0.53	7.70	0.29	6.36	0.28	7.82	0.29	7.05	0.38	6.47	0.24
MnO	0.22	0.04	0.22	0.02	0.14	0.03	0.16	0.04	0.18	0.03	0.27	0.06	0.16	0.03	0.17	0.03	0.17	0.02	0.14	0.03
MgO	32.11	0.54	34.14	0.23	32.30	1.01	34.47	0.32	31.98	0.50	32.80	0.77	32.61	0.58	31.66	0.64	30.24	1.67	33.38	0.61
CaO	0.79	0.27	0.13	0.02	1.01	0.55	0.31	0.04	1.02	0.40	0.46	0.19	1.12	0.41	0.93	0.28	2.34	2.58	0.93	0.19
Na <sub>2</sub> O	0.01	0.01	0.01	0.00	0.03	0.03	0.00	0.00	0.02	0.02	0.02	0.02	0.03	0.02	0.03	0.02	0.03	0.04	0.02	0.01
K <sub>2</sub> O	0.01	0.00	0.01	0.01	0.01	0.01	0.01	0.01	0.01	0.01	0.00	0.01	0.01	0.01	0.01	0.01	0.01	0.01	0.00	0.00
Cr <sub>2</sub> O <sub>3</sub>	0.20	0.08	0.01	0.01	0.62	0.17	0.02	0.01	0.62	0.08	0.18	0.24	0.29	0.11	0.87	0.14	0.30	0.03	0.78	0.19
NiO	0.07	0.03	0.06	0.03	0.08	0.02	0.06	0.03	0.09	0.04	0.07	0.05	0.10	0.03	0.09	0.04	0.06	0.04	0.08	0.04
Cl	0.00	0.00	0.00	0.00	0.01	0.01	0.01	0.00	0.01	0.01	0.01	0.01	0.01	0.01	0.01	0.00	0.01	0.01	0.00	0.00
F	0.02	0.03	0.01	0.03	0.03	0.04	0.19	0.18	0.03	0.07	0.00	0.00	0.01	0.01	0.01	0.02	0.03	0.04	0.01	0.02
Total	100.64	0.29	100.54	0.19	100.85	0.39	101.36	0.10	100.03	0.79	98.91	0.42	99.65	0.43	100.35	0.84	100.19	0.83	101.08	0.34
X <sub>Mg</sub>	86.09	1.10	88.19	0.19	88.62	0.45	88.87	0.34	87.74	0.73	88.00	0.57	89.90	0.43	87.59	0.39	88.18	0.24	90.01	0.30
X <sub>Fe</sub>	13.58	1.06	11.49	0.20	11.15	0.45	10.89	0.32	11.98	0.74	11.59	0.49	9.84	0.41	12.14	0.39	11.54	0.22	9.79	0.30
X <sub>Cr</sub>	0.07	0.02	0.02	0.01	0.10	0.02	0.03	0.01	0.13	0.02	0.06	0.04	0.05	0.01	0.13	0.03	0.03	0.00	0.13	0.01
Cr#	10.92		2.24		16.43		4.77		21.38		14.58		9.98		21.80		5.45		22.22	

<sup>a</sup>Average composition of several orthopyroxene grains in each sample. Error bars: ±1 std.

### 5.2.4. Olivine

Fo contents in olivine (cores and rims) range between 86.97 and 90.13% (Table 8 and supporting information Table S6). As in the case of clinopyroxenes and orthopyroxenes, there is no systematic difference in Fo contents between plagioclase-bearing lherzolites, plagioclase-bearing websterites and troctolites, olivine gabbros and gabbros. Several samples, including two olivine gabbros, contain olivine with Fo contents in the range of values measured in olivine from plagioclase-free peridotites from the same region (89.28 to 90.73% [Seyler *et al.*, 2003]). Other samples contain olivine with slightly lower Fo contents (86.97 to 88.66%) (see supporting information Figure S4). Fo contents in plagioclase lherzolites show the highest values (87.90 to 90.13%); Fo contents in plagioclase websterites range from between 87.88 to 89.71%; Fo values in troctolites and olivine gabbros are between 86.97 and 89.64% (Table 8 and supporting information Table S6). Olivine NiO (0.29–0.40 wt%) and MnO (0.12–0.22 wt%) contents are similar in all samples and within the range measured in olivine from plagioclase-free peridotites from the same region (between 0.32 and 0.43 wt% for NiO, and between 0.09 and 0.19 wt% for MnO [Seyler *et al.*, 2003]).

### 5.2.5. Spinel

The Mg# of spinel in the plagioclase-bearing ultramafic samples spans a range from 49.38 to 76.17% (Figure 10; Table 9 and supporting information Table S7). As in the case of pyroxenes and olivine, there is no correlation between the Mg# of the spinels and plagioclase An contents. In terms of their Mg#, Cr# and TiO<sub>2</sub> content, most spinels in these samples plot between the spinels of plagioclase-free lherzolites in the same region [Seyler *et al.*, 2003], and the spinels of troctolites from the MAR [Drouin *et al.*, 2009]. Spinel in the plagioclase-bearing ultramafic samples have lower Mg# (49.38 to 64.13%), Al<sub>2</sub>O<sub>3</sub> (31.74 to 37.38 wt%) and MgO (11.85 to 15.73 wt%) contents, and higher Cr# (33.65 to 40.97%), TiO<sub>2</sub> (0.29 to 0.79 wt%) and FeO (15.53 to 21.59 wt%) contents, than spinels from plagioclase-free lherzolites [Seyler *et al.*, 2003]. However, spinels in three samples (two plagioclase-bearing websterites: SMS17-4-22 and SMS29-3-9, and an olivine gabbro: SMS6-2-1) plot within the ranges of plagioclase-free lherzolites (Figure 10).

## 5.3. Mineral Trace Element Composition

### 5.3.1. Clinopyroxene

Clinopyroxenes in the plagioclase-bearing ultramafic to gabbroic suite have LREE-depleted REE patterns, with (La/Sm)<sub>n</sub> between 0.01 and 0.16 (Figure 11a and Table 10). The HREE part of these patterns is nearly flat, with (Sm/Yb)<sub>n</sub> ratios between 0.79 and 0.91. These clinopyroxene REE patterns are enriched in LREE relative to plagioclase-free residual lherzolites from the same region ((La/Sm)<sub>n</sub> from 0.009 to 0.035 [Seyler *et al.*, 2011]). Clinopyroxenes in the plagioclase-bearing lherzolites and websterites have very similar patterns, with no Eu anomaly. They are more depleted than clinopyroxenes from most analyzed troctolites, olivine gabbros and gabbros (Figure 11a). These plagioclase-rich lithologies have parallel REE patterns with distinct Eu anomalies. They also have higher Sr and Zr contents (9.8 to 25.4 ppm for Sr; 8.3 to 24.2 ppm for Zr) than the analyzed plagioclase-bearing websterite and lherzolite (5.5 ppm and 6.2 ppm respectively for Sr; 7.7

**Table 8.** Major Element Compositions (wt%) of Olivines of Representative Plagioclase-Bearing Ultramafic and Gabbroic Rocks<sup>a</sup>

	SMS6-2-1 Core		SMS6-5-2 Core		SMS6-5-7 Core		SMS7-4-2 Core		SMS17-4-22 Core		SMS17-5-6 Core		ED21-10-3 Core		ED23-3-6 Core	
	(n=17)	±	(n=23)	±	(n=10)	±	(n=10)	±	(n=6)	±	(n=4)	±	(n=4)	±	(n=15)	±
SiO <sub>2</sub>	40.58	0.36	40.92	0.24	40.29	0.21	40.93	0.30	40.75	0.28	40.95	0.37	40.33	0.39	41.11	0.36
TiO <sub>2</sub>	0.01	0.01	0.01	0.01	0.02	0.01	0.02	0.01	0.04	0.04	0.02	0.01	0.02	0.01	0.02	0.01
Al <sub>2</sub> O <sub>3</sub>	0.01	0.01	0.01	0.01	0.01	0.01	0.01	0.01	0.01	0.01	0.02	0.02	0.00	0.00	0.01	0.01
FeO <sub>tot</sub>	12.44	0.98	11.05	0.32	11.18	0.43	10.88	0.21	9.72	0.28	11.37	0.27	11.48	0.20	9.58	0.15
MnO	0.19	0.03	0.14	0.03	0.22	0.03	0.18	0.02	0.18	0.02	0.15	0.04	0.17	0.03	0.14	0.04
MgO	47.32	0.79	48.17	0.47	47.47	0.78	47.64	0.40	48.43	0.33	47.21	0.54	47.48	0.31	49.79	0.29
CaO	0.02	0.01	0.04	0.01	0.02	0.01	0.04	0.01	0.03	0.01	0.03	0.00	0.04	0.01	0.05	0.02
Na <sub>2</sub> O	0.00	0.01	0.01	0.01	0.00	0.00	0.01	0.01	0.01	0.01	0.00	0.01	0.03	0.04	0.02	0.03
K <sub>2</sub> O	0.01	0.00	0.01	0.01	0.01	0.01	0.01	0.01	0.01	0.00	0.01	0.01	0.01	0.02	0.01	0.02
Cr <sub>2</sub> O <sub>3</sub>	0.01	0.01	0.01	0.01	0.01	0.01	0.01	0.01	0.01	0.00	0.01	0.02	0.02	0.01	0.00	0.01
NiO	0.37	0.03	0.38	0.05	0.39	0.07	0.34	0.04	0.38	0.04	0.32	0.05	0.29	0.04	0.35	0.03
Cl	0.00	0.00	0.00	0.00	0.01	0.01	0.01	0.01	0.01	0.01	0.00	0.00	0.00	0.00	0.01	0.02
F	0.03	0.04	0.03	0.07	0.01	0.02	0.02	0.05	0.02	0.02	0.00	0.00	0.00	0.00	0.01	0.03
Total	100.99	0.36	100.79	0.59	99.64	0.96	100.07	0.55	99.58	0.31	100.10	0.58	99.85	0.51	101.08	0.27
Fo %	86.97	1.08	88.47	0.32	88.12	0.47	88.48	0.16	89.71	0.30	87.95	0.36	87.90	0.22	90.13	0.13

<sup>a</sup>Average composition of several olivine grains in each sample. Error bars: ± 1 std.

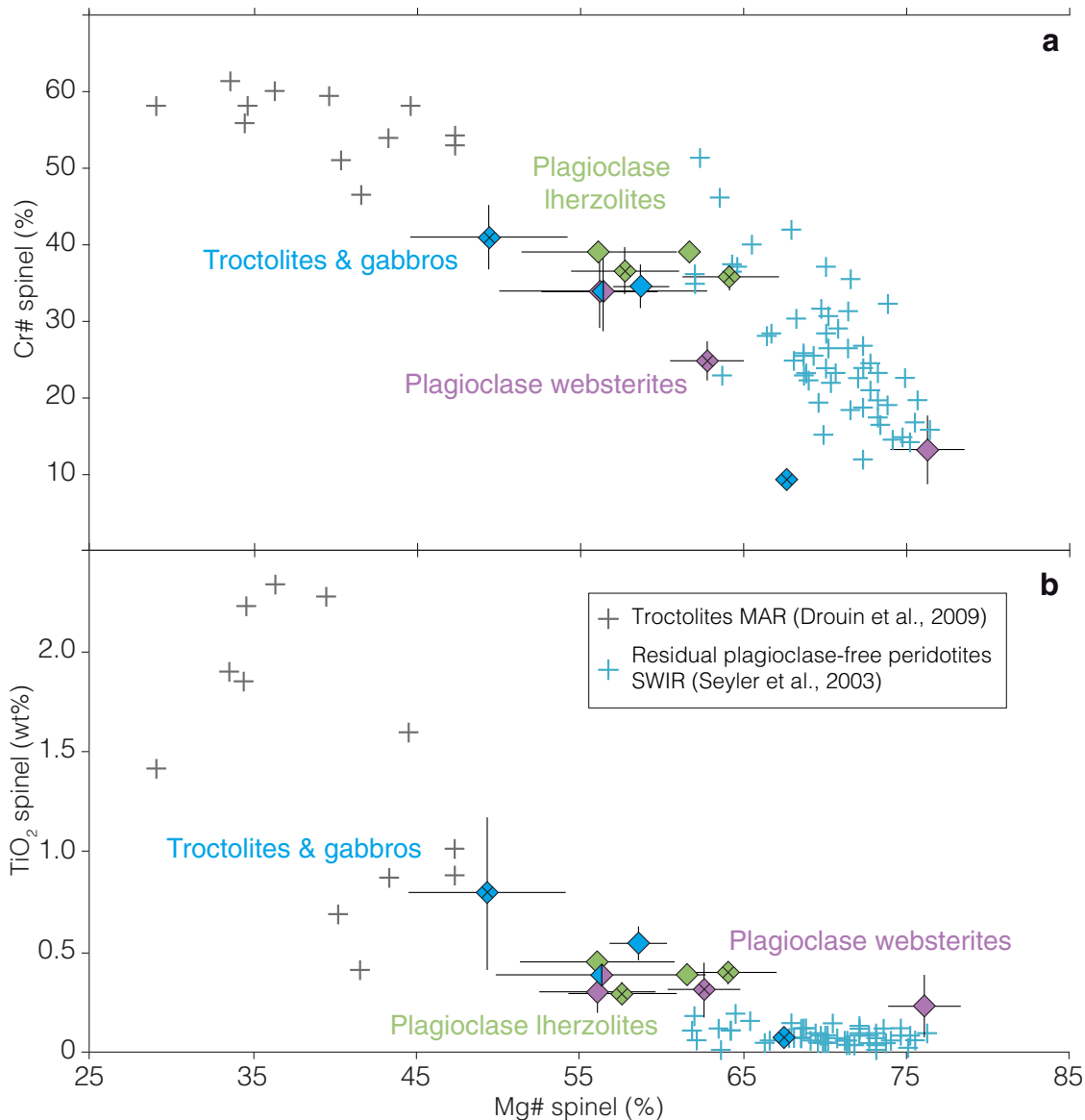


**Figure 10.** Spinel major element composition in samples of the plagioclase-bearing ultramafic to gabbroic suite. (a) Cr# and (b) TiO<sub>2</sub> content as a function of Mg#. Diamond data point corresponds to the average composition of several spinel grains in each sample (n values in Table 9). Error bars: ± 1 std. Same symbols as in Figure 8. Spinel in the samples describe the whole range defined by the spinels in residual plagioclase-free peridotites from the SWIR and in troctolites from the MAR, with an increase of Cr#, and TiO<sub>2</sub> content as the Mg# decreases.

ppm and 8.7 ppm respectively for Zr; Table 10). Among the troctolites, olivine gabbros and gabbros, the highest Sr contents tend to correspond to the lowest Zr contents, and to the most depleted REE patterns.

### 5.3.2. Orthopyroxene

Orthopyroxenes have LREE-depleted patterns, characterized by a steep decrease from HREE to LREE (Figure 11a and Table 10). These patterns are similar in all the analyzed rock types (plagioclase-bearing Iherzolites, plagioclase-bearing websterites, troctolites, olivine gabbros, and gabbros) and also similar to the REE composition of orthopyroxenes from plagioclase-free residual Iherzolites from the same region [Seyler *et al.*, 2011]. Orthopyroxenes in the plagioclase-bearing samples also have positive anomalies in Zr and Ti, which are typical in orthopyroxenes from residual peridotites [Rampone *et al.*, 1991].

### 5.3.3. Plagioclase

Plagioclase REE compositions have been measured only in the plagioclase-rich rock types (troctolites, olivine gabbros and gabbros) because plagioclase grains in the plagioclase-bearing Iherzolites and websterites were too small to be analyzed by LA-ICP-MS. The four analyzed samples have low plagioclase HREE contents ( $Yb_n = 0.01$ –

**Table 9.** Major Element Compositions (wt%) of Spinels of Representative Plagioclase-Bearing Ultramafic and Gabbroic Rocks<sup>a</sup>

	SMS6-2-1 Core		SMS6-5-2 Core		SMS6-5-7 Core		SMS17-4-22 Core		SMS17-5-6 Core		SMS29-3-9 Core		ED23-3-6 Core	
	(n=1)	±	(n=15)	±	(n=7)	±	(n=2)	±	(n=4)	±	(n=3)	±	(n=5)	±
SiO <sub>2</sub>	0.04	-	0.04	0.03	0.04	0.02	0.09	0.01	0.03	0.02	0.00	0.00	0.06	0.03
TiO <sub>2</sub>	0.07	-	0.30	0.10	0.38	0.08	0.23	0.15	0.54	0.08	0.31	0.14	0.29	0.05
Al <sub>2</sub> O <sub>3</sub>	56.64	-	37.38	3.48	37.15	4.28	54.79	3.47	36.05	2.14	43.72	2.21	35.76	2.59
FeO <sub>tot</sub>	15.33	-	19.25	1.33	18.77	2.54	11.01	0.87	18.62	0.59	17.32	0.84	18.49	1.44
MnO	0.00	-	0.00	0.00	0.00	0.01	0.00	0.00	0.00	0.00	0.00	0.00	0.17	0.10
MgO	17.97	-	13.85	1.08	13.64	1.70	19.76	0.92	14.83	0.60	16.39	0.77	14.28	0.88
CaO	0.02	-	0.02	0.02	0.03	0.03	0.03	0.03	0.01	0.00	0.00	0.00	0.02	0.03
Na <sub>2</sub> O	0.03	-	0.01	0.01	0.01	0.01	0.01	0.02	0.01	0.01	0.00	0.00	0.01	0.02
K <sub>2</sub> O	0.00	-	0.01	0.01	0.01	0.00	0.01	0.00	0.01	0.01	0.01	0.01	0.01	0.01
Cr <sub>2</sub> O <sub>3</sub>	8.77	-	28.13	3.17	28.17	3.36	12.41	4.13	28.22	1.85	21.29	1.73	30.54	1.77
NiO	0.30	-	0.20	0.08	0.16	0.05	0.34	0.03	0.21	0.01	0.22	0.03	0.15	0.02
Cl	0.00	-	0.01	0.01	0.01	0.01	0.00	0.01	0.00	0.00	0.00	0.00	0.00	0.00
F	0.30	-	1.08	0.41	1.02	0.25	0.63	0.31	0.52	0.02	0.86	0.37	0.17	0.37
Total	99.48	-	100.26	0.85	99.38	0.44	99.33	0.41	99.03	0.47	100.11	0.35	99.94	0.29
X <sub>Mg</sub>	67.63	-	56.15	3.57	56.36	6.41	76.17	2.28	58.65	1.75	62.72	2.24	57.68	3.32
X <sub>Cr</sub>	9.41	-	33.65	4.58	33.89	5.29	13.22	4.53	34.46	2.80	24.79	2.57	36.48	3.01

<sup>a</sup>Average composition of several spinel grains in each sample. Error bars: ±1 std.

0.2), LREE-enriched patterns with strong Eu anomalies. Two samples display more enriched patterns, with slightly flatter HREE portions ((Sm/Yb)<sub>n</sub> = 3.3). The other two samples show more depleted plagioclase REE patterns, with steeper slopes for the HREE parts of the patterns ((Sm/Yb)<sub>n</sub> = 12.5–15.6). The most enriched REE patterns correspond to plagioclase with An contents ≤60% (Figure 8) and to samples with the most REE-enriched clinopyroxenes (Figure 11a).

#### 5.4. Calculated REE Composition of Melts in Equilibrium With Clinopyroxene and Plagioclase

The range of REE compositions for melts calculated to be in equilibrium with the clinopyroxenes of the plagioclase-bearing ultramafic rocks, using clinopyroxene/liquid partition coefficients from *Bédard* [2014], is shown in Figure 12. Using clinopyroxene/liquid partition coefficients from *Lee et al.* [2007] results in more enriched calculated melts, particularly in LREE (supporting information Figure S5). In both cases, melts calculated to be in equilibrium with the clinopyroxenes of most samples (Figure 12) have flat REE patterns and abundances similar to those of most basalts sampled in the study area (all of the ultramafic seafloor basalts and most basalts from the volcanic seafloor domains; Figure 4a). The REE compositions of melts calculated to be in equilibrium with plagioclase (using plagioclase/liquid partition coefficients from *Bédard* [1994, 2006]) are inconsistent for HREE. We note that a similar inconsistency was found for melt REE compositions calculated from clinopyroxene and plagioclase REE patterns in troctolites and olivine gabbros from other abyssal [*Drouin et al.*, 2009] and ophiolitic (data not shown: *Kelemen et al.* [1997], *Borghini et al.* [2007], *Borghini and Rampone* [2007], *Renna and Tribuzio* [2011]) locations. This suggests that the available plagioclase/liquid partition coefficients are possibly not appropriate for HREE.

### 6. Discussion

Most basalts dredged from the sparse volcanic cover of nearly amagmatic corridors in the 61°–67°E region of the SWIR (“ultramafic seafloor basalts”) have significantly lower CaO contents at a given MgO (Figure 3b) than most basalts dredged from the intervening, more volcanically active domains (“volcanic seafloor basalts”). Ultramafic seafloor basalts also tend to have higher Na<sub>2</sub>O and TiO<sub>2</sub> contents (Figures 3a and 3f), and lower Al<sub>2</sub>O<sub>3</sub> and FeO contents (Figures 3c and 3d) at a given MgO content. These characteristics cannot be collectively explained by invoking a lower degree of mantle melting beneath the nearly amagmatic spreading corridors: Na<sub>2</sub>O and TiO<sub>2</sub> contents would then be higher, but so would Al<sub>2</sub>O<sub>3</sub> contents. Moreover, ultramafic seafloor basalts also have isotopic and trace element compositions similar to most volcanic seafloor basalts (Tables 2 and 3; Figure 4), which is consistent with the idea that these two groups of basalts derive from similar degrees of melting of a common mantle source.

Plagioclase-bearing ultramafic and gabbroic rocks, dredged at several locations in the nearly amagmatic spreading corridors (Figure 1), represent a small fraction of the rocks dredged in these corridors (<4% in

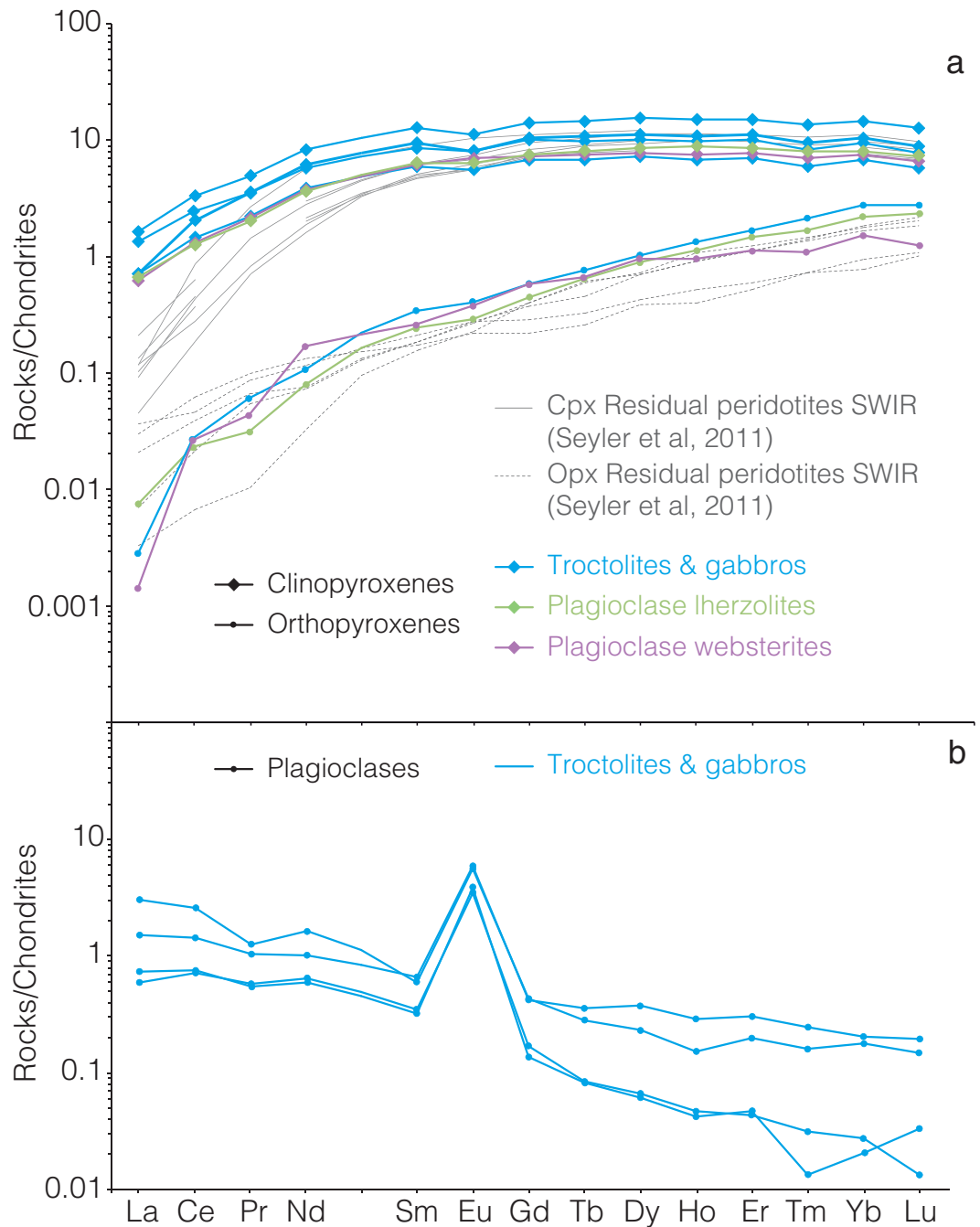


**Figure 11.** (a) Chondrite-normalized Rare Earth Element (REE) concentrations in clinopyroxenes and orthopyroxenes, and (b) in plagioclases in samples of the plagioclase-bearing ultramafic to gabbroic suite for the 61°–67°E SWIR region. Each line corresponds to the average composition of several grains (n values in Table 10) in each sample. Normalizing values of McDonough and Sun [1995]. Data are colored according to modal mineralogy of the sample: plagioclase-bearing lherzolites in green, plagioclase-bearing websterites in purple, troctolites, olivine gabbros and gabbros in blue. Thin grey lines in (a) show the composition of clinopyroxenes and orthopyroxenes in plagioclase-free ultramafic rocks from the same region [Seyler et al., 2011]. Orthopyroxenes in the plagioclase-bearing samples have LREE-depleted compositions similar to orthopyroxenes in these plagioclase-free samples. By contrast, clinopyroxenes compositions in the plagioclase-bearing ultramafic to gabbroic rock suite are enriched in LREE compared to clinopyroxenes in plagioclase-free samples. Plagioclase REE have been measured only in the plagioclase-rich rock types (troctolites, olivine gabbros and gabbros).

volume against 96% for plagioclase-free ultramafic rocks [Sauter et al., 2013]). They show impregnation and melt/rock reaction textures such as interstitial plagioclase lenses, rims of secondary orthopyroxene between olivine and plagioclase (Figure 7e), replacement of primary orthopyroxene by clinopyroxene (Figures 7b–7d), and clinopyroxenes with plagioclase and orthopyroxene inclusions. The transition from plagioclase-free to

**Table 10.** Trace Element Compositions (ppm) of Clinopyroxenes, Orthopyroxenes, and Plagioclases of Plagioclase-Bearing Ultramafic and Gabbroic Rocks<sup>a</sup>

	SMS56-2-1			SMS15-3-20			SMS521-3-1			SMS29-3-9			ED21-10-3			ED23-3-6								
	Cpx Core	Pl Core	±	Cpx Core	Opx Core	±	Cpx Core	Pl Core	±	Cpx Core	Opx Core	±	Cpx Core	Pl Core	±	Cpx Core	Opx Core	±						
Sc	75.7	11.0	0.8	0.2	73.2	6.8	35.9	-	0.7	0.3	78.7	3.0	53.1	21.7	17.1	-	62.1	22.0	0.9	0.3	53.0	9.0	29.1	2.2
Ti	3127	204	437	229	2309	256	862	-	157	70	2289	392	1823	362	868	-	1553	545	152	4	1618	177	752	44
V	348.6	36.6	3.8	4.3	284.6	28.1	142.0	-	0.6	0.5	332.4	4.1	255.4	108.4	103.3	-	264.3	101.6	1.1	0.1	237.4	22.0	136.2	8.1
Cr	2938.0	1601.2	0.2	0.2	8950.3	670.5	5432.8	-	0.1	0.1	1668.0	522.9	2824.9	722.1	2444.2	-	4115.9	1691.9	0.7	0.7	7691.1	167.5	5105.3	451.8
Mn	927.6	97.4	67.9	82.4	840.1	100.9	1217.5	-	18.4	23.1	940.9	99.0	1076.8	59.8	1080.3	-	773.0	190.3	17.5	0.8	694.0	68.7	993.5	60.5
Co	25.8	1.6	1.5	2.1	23.8	3.0	54.6	-	0.4	0.6	28.8	2.1	25.8	2.4	57.1	-	23.0	8.6	0.2	0.0	23.8	3.1	50.2	1.7
Ni	315.1	13.6	25.1	35.5	321.8	38.1	606.7	-	6.0	10.3	398.7	33.4	313.8	29.6	642.9	-	290.4	161.3	1.7	2.4	386.4	26.5	674.7	23.3
Zn	7.32	0.82	0.78	0.81	5.06	1.57	15.64	-	0.16	0.05	16.87	2.37	5.17	0.65	12.71	-	14.44	3.53	1.16	0.21	5.09	1.48	15.36	0.41
Rb	n.d.	n.d.	0.16	0.10	0.03	0.07	n.d.	-	0.16	0.15	0.03	0.05	n.d.	n.d.	0.02	-	0.11	0.22	0.05	0.04	n.d.	n.d.	n.d.	n.d.
Sr	9.80	0.47	265.08	8.74	7.99	1.22	0.28	-	275.95	45.55	12.80	1.54	329.67	5.50	3.63	0.18	25.40	50.87	232.83	7.04	6.23	2.00	0.08	0.04
Y	20.42	1.47	0.49	0.46	14.88	2.00	1.86	-	0.08	0.03	13.64	1.79	10.16	2.16	1.49	-	9.48	4.02	0.08	0.00	11.91	1.32	1.75	0.17
Zr	24.22	3.85	0.05	0.07	16.14	3.15	1.67	-	0.01	0.01	11.72	6.14	7.68	1.69	2.74	-	8.26	4.00	0.09	0.12	8.72	1.54	1.46	0.23
Nb	0.048	0.012	0.001	0.002	0.009	0.006	0.000	-	0.001	0.001	0.028	0.025	0.005	0.004	0.003	-	0.008	0.004	0.003	0.004	0.016	0.012	0.002	0.001
Ba	0.021	0.011	1.183	0.078	0.103	0.082	0.030	-	4.450	5.135	0.364	0.604	0.083	0.104	0.007	-	0.395	0.722	2.571	0.338	0.008	0.010	0.002	0.002
La	0.386	0.076	0.361	0.057	0.167	0.031	0.001	-	0.142	0.045	0.317	0.111	0.147	0.407	0.000	-	0.166	0.013	0.177	0.012	0.158	0.028	0.002	0.002
Ce	2.024	0.304	0.891	0.054	1.214	0.148	0.044	-	0.447	0.110	1.477	0.407	0.803	0.190	0.016	-	0.872	0.218	0.467	0.001	0.764	0.109	0.014	0.004
Pr	0.458	0.063	0.096	0.004	0.322	0.044	0.006	-	0.054	0.016	0.320	0.082	0.200	0.039	0.004	-	0.205	0.068	0.275	0.009	0.186	0.019	0.003	0.001
Nd	3.727	0.407	0.461	0.099	2.798	0.317	0.049	-	0.292	0.075	2.632	0.594	1.715	0.291	0.078	-	1.754	0.655	0.275	0.008	1.624	0.156	0.037	0.016
Sm	1.866	0.179	0.100	0.040	1.380	0.173	0.051	-	0.194	0.040	1.445	0.019	0.905	0.148	0.039	-	0.316	0.071	0.215	0.025	0.362	0.037	0.016	0.005
Eu	0.620	0.056	0.333	0.003	0.446	0.043	0.023	-	0.034	0.002	0.445	0.019	0.398	0.049	0.021	-	0.316	0.071	0.215	0.025	0.362	0.037	0.016	0.005
Gd	2.843	0.194	0.084	0.038	2.115	0.311	0.116	-	0.034	0.018	1.980	0.298	1.428	0.250	0.117	-	1.346	0.584	0.228	0.003	1.501	0.181	0.090	0.019
Tb	0.532	0.040	0.013	0.009	0.384	0.060	0.027	-	0.003	0.002	0.353	0.045	0.267	0.053	0.024	-	0.245	0.106	0.003	0.001	0.290	0.039	0.023	0.005
Dy	3.800	0.245	0.093	0.072	2.756	0.385	0.254	-	0.016	0.007	2.527	0.318	1.892	0.425	0.238	-	1.762	0.751	0.015	0.005	2.124	0.231	0.217	0.036
Ho	0.831	0.061	0.016	0.014	0.596	0.091	0.072	-	0.003	0.001	0.536	0.060	0.410	0.098	0.052	-	0.370	0.157	0.002	0.000	0.476	0.055	0.061	0.011
Er	2.434	0.174	0.049	0.041	1.759	0.257	0.269	-	0.007	0.003	1.603	0.163	1.221	0.304	0.180	-	1.116	0.469	0.008	0.001	1.392	0.160	0.235	0.042
Tm	0.336	0.023	0.006	0.005	0.235	0.037	0.052	-	0.001	0.001	0.206	0.022	0.171	0.039	0.027	-	0.147	0.061	0.000	0.000	0.197	0.019	0.042	0.006
Yb	2.356	0.143	0.033	0.041	1.676	0.198	0.446	-	0.004	0.003	1.534	0.157	1.188	0.255	0.244	-	1.106	0.440	0.003	0.003	1.307	0.161	0.359	0.042
Lu	0.312	0.025	0.005	0.006	0.217	0.033	0.068	-	n.d.	n.d.	0.192	0.021	0.161	0.039	0.030	-	0.143	0.057	0.001	0.000	0.177	0.021	0.058	0.011
Hf	0.834	0.105	0.001	0.002	0.620	0.121	0.085	-	n.d.	n.d.	0.471	0.208	0.342	0.076	0.095	-	0.342	0.179	0.002	0.002	0.380	0.084	0.066	0.015
Pb	0.012	0.009	0.238	0.107	0.005	0.004	0.004	-	0.034	0.020	0.020	0.029	0.005	0.004	n.d.	-	0.028	0.031	0.061	0.012	0.006	0.009	0.001	0.001
Ta	0.004	0.004	n.d.	n.d.	n.d.	n.d.	n.d.	-	n.d.	n.d.	0.003	0.003	0.001	0.001	n.d.	-	n.d.	n.d.	n.d.	n.d.	0.002	0.002	n.d.	n.d.
Th	0.005	0.002	n.d.	n.d.	0.002	0.003	n.d.	-	n.d.	n.d.	0.005	0.008	0.001	0.001	0.001	-	0.003	0.005	0.002	0.003	0.002	0.002	n.d.	n.d.
U	0.002	0.002	n.d.	n.d.	0.001	0.001	n.d.	-	0.001	0.001	0.004	0.007	0.001	0.001	n.d.	-	0.001	0.003	0.001	0.002	0.001	0.001	n.d.	n.d.

<sup>a</sup>Average composition of several grains in each sample. Error bars: ±1 std.

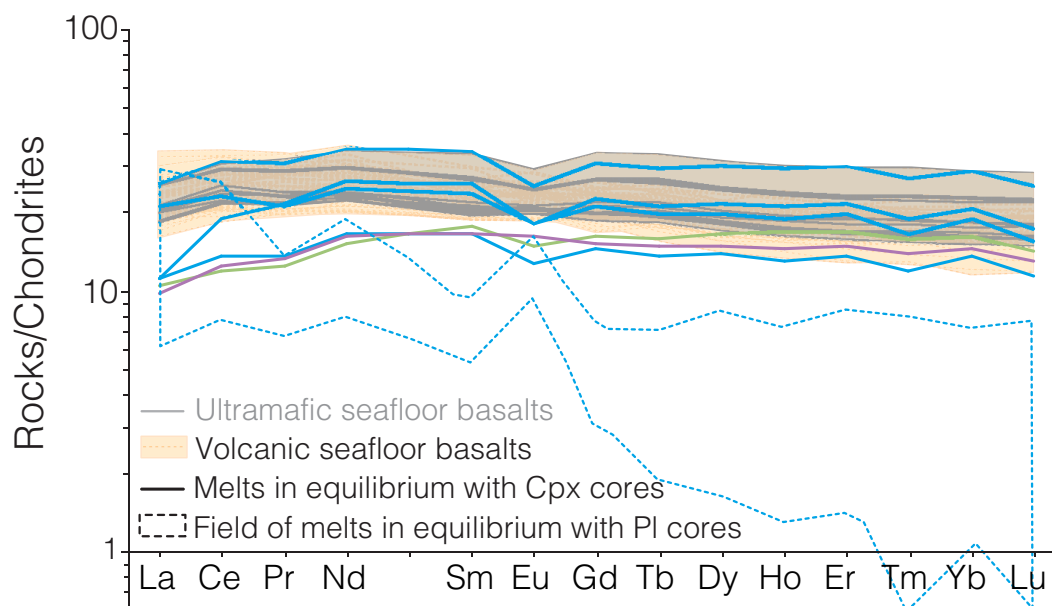


**Figure 12.** Chondrite-normalized Rare Earth Element (REE) concentrations in melts calculated to be in equilibrium with the clinopyroxenes and plagioclases (clinopyroxene/liquid partition coefficients from Bédard [2014]; plagioclase/liquid partition coefficients from Bédard [2006]). Normalizing values of McDonough and Sun [1995]. Data are colored according to modal mineralogy of the sample: plagioclase-bearing lherzolites in green, plagioclase-bearing websterites in purple, troctolites, olivine gabbros and gabbros in blue. The field of ultramafic seafloor basalts and volcanic seafloor basalts (except ED20, ED22 and ED26) (Figure 4a) is shown for comparison.

plagioclase-rich lithologies is commonly observed within a single small sample (e.g., Figures 5b and 5c), suggesting that the melt/rock reactions mostly occurred in centimeter to decimeter-scale irregular veins and impregnations in plagioclase-free lherzolites and websterites. Olivines and orthopyroxenes have major and trace compositions similar to those measured in plagioclase-free residual lherzolites and websterites of the same region [Seyler *et al.*, 2003, 2011; Brunelli *et al.*, 2014]. Clinopyroxenes by contrast have LREE-enriched trace element compositions (Figure 11a). Melts calculated to be in equilibrium with these clinopyroxenes have trace element compositions similar to those of the basalts (Figure 12).

In the first part of the discussion we propose that the differences in major element composition between ultramafic and volcanic seafloor basalts could result from different degrees of reaction between plagioclase-free residual lherzolites and websterites and a common parental melt. We also discuss the implications of this hypothesis in terms of the ridge's magma plumbing system. Being aware that the 61°–67°E region of the SWIR represents a very low melt budget end-member for mid-ocean ridges, we then introduce a discussion of the extent to which our observations in this region may be significant for other, more magmatically active ridges.

### 6.1. A Mass Balance Model of the Effect of Melt/Mantle Interactions on the Major Element Composition of Ultramafic Seafloor Basalts

Textural relations and mineral chemistry in the plagioclase-bearing ultramafic and gabbroic sample suite indicate that:

1. plagioclase and clinopyroxene are the principal mineral products of melt/rock interactions, while olivine, and most orthopyroxene (to the exception of small orthopyroxenes in olivine-plagioclase reaction rims; Figure 7e) are relics of the plagioclase-free protolith. Spinel has amoeboid to vermicular shapes, which is texturally different from residual poikilitic spinel in plagioclase-free ultramafic rocks of the same region [Seyler *et al.*, 2003], and has, with few exceptions, higher Cr# and TiO<sub>2</sub> contents, and lower Mg# (Figure 10). These chemical differences most likely result from partial destabilization of the peridotite's spinel into plagioclase and reequilibration with the melt.
2. although clinopyroxene is clearly secondary (it encloses relics of orthopyroxene and small plagioclase grains) and has enriched trace element compositions (consistent with crystallization from a melt with

trace element compositions similar to those of the basalts; Figure 12), it also has high Mg# (between 88.28 and 90.85%; Figure 8).

These high Mg# values are measured even in samples of troctolite, olivine gabbro and gabbro with plagioclase An contents lower than 65% (Figure 8), a value that typically corresponds in abyssal gabbros to the cocrystallization of clinopyroxene with Mg# between 80 and 85% [e.g., Bloomer *et al.*, 1991; Cannat *et al.*, 1997a, 1997b; Ross and Elthon, 1997; Dick *et al.*, 2002; Miller *et al.*, 2009] (Figure 9). The clinopyroxene Mg# in the plagioclase-bearing samples can be interpreted as having been buffered by the Mg# of the plagioclase-free protolith, as proposed for clinopyroxene in gabbroic veins drilled in serpentinized peridotites next to the Kane Fracture zone (MAR) [Cannat *et al.*, 1997a], implying that the documented melt/rock interactions occurred at low melt/rock ratio.

Taking these observations into account, we now want to test whether the major element composition of the ultramafic seafloor basalts could retain a signature of the documented melt/mantle interactions, and what would then be the range of possible major element compositions for the parent melts. To this end, we develop a simple mass balance model in which we use the modal abundances and the major and trace element composition of the mineral phases in plagioclase-bearing ultramafic to gabbroic rocks and in ultramafic seafloor basalts (inferred products of melt/mantle interaction), and in plagioclase-free residual lherzolites (inferred solid prior to reaction), to reconstruct the composition of the melt prior to reaction.

Two parameters are unknown in these calculations: the composition of the melt prior to the reaction (parent melt), and the melt/mantle ratio, expressed as the ratio of the final mass of melt (i.e., the mass of extracted liquid, that could be erupted) over the initial mass of solid (i.e., the mass of reacting mantle). We allow this ratio to vary between 20 and 500 (Figure 13), and calculate the parent melt composition for each value of the melt/mantle ratio. We also assume that the reactions (dissolution of orthopyroxene and olivine, and crystallization of clinopyroxene and plagioclase) occurred with either no change of solid mass, or with a solid mass change of 100% (see supporting information Text S3 and Table S8). In this second case, which corresponds to more liquid being trapped in the reaction zone, calculated results change in absolute values but not in the general trends (Figure 13).

In the model results shown in Figure 13, we selected spinel lherzolite sample ED21-5-1, representative of residual mantle composition in the study area [Seyler *et al.*, 2003, 2011] as the starting mantle rock. For the reacted rock, we used the modal and chemical composition of olivine gabbro sample SMS17-5-6 (Figures 5c and 7a; Tables 5–10). For the reacted melt, we used the most Mg-rich ultramafic seafloor basalts in dredges SMS16, SMS23 and SMS28 (red, orange and pink triangles in Figure 13) These basalts have relatively depleted REE and trace element compositions with no indication for significant fractional crystallization. Basalts in dredges SMS23 and SMS28 have lower MgO, Na<sub>2</sub>O and Al<sub>2</sub>O<sub>3</sub> contents and slightly higher CaO and FeO contents than the MgO-rich basalts in dredge SMS16.

For melt/rock ratios above 100, the major element composition of the calculated parent melts is not substantially different from that of the reacted melt (ultramafic seafloor basalt). For melt/mantle ratios <100, the calculated parent melts have substantially lower MgO, and higher CaO and Al<sub>2</sub>O<sub>3</sub> contents than the reacted melt. For melt/mantle ratios <60, the parent melt major element compositions plot within the range of most volcanic seafloor basalts (Figure 13).

The REE patterns of the ultramafic seafloor basalts are similar to those of most volcanic seafloor basalts (Figure 4). For the melt/mantle ratios investigated (20 to 500), the REE and TiO<sub>2</sub> contents of the calculated parent melts are not significantly modified relative to the composition of the reacted melts. This includes elements like Sc, Y or transition metals (i.e., Fe/Mn), which are sensitive to reactions of replacement of orthopyroxene or olivine by clinopyroxene; and element pairs such as Sr/Nd, which are sensitive to reactions involving plagioclase fractionation (see supporting information Figure S6).

This mass balance model therefore supports our interpretation that the ultramafic seafloor basalts and the volcanic seafloor basalts are derived from similar parental melts, but that the ultramafic seafloor basalts are more affected by reactions between these parent melts and the mantle rocks in the lithosphere below the ridge. This interpretation is also supported by the observation that ultramafic and volcanic seafloor basalts have similar isotopic compositions, which are indicators in favor of a common mantle source (Table 3).

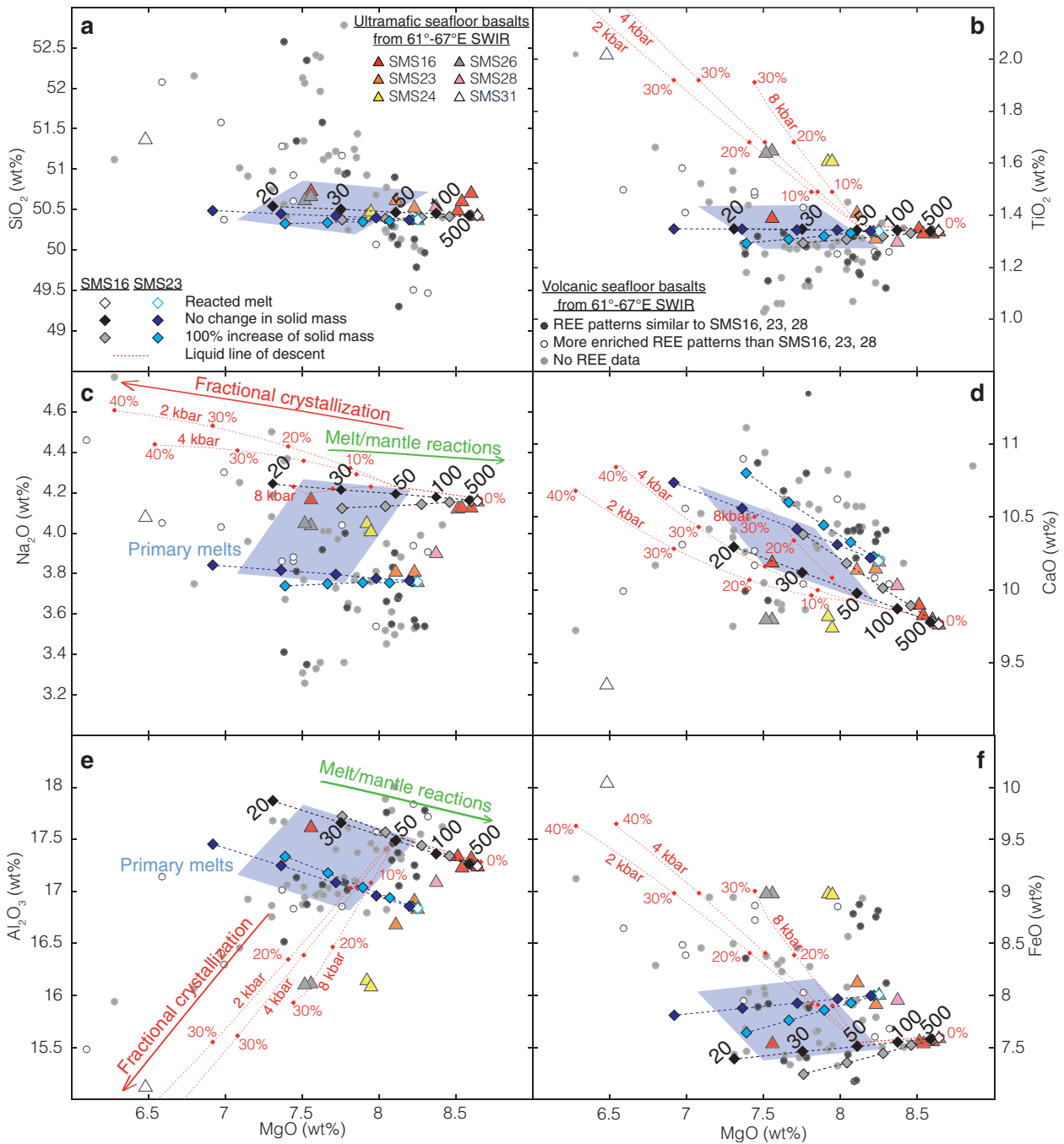


**Figure 13.** Mass balance model of the possible effect of melt/rock interactions in the mantle lithosphere on the major element composition of basalts in the easternmost Southwest Indian Ridge. In this model, we use the modal abundances and major element composition of the mineral phases in the inferred products of melt/mantle interaction (olivine gabbro sample SMS17-5-6 and ultramafic seafloor basalts from dredges SMS16, SMS23 and SMS28), and in the inferred solid prior to reaction (plagioclase-free residual lherzolite: sample ED21-5-1 [Seyler et al., 2003]), to reconstruct the initial composition of the reacting melt (shown here for ultramafic seafloor basalts SMS16-3-5 and SMS23-2-10, respectively as black or dark blue diamonds: no change in solid mass; grey or light blue diamonds: 100% increase of the solid mass). Values from 20 to 500 correspond to the ratio of the final mass of melt (i.e., the mass that could be erupted) over the initial mass of solid (i.e., the initial mass of reacted mantle; see text). For high melt/rock values, reactions have little effect on the melt composition. For lower melt/rock values, the calculated initial composition of the melt has lower MgO and CaO contents, similar to those reported for volcanic seafloor basalts. Shaded domains correspond to the proposed compositional range of the initial reacting melts. (a) SiO<sub>2</sub>, (b) TiO<sub>2</sub>, (c) Na<sub>2</sub>O, (d) CaO, (e) Al<sub>2</sub>O<sub>3</sub> and (f) FeO contents in function of MgO content. Dotted lines correspond to the liquid lines of descent for different crystallization pressures of 2, 4 and 8 kbar calculated with the Petrolog code [Danyushevsky and Plechov, 2011] for a starting composition similar to ultramafic seafloor basalt SMS16-3-5. Red dots along these trends correspond to percent of crystallization. The details of these calculations are given in the supporting information Text S4. The model trends are plotted over the composition of easternmost SWIR basalts shown as dots. White dots correspond to samples with REE patterns that are more enriched than ultramafic seafloor basalts from dredges SMS16, 23 and 28. Dark grey dots correspond to samples with REE patterns similar to ultramafic seafloor basalts from dredges SMS16, 23 and 28. Light grey dots correspond to samples for which trace element data are not available. The very primitive, LREE-depleted, basalts that are shown in grey symbols in Figure 3 are not represented here.

Mg-rich and REE-depleted ultramafic seafloor basalts in dredges SMS16, 23 and 28, which we have used as reacted melts in our model, have a range of MgO, Al<sub>2</sub>O<sub>3</sub>, Na<sub>2</sub>O, CaO and FeO contents that translates into a similar range of composition for the calculated parent melts (Figure 13). We propose that this reflects a range of possible compositions for the parental melts of both volcanic seafloor and ultramafic seafloor basalts.

Ultramafic seafloor basalt SMS16-3-14 has a depleted REE pattern similar to those of the other basalts in dredge SMS16 (Figure 4 and Table 2), but plots at lower MgO and higher CaO contents (7.56 wt%; Figure 3), in the range of volcanic seafloor basalts. We propose that dredge SMS16, which is located near the limit between volcanic and ultramafic domains, sampled distinct lava flows recovering basalts with contrasted imprints of melt/mantle interactions in the deep axial lithosphere.

Ultramafic seafloor basalts recovered in dredges SMS24, 26 and 31 (Figure 1) have relatively enriched REE and trace element compositions and show negative Eu anomalies (Figure 4). This suggests that these basalts result from significant fractional crystallization. Their MgO, TiO<sub>2</sub>, FeO, Na<sub>2</sub>O and Al<sub>2</sub>O<sub>3</sub> contents would be consistent with relatively high pressure (>4 kbar) fractionation of an ultramafic seafloor basalt type melt (Figure 13).

### 6.2. Melt/Mantle Reactions Versus Fractional Crystallization

In Figure 13, we also show the liquid lines of descent (LLD) calculated with the Petrolog code [Danyushevsky and Plechov, 2011] for fractional crystallization of olivine, plagioclase and clinopyroxene for a range of pressures (2, 4 and 8 kbar). The starting melt composition is that of basalt sample SMS16-3-5. LLDs calculated for the more calcium-rich ultramafic seafloor basalts in dredges SMS23 and 28 (pink and orange triangles in Figure 13) are similar to those calculated for sample SMS16-3-5, except that they predict that clinopyroxene starts crystallizing a bit earlier (e.g., clinopyroxene is in at 13.6% and 19.1% fractional crystallization, respectively, at 8 kbar, against 26.3% with basalt sample SMS16-3-5 as a starting melt).

We see that the melt/mantle reaction trends, calculated with the mass balance approach, are comparable to the early portions of these LLDs. This is understandable because in these early portions of the LLDs, Petrolog predicts fractional crystallization of olivine, then of olivine and plagioclase (Figure 13), while olivine dissolution leading to higher MgO content of the reacted melt dominates the calculated melt/rock reaction trends. The similarity between LLDs and melt/mantle reaction trends is strong over the full range of investigated melt/rock ratios for SiO<sub>2</sub>, CaO and Na<sub>2</sub>O. For Al<sub>2</sub>O<sub>3</sub>, FeO and TiO<sub>2</sub>, the similarity does not persist for the lowest melt/rock ratios because these three elements vary rapidly in LLDs as plagioclase kicks in and as crystallization rates increase (for basalt sample SMS16-3-5 as a starting melt, plagioclase appears on the liquidus at only 1.4% fractional crystallization over the range of investigated crystallization pressures; Figure 13).

Because of the similarity between the early portions of the LLDs and the melt/mantle reaction trends, basalts with intermediate MgO contents in the sample set can be interpreted either as parent melts that have escaped the effects of melt/mantle interactions on their way to the seafloor (or have been involved in such reactions but at melt/rock ratios >100), or as the product of small (<20%; Figure 13) degrees of fractional crystallization from melts that would instead have been similar in composition to the more Mg-rich ultramafic seafloor samples. We propose to use trace element compositions to discriminate between these two interpretations: we interpret basalts with depleted REE patterns similar to those of the ultramafic seafloor basalts in dredges SMS16, SMS23 and SMS28 as parent melts variably modified by melt/mantle reactions, and basalts with enriched REE patterns and negative Eu anomalies, indicative of plagioclase fractionation (Figure 4), as products of fractional crystallization (Figure 13).

### 6.3. Magma Plumbing System at a Melt-Poor and Ultraslow Mid-Ocean Ridge

The melt/mantle reactions documented in this study occur in the deep and hot levels of the axial lithosphere, yet they affect mantle rocks that had already undergone some degree of semiplastic deformation: crystallization of plagioclase and clinopyroxene in the plagioclase-bearing reacted ultramafic and gabbroic rocks postdates a deformation that produced kink bands in relict orthopyroxene porphyroclasts (Figure 7d). In the sketch of Figure 14, we therefore infer that these melt/mantle reactions occurred in the ductile to semibrittle part of the axial lithosphere. We also propose that these melt/rock reactions occurred in the walls of the conduits that allow the aggregated melts extracted from the melting mantle to rise through the axial lithosphere and to the eruption sites. This interpretation is based on the observations of decimeter scale transitions from plagioclase-rich

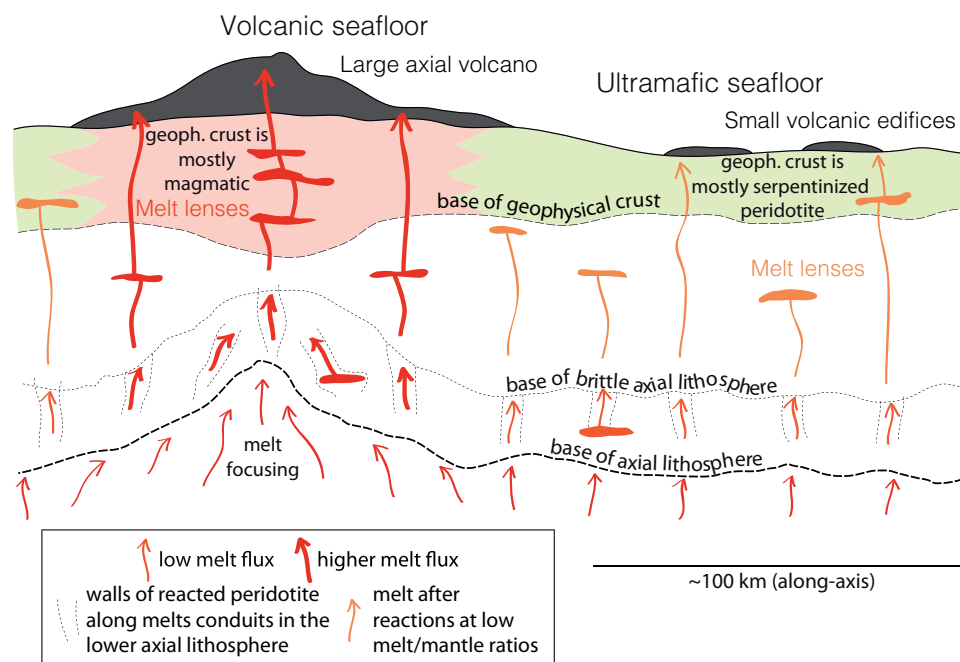


**Figure 14.** Cartoon showing the geological context proposed for melt/mantle interactions and for the melt plumbing system at the easternmost Southwest Indian Ridge. Along-axis section, not to scale. In this conceptual sketch, we propose that melting of a common mantle source occurs to a similar degree below volcanic seafloor and ultramafic seafloor domains. The extracted melts are then focused preferentially toward volcanic domains [Dick, 1989], generating higher melt fluxes and leading to the formation of large axial volcanoes, as proposed by Cannat [2003], and by Standish *et al.* [2008]. The melt/mantle reactions documented in this paper are proposed to occur in the walls of melt conduits, at temperatures lower than the liquidus temperature of the aggregated parent melt and below the base of the brittle axial lithosphere. Microseismic data suggest that this brittle lithosphere is >15 km-thick in the ultramafic seafloor domains [Schlindwein and Schmid, 2016]. Arrows show the flux of melt. Low fluxes in the reactive domain result in low overall melt/rock ratios and in a more modified major element composition (Figure 13) of the reacted melt (orange). Subsequent fractional crystallization occurs in melt lenses emplaced at various levels through the axial lithosphere. A significant proportion of the basalts sampled in volcanic and ultramafic domains, however, do not show evidence for substantial fractionation.

lithologies to unreacted peridotite in many samples. Such conduits are indeed required if the reacted melts are, as we propose, to be erupted at the seafloor. This is in contrast to previous interpretations of similar reacted mantle rocks in other ridge settings as resulting from melt trapping in the deep lithosphere [Godard *et al.*, 2009; Drouin *et al.*, 2009; Renna and Tribuzio, 2011; Sanfilippo *et al.*, 2014].

This melt conduit interpretation also offers a mean to explain the contradiction between the melt/mantle ratios of 20 to 60 calculated to account for the transformation of our inferred parental melts into MgO-enriched and CaO and Al<sub>2</sub>O<sub>3</sub>-depleted ultramafic seafloor basalts, and the observed buffering of clinopyroxene Mg# in the reacted gabbroic rocks. Although this would need to be investigated further, we suggest that in the high temperature conditions that reign in the lower axial lithosphere, melts that rise in these conduits will percolate into the host peridotite over distances of a several centimeters to a few decimeters, then back into the conduit, mixing with unreacted uprising melts. Our mass balance calculations yield values of the integrated or “finite” melt/rock ratio, while mineral compositions in a given reacted rock sample reflect melt/mineral reactions at that particular location in the conduit’s walls, most likely at a lower melt/rock ratio.

In our conceptual model, melt/mantle reactions occur beneath both the volcanic and the ultramafic seafloor domains, but they result in substantial major element compositional changes of the upflowing melt mostly below the ultramafic seafloor domains because the melt/mantle ratio there is always very low. The mass balance calculations suggest that melt/mantle ratios in the 20–60 range are required in order to transform a parental melt with the composition of a typical volcanic seafloor basalt, into an ultramafic seafloor basalt composition (Figure 13). Such low ratios are consistent with the very small volume of erupted basalt in ultramafic seafloor domains. The isolated basaltic construction imaged in Figure 2 is about 2.5 km by 1 km and less than 150m-high (< 0.04 km<sup>3</sup>): with a “finite” melt/rock ratio of 60, it would require the formation

of  $< 0.002 \text{ km}^3$  of reacted mantle in the lower axial lithosphere. Gabbroic rocks represent less than 4% of the samples dredged in ultramafic seafloor domains [Sauter *et al.*, 2013], and most of these gabbroic samples can be interpreted as reacted mantle rocks. Provided that the material exhumed in the upper few hundred meters of the footwall of axial detachment faults is representative of the lithologies present in the lower axial lithosphere, we can use this proportion to estimate the relative volume of reacted conduit walls below the ultramafic seafloor domains. Similarly, if our conceptual model is correct, the observation that most volcanic seafloor basalts are similar in composition to our candidate parental melts (Figure 13), would suggest that they tend to travel in conduits with “finite” melt/rock ratios  $> 100$ .

The conceptual sketch in Figure 14 also includes melt lenses located at various depths in the axial lithosphere (in the mantle or in the crust). These melt lenses have not been imaged seismically yet in the study area. Their existence is, however, likely beneath the large axial volcanoes by analogy with what is known of the melt plumbing system of large volcanoes in other geodynamic contexts [Gudmundsson *et al.*, 1994; Okubo *et al.*, 1997]. The major and trace element composition of both the volcanic and ultramafic seafloor basalts (Figures 3 and 4) indicates variable degrees of fractional crystallization that could take place in such lenses. Most lenses are sketched in the brittle portion of the axial lithosphere. However, mineral compositions of the plagioclase-bearing ultramafic and gabbroic reacted rocks suggest that a few samples of troctolites and olivine gabbros result from reactions with a melt that was slightly enriched in trace elements (Figure 12) and crystallized plagioclase with lower An and higher  $\text{TiO}_2$ ,  $\text{K}_2\text{O}$  contents than in the other sampled ultramafic and gabbroic reacted rocks (Figure 8a). This suggests that limited fractional crystallization of some of the upflowing melt did occur in the deepest levels of the axial lithosphere, prior to or during melt/mantle interactions.

These constraints on the axial magma plumbing system of the ultraslow and melt-depleted study area are based on the joint study of erupted basalts and of the plagioclase-bearing ultramafic and gabbroic reacted rock suite. It is important to stress that the data on basalt composition alone indicates that the melts erupted on the exhumed ultramafic rocks in the nearly amagmatic corridors are in most cases distinct from those erupted in the volcanic domains and that they could not have evolved from the volcanic seafloor melts in dikes feeding lateral eruptions, as proposed for Kilauea or for the MAR [Fialko and Rubin, 1998; Smith and Cann, 1999]. This suggests instead that eruptions in volcanic seafloor domains and in ultramafic seafloor domains are in most cases fed by distinct conduits (Figure 14).

#### 6.4. Reacting Melt Composition and the Anorthite Content of Plagioclase in Plagioclase-Bearing Ultramafic and Gabbroic Samples

The An content of plagioclase in plagioclase-bearing ultramafic rocks, troctolites and gabbros varies over a wide range (58.8 to 91.6%; Figure 9a). The highest An values (74 to 91.6%) are measured in small plagioclase grains that are either isolated in ultramafic rocks with low modal abundances of plagioclase, or found as inclusions in clinopyroxenes. Gabbroic samples that contain such An-rich inclusions, also contain larger plagioclase grains with An contents  $< 74\%$ .

LLDs calculated with Petrolog (Figure 13) [Danyushevsky and Plechov, 2011] predict that the first plagioclase to crystallize from a melt with the major element composition of ultramafic seafloor basalt SMS16-3-5 should have an An content of 62.7% at 2 kbar, 59.3% at 4 kbar, and 52.5% at 8 kbar. Using the composition we calculate for the reacting melt at a melt/rock ratio of 30 (lower MgO and higher CaO and  $\text{Al}_2\text{O}_3$ ; Figure 13) as the initial melt composition, the first plagioclase that fractionates has An values of 63.3% at 2 kbar, 59.9% at 4 kbar, and 53.1% at 8 kbar. These An values are comparable to those measured in the larger plagioclase grains in most of our samples of troctolites and gabbros (An contents between 55 and 67%; Figure 8). This supports our interpretation of these larger plagioclases as having crystallized from the reacting melt.

By contrast, we propose that the higher An and smaller plagioclase grains in the plagioclase-bearing ultramafic rocks are the result reactions between the melt and the peridotite minerals, leading to the destabilization of spinel and to the replacement of preexisting orthopyroxene, olivine and spinel by orthopyroxene, clinopyroxene and plagioclase. Plagioclase grains with similarly high An contents have been reported in several suites of plagioclase-bearing abyssal peridotites [e.g., Tartarotti *et al.*, 2002; Dick *et al.*, 2010; Warren and Shimizu, 2010]. Experimental data on the spinel to plagioclase transition in lherzolites suggest that there is an inverse relation between pressure and the An content of the metamorphic plagioclase [Borghini *et al.*,

2010, 2011]. However, in our study, melt is clearly involved in the formation of the plagioclase and the An contents measured are therefore not equilibrium metamorphic compositions.

### 6.5. Parental Melts

If our interpretation is correct, ultramafic seafloor basalts and most volcanic seafloor basalts are derived from parental melts that have lower MgO contents (7.4 to 8.3%; Figure 13) than commonly proposed for MORB parental melts [e.g., *Kinzler and Grove*, 1993]. Low MgO content in the melts is consistent with the low degrees of mantle melting indicated for the 61°–67°E region of the SWIR by the composition of both peridotites [*Seyler et al.*, 2003; *Brunelli et al.*, 2014] and basalts [*Meyzen et al.*, 2003]. However, current partial melting models using commonly accepted upper mantle source compositions [e.g., *McDonough and Sun*, 1995; *Salter and Stracke*, 2004; *Workman and Hart*, 2005] produce higher melt MgO contents even for the very low degrees of mantle melting inferred in our study area. This is the case for the MELTs model, based on thermodynamics and decompression melting [e.g., *Asimow et al.*, 2001], and for the nonmodal incremental melting model of *Kinzler and Grove* [1992a, 1992b, 1993], which is based on batch melting experiments. For example, using the non modal incremental melting model of *Kinzler and Grove* [1992a, 1992b, 1993], their H&Z dep. 1 depleted upper mantle composition, and a constant melting pressure of 10 kbar, we obtain a MgO content of 9.6 wt% in the melt, for a total melting rate of 4%.

A possible way to obtain parental melts with lower MgO values is to mix these low degree mantle melts with melts produced from basaltic heterogeneities (pyroxenites or eclogites) in the subaxial mantle. The existence of these heterogeneities is supported by basalt petrology and geochemistry [e.g., *Hofmann and White*, 1982; *Hirschmann and Stolper*, 1996; *Sobolev et al.*, 2007]. While this mixing is used to explain some aspects of the trace and isotopic composition of MORBs [e.g., *Lundstrom et al.*, 1995; *Hirschmann and Stolper*, 1996; *Salter and Dick*, 2002; *Pertermann and Hirschmann*, 2003a], it may only have a significant effect on major element compositions if the proportion of pyroxenitic melt over depleted mantle melt is itself significant. This is of course more likely to be the case in the melt-poor ridge environment considered in this study. Such bimodal melting has also been proposed to explain the composition of the so-called low K/Ti basalts in the melt-poor 9° to 25°E SWIR region [*Standish et al.*, 2008]. The pertinence of pyroxenite/peridotite bimodal melting in the study area is further supported by clinopyroxene trace element composition in the dredged spinel peridotites [*Seyler et al.*, 2011]. These trace element compositions can be modeled with open-system melting of the peridotites accompanied by influx of garnet field-generated enriched melts [*Brunelli et al.*, 2014]. Pyroxenites are good candidates for the source of these deep and enriched melts [*Brunelli et al.*, 2015].

To test the potential of this bimodal melting process to produce the low MgO contents measured in primitive volcanic seafloor basalts, we mixed the mantle melts produced with the nonmodal incremental melting model of *Kinzler and Grove* [1992a, 1992b, 1993] for 4% melting, with a melt produced by melting of a pyroxenite component representing 10 wt% of the mantle by 10% (composition A284 obtained experimentally at 2GPa and 1250°C by *Pertermann and Hirschmann* [2003b]). The resulting melt provides a better fit to the range of inferred parental melts (shaded domains in Figure 13) than the low degree mantle melt alone. It fits in terms of MgO (8.2%), CaO (9.8%), Na<sub>2</sub>O (3.9%) and FeO (7.5%) contents. However, it is too high in TiO<sub>2</sub> (2.3%) and SiO<sub>2</sub> (51.5%), and a little too low in Al<sub>2</sub>O<sub>3</sub> (16.7%). While these misfits can be partly explained by our choice of the degree of melting, hence composition, for the pyroxenitic melt component, they could also undoubtedly arise from using melting models that are too simplistic. Indeed, the *Kinzler and Grove* partial melting model is not designed for very low degrees of mantle melting and is based on batch melting experiments while decompression melting in the mantle is more likely to be open system and fractional [*Johnson et al.*, 1990; *Aharonov et al.*, 1995; *Ozawa and Shimizu*, 1995; *Shaw*, 2000]. Also, the bulk mixing approach of the melts derived from the mantle and pyroxenitic components does not take into account the effect of melt/rock disequilibrium in the melting domain [e.g., *Bédard*, 1989; *Aharonov et al.*, 1995; *Ozawa and Shimizu*, 1995; *Shaw*, 2000; *Spiegelman and Kelemen*, 2003; *Liang and Parmentier*, 2010; *Brunelli et al.*, 2014].

A few basalts, so far sampled only in volcanic seafloor domains, have LREE-depleted signatures (Figure 4), higher MgO and FeO contents, and lower Na<sub>2</sub>O, TiO<sub>2</sub> and SiO<sub>2</sub> contents (grey dots in Figure 3). These basalts, occurring in dredges ED20, ED22 and ED26 (Figure 1), could derive from mantle melts with very little to no mixed pyroxenitic component.

### 6.6. Are the Effects of Melt/Mantle Reactions Seen in MORBs From More Magmatically Robust Slow-Spreading Ridges?

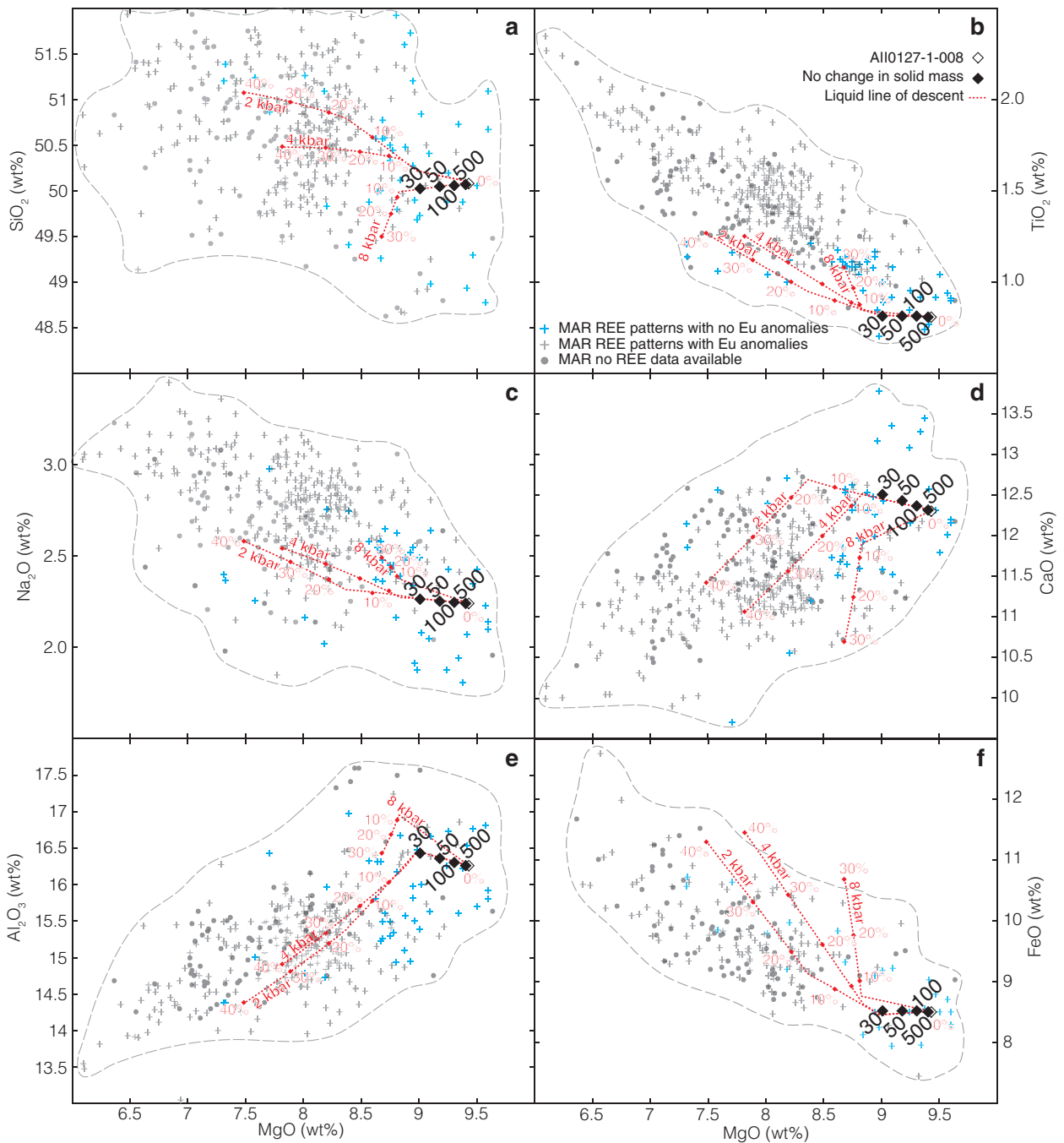
The easternmost SWIR study area is a low melt supply end-member for the global MOR system and the nearly amagmatic spreading corridors there are indeed exceptional settings. The more common case is for slow and ultraslow spreading ridges to receive sufficient melt, averaged over the 30 to 100 km length of a ridge segment, to produce a 6 km-thick magmatic crust (see review in *Carbotte et al.* [2015]). In this more common slow spreading ridge setting, mantle exhumation and detachment faulting characterize the least magmatically active domains [*Cannat et al.*, 1995; *Dick et al.*, 2008; *Escartin et al.*, 2008]. Microseismicity studies in these detachment-dominated contexts indicate that the brittle part of the axial lithosphere is about 8 km-thick [*Toomey et al.*, 1988; *Wolfe et al.*, 1995; *deMartin et al.*, 2007]. This is less than inferred for the eastern SWIR (Figure 14), but mantle melts still have to travel through a substantial thickness of lithospheric mantle before they can crystallize in the crust or be erupted as basalts [*Cannat et al.*, 1995]. Gabbroic impregnations and veins, and reacted ultramafic rocks have been sampled at numerous MAR locations and bear witness to melt/mantle reactions that are comparable to those described in this paper [*Cannat*, 1993; *Cannat and Casey*, 1995; *Cannat et al.*, 1995, 1997b; *Seyler et al.*, 2007; *Dick et al.*, 2008; *Suhr et al.*, 2008; *Drouin et al.*, 2009].

Figure 15 shows results of the same mass balance model as in Figure 13, using a MgO and CaO-rich MAR basalt as the reacted melt, a moderately depleted spinel lherzolite from south of the Kane Fracture Zone for the reacting mantle, and an olivine-rich troctolite drilled during leg IODP304/305 for the reacted rock. As calculated for the SWIR case (Figure 13), the initial composition predicted for the reacting melt, for no change in the solid mass, is lower in MgO, and higher in CaO and  $\text{Al}_2\text{O}_3$ , compared to the reacted melt composition and the trace element and  $\text{TiO}_2$  contents of the melt are not modified, regardless of the melt/rock ratio (Figure 15).

If they occur at sufficiently low “finite” melt/rock ratios in conduits that channel melts through the deep lithosphere, melt/mantle reactions could thus be expected to increase the MgO and to lower the CaO and  $\text{Al}_2\text{O}_3$  contents of MAR asthenospheric parent melts in much the same way as proposed for the ultramafic seafloor basalts at the easternmost SWIR. If this were the case, some of the highest MgO content MAR basalts (Figure 15) would not in fact be closer to parental melt composition than less MgO-rich basalts collected in the same regions.

In our conceptual model, we propose that the “finite” melt/rock ratio (the ratio of the mass of reacted melt to the initial mass of reacting mantle) is related to the flux of melt in conduits that cross the deepest and hottest portions of the axial lithosphere. This “finite” melt/rock ratio is likely to be lowest at ridges that receive very little melt, such as the nearly amagmatic corridors of the eastern SWIR. However, for ridges that receive more melt, these “finite” melt/rock ratios may not depend only on the overall ridge melt supply: for a given melt supply, “finite” melt/rock ratios would be lower if the melt is partitioned into numerous conduits. Investigating the possible effects of melt/mantle interactions in the deep axial lithosphere on basalt chemistry may thus be a way to better understand the dynamics of magma at mid-ocean ridge. However, in the higher melt supply context of the MAR, melts are also more likely to gather in melt bodies and pockets where they undergo significant fractionation and melt/rock interactions. These later processes would overprint the earlier chemical effects of melt/mantle interactions.

Figure 15 shows the PetDB compilation of MAR basalts and identifies those that have non Eu-depleted REE patterns and have therefore crystallized only minor amounts of plagioclase prior to being erupted. Most of these least fractionated basalts have  $8.5\% < \text{MgO} < 9.5\%$ , with a spread in MgO, CaO and  $\text{Al}_2\text{O}_3$  that could be interpreted in four ways: as a result of regional variations in the degree of mantle melting; as due to variations in the degree of early olivine and plagioclase fractionation; as due to variations in the contribution of melt/rock reactions in the crust [e.g., *Bédard*, 1991, 1993; *Lissenberg and Dick*, 2008]; or as due to variations in the contribution of melt/mantle reactions in the axial lithospheric mantle. Refining the interpretation requires the study of more local data sets, allowing for intersegment and intra-segment variations to be identified. Numerous studies have performed this more local approach of MAR basalts and identified intra-segment calcium and calcium/aluminum versus magnesium trends [*Tormey et al.*, 1987; *Grove et al.*, 1992; *Michael and Cornell*, 1998; *Escartin et al.*, 2008]. These local trends have been proposed to characterize detachment-dominated ridge segments [*Escartin et al.*, 2008]. They are best interpreted as due to significant preeruption crystallization of clinopyroxene, and two interpretations have been proposed for this: a deeper onset of fractional



**Figure 15.** Mass balance model of the possible effect of melt/rock interactions in the mantle lithosphere on the major element composition of basalts in the Mid-Atlantic Ridge. In this model, we use the modal abundances and major element composition of the mineral phases in the inferred products of melt/mantle interaction (troctolite sample IODP304/305-U1309D-63R2-28-30 [Drouin *et al.*, 2009]; and MAR basalt sample AII0127-1-008 [Gale *et al.*, 2013]), and in the inferred solid prior to reaction (plagioclase-free residual lherzolite: sample SDM-D2-2-2 [Ghose *et al.*, 1996]), to reconstruct the initial composition of the reacting melt (black diamonds: no change in solid mass) for a range of melt/mantle ratios (see text). (a) SiO<sub>2</sub>, (b) TiO<sub>2</sub>, (c) Na<sub>2</sub>O, (d) CaO, (e) Al<sub>2</sub>O<sub>3</sub> and (f) FeO contents in function of MgO content. Dotted lines correspond to the liquid lines of descent calculated for crystallization pressures of 2, 4 and 8 kbar with the Petrolog code ([Danyushevsky and Plechov, 2011]; parameters used for these calculations are similar to those used for Figure 13 and detailed in the supporting information Text S4) for a starting composition similar to basalt sample AII0127-1-008. The model trends are shown over a compilation of MAR basalts (in grey) collected between 60°N and 55°S (PetDB [Lehnert *et al.*, 2000]; details in supporting information Text S2). Grey crosses correspond to samples with pronounced Eu anomaly. Blue crosses correspond to samples with no Eu anomaly. Light grey dots correspond to samples for which trace element data are not available.

crystallization [e.g., Michael and Cornell, 1998; Herzberg, 2004], or extensive interactions between MORB-type melts and olivine gabbros in the lower, mushy magmatic crust, at moderate pressure [e.g., Bédard, 1991, 1993; Lissenberg and Dick, 2008]. Melts undergoing such reactions can be enriched in Al<sub>2</sub>O<sub>3</sub> and MgO and depleted

in CaO and SiO<sub>2</sub> [Lissenberg and Dick, 2008], thus producing changes in CaO and MgO that go in the same direction as the melt/mantle reactions described in this paper. It is worth noting here that our candidate parental melts for the eastern SWIR basalts have substantially lower MgO and CaO, preventing the early fractional crystallization of clinopyroxene, even at relatively high pressure (Figure 13).

Whatever their cause (deep fractional crystallization or more shallow melt-gabbro reactions), these early clinopyroxene crystallization local trends obscure the effect melt/mantle reactions of the type documented in this paper could have had on the Mg, Ca and Al content of primitive MAR MORBs. Although this would deserve further examination, we therefore conclude that while such melt/mantle reactions are known to occur at the MAR [Godard *et al.*, 2009; Drouin *et al.*, 2009; Renna and Tribuzio, 2011; Sanfilippo *et al.*, 2014], their effect does not appear prominent on primitive MAR basalt compositions.

## 7. Conclusions

The eastern SWIR between 61° and 67°E has a very low melt supply and comprises several corridors of nearly amagmatic spreading that expose mantle-derived serpentinized peridotite [Cannat *et al.*, 2003, 2006; Sauter *et al.*, 2013]. More volcanically active ridge portions separate these corridors. Basalts from this melt-poor ridge represent a global MORB end-member for major element compositions [Meyzen *et al.*, 2003], with higher Na<sub>2</sub>O and Al<sub>2</sub>O<sub>3</sub> contents, and lower CaO and FeO contents at a given MgO. Within this end-member group, basalts from the nearly amagmatic corridors have significantly lower CaO and Al<sub>2</sub>O<sub>3</sub> contents at a given MgO than basalts from the volcanic areas. They are, however, similar in terms of trace elements and isotopic ratios.

Serpentinized mantle-derived peridotites represent 96% in volume of the material dredged in the nearly amagmatic corridors [Sauter *et al.*, 2013]. In addition to rare basalts, these dredges have also recovered small amounts of plagioclase-bearing ultramafic rocks, and of olivine gabbros. These rocks present textural and chemical characteristics that are best interpreted as due to reactions between a peridotite or websterite host rock and basaltic melts in the deep axial lithosphere. These reactions involve dissolution of olivine and orthopyroxene, and crystallization of clinopyroxene and plagioclase. The trace element composition of clinopyroxene indicates that the reacting melt had the same trace element signature as the basalts erupted at the ridge. Because we observe the transition between the ultramafic host and the most plagioclase-rich lithologies at the scale of decimeter-sized sample, we infer that these reactions occurred in the walls of veins or narrow dikes that formed conduits for primitive MORB melts, allowing them to rise through the axial lithosphere and to the eruption sites.

In order to assess the possible effect of these reactions on the composition of the reacted melt, we develop a simple mass balance model in which we use the modal abundances and the major and trace element composition of the mineral phases in the inferred products of melt/mantle interaction (the plagioclase-bearing ultramafic to gabbroic rocks and the basalt erupted in nearly amagmatic corridors), and in the inferred solid prior to reaction (plagioclase-free residual lherzolites), to reconstruct the initial composition of the reacting melt. We find that for low ( $\leq 50$ ) values of the ratio of erupted melt to reacted mantle, the initial composition of the reacting melt is significantly lower in Mg, and higher in Ca and Al, resembling the composition of the basalts dredged in the volcanic portions of the study area. This, and their similarity in terms of trace element composition and isotopic ratio leads us to propose that the two groups of basalts derive from similar parental melts, with low MgO contents (7.5 – 8.25 wt%). We propose that the basalts erupted on ultramafic seafloor are more affected by reactions between these parent melts and the mantle rocks in the deep lithosphere below the ridge because the ratio of erupted melt to reacted mantle is very low in the nearly amagmatic corridors. We also propose that the range of major element compositions inferred for the asthenospheric parental melts involved in these reactions could result from very low degrees of melting (4%) of a mantle that also contains about 10% of a more fusible pyroxenite component.

Although this would deserve further study, we predict that melt/mantle reactions that have been documented at detachment-dominated portions of the more magmatically active MAR [Godard *et al.*, 2009; Drouin *et al.*, 2009; Renna and Tribuzio, 2011; Sanfilippo *et al.*, 2014] should have a lesser effect on the composition of the basalts erupted there.

### Acknowledgments

The authors thank Jean H. Bédard, John Lassiter, an anonymous reviewer and the Editor Janne Blichert-Toft for their constructive reviews that helped to improve this manuscript. We also thank Jean H. Bédard for providing us his partition coefficients data set. The authors thank Daniel Sauter, cochief of the SMOOTHSEAFLOOR cruise. This work was supported by the Institut National des Sciences de l'Univers (SYSTER program). This is IPGP contribution 3770. Supporting data are included as tables in the supporting information. Upon publication of this paper, the data will be contributed to the Petrological Database ([www.earthchem.org/petdb](http://www.earthchem.org/petdb)) and to SEANOE (<http://doi.org/10.17882/46520>).

### References

- Aharonov, E., J. A. Whitehead, P. B. Kelemen, and M. Spiegelman (1995), Channeling instability of upwelling melt in the mantle, *J. Geophys. Res.*, *100*(B10), 20,433–20,450.
- Asimow, P. D., M. M. Hirschmann, and E. M. Stolper (2001), Calculation of peridotite partial melting from thermodynamic models of minerals and melts, IV. Adiabatic decompression and the composition and mean properties of mid-ocean ridge basalts, *J. Petrol.*, *42*(5), 963–998.
- Bédard, J. H. (1989), Disequilibrium mantle melting, *Earth Planet. Sci. Lett.*, *91*(3), 359–366.
- Bédard, J. H. (1991), Cumulate recycling and crustal evolution in the Bay of Islands ophiolite, *J. Geol.*, *99*(2), 225–249.
- Bédard, J. H. (1993), Oceanic crust as a reactive filter: Synkinematic intrusion, hybridization, and assimilation in an ophiolitic magma chamber, western Newfoundland, *Geology*, *21*(1), 77–80.
- Bédard, J. H. (1994), A procedure for calculating the equilibrium distribution of trace elements among the minerals of cumulate rocks, and the concentration of trace elements in the coexisting liquids, *Chem. Geol.*, *118*(1), 143–153.
- Bédard, J. H. (2006), Trace element partitioning in plagioclase feldspar, *Geochim. Cosmochim. Acta*, *70*(14), 3717–3742.
- Bédard, J. H. (2014), Parameterizations of calcic clinopyroxene-Melt trace element partition coefficients, *Geochem. Geophys. Geosyst.*, *15*, 303–336, doi:10.1002/2013GC005112.
- Bloomer, S. H., P. S. Meyer, H. J. B. Dick, K. Ozawa, and J. H. Natland (1991), Textural and mineralogical variations in gabbroic rocks from Hole 735B, in *Proceedings of Ocean Drilling Program, Scientific Results*, vol. 118, edited by R. P. Von Herzen et al., pp. 21–39.
- Borghini, G., and E. Rampone (2007), Postcumulus processes in oceanic-type olivine-rich cumulates: The role of trapped melt crystallization versus melt/rock interaction, *Contrib. Mineral. Petrol.*, *154*(6), 619–633.
- Borghini, G., E. Rampone, L. Crispini, R. De Ferrari, and M. Godard (2007), Origin and emplacement of ultramafic–mafic intrusions in the Ero-Tobbio mantle peridotite (Ligurian Alps, Italy), *Lithos*, *94*(1), 210–229.
- Borghini, G., P. Fumagalli, and E. Rampone (2010), The stability of plagioclase in the upper mantle: Subsolvus experiments on fertile and depleted lherzolite, *J. Petrol.*, *51*(1–2), 229–254.
- Borghini, G., Fumagalli, P., and E. Rampone (2011), The geobarometric significance of plagioclase in mantle peridotites: A link between nature and experiments, *Lithos*, *126*(1), 42–53.
- Bottinga, Y., and C. J. Allègre (1973), Thermal aspects of sea-floor spreading and the nature of the oceanic crust, *Tectonophysics*, *18*(1), 1–17.
- Brunelli, D., E. Paganelli, and M. Seyler (2014), Percolation of enriched melts during incremental open-system melting in the spinel field: A REE approach to abyssal peridotites from the Southwest Indian Ridge, *Geochim. Cosmochim. Acta*, *127*, 190–203.
- Brunelli, D., M. Cannat, M. Paquet, M. Sforna, and M. Seyler (2015), Sodium inverse relationships during melting in ultraslow spreading regions: Insights from SWIR-smoothseafloor peridotites, Abstract V11B-3063 presented at 2015 Fall Meeting, AGU, San Francisco, Calif.
- Cannat, M. (1993), Emplacement of mantle rocks in the seafloor at mid-ocean ridges, *J. Geophys. Res.*, *98*(B3), 4163–4172.
- Cannat, M., C. Rommevaux-Jestin, and H. Fujimoto (2003), Melt supply variations to a magma-poor ultra-slow spreading ridge (Southwest Indian Ridge 61° to 69°E), *Geochem. Geophys. Geosyst.*, *4*(8), doi:10.1029/2002GC000480.
- Cannat, M., and J. F. Casey (1995), An ultramafic lift at the Mid-Atlantic Ridge: Successive stages of magmatism in serpentinized peridotites from the 15 N region, in *Mantle and Lower Crust Exposed in Oceanic Ridges and in Ophiolites*, edited by R. L. M. Vissers, and A. Nicolas, pp. 5–34, Springer, Netherlands.
- Cannat, M., D. Bideau, and R. Hébert (1990), Plastic deformation and magmatic impregnation in serpentinized ultramafic rocks from the Garrett transform fault (East Pacific Rise), *Earth Planet. Sci. Lett.*, *101*(2), 216–232.
- Cannat, M., et al. (1995), Thin crust, ultramafic exposures, and rugged faulting patterns at the Mid-Atlantic Ridge (22–24 N), *Geology*, *23*(1), 49–52.
- Cannat, M., G. Ceuleneer, and J. Fletcher (1997a), 5. Localization of ductile strain and the magmatic evolution of gabbroic rocks drilled at the Mid-Atlantic Ridge (23°N), *Proc. Ocean Drill. Program Sci. Results*, *153*, 77–98.
- Cannat, M., F. Chatin, H. Whitechurch, and G. Ceuleneer (1997b), 11. Gabbroic rocks trapped in the upper mantle at the Mid-Atlantic Ridge, *Proc. Ocean Drill. Program Sci. Results*, *153*, 243–264.
- Cannat, M., C. Rommevaux-Jestin, D. Sauter, C. Deplus, and V. Mendel (1999), Formation of the axial relief at the very slow spreading Southwest Indian Ridge (49° to 69°E), *J. Geophys. Res.*, *104*(B10), 22,825–22,843.
- Cannat, M., D. Sauter, V. Mendel, E. Ruellan, K. Okino, J. Escartin, V. Combier, and M. Baala (2006), Modes of seafloor generation at a melt-poor ultraslow-spreading ridge, *Geology*, *34*(7), 605–608, doi:10.1130/G22486.1.
- Cannat, M., D. Sauter, A. Bezos, C. Meyzen, E. Humler, and M. Le Rigoleur (2008), Spreading rate, spreading obliquity, and melt supply at the ultraslow spreading Southwest Indian Ridge, *Geochem. Geophys. Geosyst.*, *9*, Q04002, doi:10.1029/2007GC001676.
- Carbotte, S. M., D. K. Smith, M. Cannat, and E. M. Klein (2015), Tectonic and magmatic segmentation of the Global Ocean Ridge System: A synthesis of observations, *Geol. Soc. Spec. Publ.*, *420*, SP420–5.
- Carmichael, I. S., F. J. Turner, and J. Verhoogen (1974), *Igneous Petrology*, McGraw-Hill.
- Catanzaro, E. J., T. J. Murphy, W. R. Shields, and E. L. Garner (1968), Absolute isotopic abundance ratios of common, equal-atom, and radiogenic lead isotopic standards, *J. Res. Natl. Bur. Stand.*, *72A* (3), 261–267.
- Danyushevsky, L. V., and P. Plechov (2011), Petrolog3: Integrated software for modeling crystallization processes, *Geochem. Geophys. Geosyst.*, *12*, Q07021, doi:10.1029/2011GC003516.
- deMartin, B. J., R. A. Sohn, J. P. Canales, and S. Humphris (2007), Kinematics and geometry of active detachment faulting beneath the Trans-Atlantic Geotraverse (TAG) hydrothermal field on the Mid-Atlantic Ridge, *Geology*, *35*, 711–714.
- Dick, H. J. B. (1977), Evidence of partial melting in the Josephine Peridotite, in *Magma Genesis*, edited by H. J. B. Dick, pp. 59–62, Oreg. Dep. of Geol. and Miner. Ind., Portland.
- Dick, H. J. B. (1989), Abyssal peridotites, very slow spreading ridges and ocean ridge magmatism, *Geol. Soc., London, Special Publications*, *42*(1), 71–105.
- Dick, H. J. B., R. Fisher, and W. Bryan (1984), Mineralogical variability of the uppermost mantle along mid-ocean ridges, *Earth Planet. Sci. Lett.*, *69*(1), 88–106.
- Dick, H. J. B., C. J. Lissenberg, and J. M. Warren (2010), Mantle melting, melt transport, and delivery beneath a slow-spreading ridge: The Paleo-MAR from 23°15'N to 23°45'N, *J. Petrol.*, *51*(1–2), 425–467, doi:10.1093/petrology/egg088.
- Dick, H. J., M. A. Tivey, and B. E. Tucholke (2008), Plutonic foundation of a slow-spreading ridge segment: Oceanic core complex at Kane Megamullion, 23°30' N, 45°20' W, *Geochem. Geophys. Geosyst.*, *9*, Q05014, doi:10.1029/2007GC001645.

- Dick, H. J. B., et al. (2002), Primary silicate mineral chemistry of a 1.5-km section of very slow spreading lower ocean crust: ODP Hole 735B, Southwest Indian Ridge, in *Proc. ODP, Sci. Results*, vol. 176, edited by J. H. Natland, pp. 1–61. [Available at [http://www-odp.tamu.edu/publications/176\\_SR/VOLUME/CHAPTERS/SR176\\_10.PDF](http://www-odp.tamu.edu/publications/176_SR/VOLUME/CHAPTERS/SR176_10.PDF).]
- Drouin, M., M. Godard, B. Ildefonse, O. Bruguier, and C. J. Garrido (2009), Geochemical and petrographic evidence for magmatic impregnation in the oceanic lithosphere at Atlantis Massif, Mid-Atlantic Ridge (IODP Hole U1309D, 30 N), *Chem. Geol.*, *264*(1), 71–88.
- Escartin, J., D. K. Smith, J. Cann, H. Schouten, C. H. Langmuir, and S. Escrig (2008), Central role of detachment faults in accretion of slow-spreading oceanic lithosphere, *Nature*, *455*(7214), 790–794.
- Fialko, Y. A., and A. M. Rubin (1998), Thermodynamics of lateral dike propagation: Implications for crustal accretion at slow spreading mid-ocean ridges, *J. Geophys. Res.*, *103*(B2), 2501–2514.
- Gale, A., M. Laubier, S. Escrig, and C. H. Langmuir (2013), Constraints on melting processes and plume-ridge interaction from comprehensive study of the FAMOUS and North Famous segments, Mid-Atlantic Ridge, *Earth Planet. Sci. Lett.*, *365*, 209–220.
- Gale, A., C. H. Langmuir, and C. A. Dalton (2014), The global systematics of ocean ridge basalts and their origin, *J. Petrol.*, *55*(6), 1051–1082.
- Ghose, I., M. Cannat, and M. Seyler (1996), Transform fault effect on mantle melting in the MARK area (Mid-Atlantic Ridge south of the Kane transform), *Geology*, *24*(12), 1139–1142.
- Godard, M., et al. (2009), Geochemistry of a long in-situ section of intrusive slow-spread oceanic lithosphere: Results from IODP Site U1309 (Atlantis Massif, 30°N Mid-Atlantic-Ridge), *Earth Planet. Sci. Lett.*, *279*(1), 110–122.
- Grove, T. L., R. J. Kinzler, and W. B. Bryan (1992), Fractionation of mid-ocean ridge basalt (MORB), in *Mantle Flow and Melt Generation at Mid-Ocean Ridges*, *Geophys. Monogr. Ser.*, vol. 71, edited by J. P. Morgan, D. K. Blackman, and J. M. Sinton, pp. 281–310, AGU, Washington, D. C.
- Gudmundsson, O., B. Brandsdottir, W. Menke, and G. E. Sigvaldason (1994), The crustal magma chamber of the Katla volcano in south Iceland revealed by 2-D seismic undershooting, *Geophys. J. Int.*, *119*(1), 277–296.
- Günther, D., and C. A. Heinrich (1999), Enhanced sensitivity in laser ablation-ICP mass spectrometry using helium-argon mixtures as aerosol carrier, *J. Anal. At. Spectrom.*, *14*(9), 1363–1368.
- Hamelin, C., A. Bezos, L. Dosso, J. Escartin, M. Cannat, and C. Mevel (2013), Atypically depleted upper mantle component revealed by Hf isotopes at Lucky Strike segment, *Chem. Geol.*, *341*, 128–139.
- Herzberg, C. (2004), Partial crystallization of mid-ocean ridge basalts in the crust and mantle, *J. Petrol.*, *45*(12), 2389–2405, doi:10.1093/petrology/egh040.
- Hirschmann, M. M., and E. M. Stolper (1996), A possible role for garnet pyroxenite in the origin of the “garnet signature” in MORB, *Contrib. Mineral. Petrol.*, *124*(2), 185–208.
- Hirschmann, M. M., M. S. Ghiorso, L. E. Waslylenki, P. D. Asimow, and E. M. Stolper (1998), Calculation of peridotite partial melting from thermodynamic models of minerals and melts. I. Review of methods and comparison with experiments, *J. Petrol.*, *39*(6), 1091–1115.
- Hofmann, A. W., and W. M. White (1982), Mantle plumes from ancient oceanic crust, *Earth Planet. Sci. Lett.*, *57*(2), 421–436.
- Hopson, C. A., R. G. Coleman, R. T. Gregory, J. S. Pallister, and E. H. Bailey (1981), Geologic section through the Samail Ophiolite and associated rocks along a Muscat-Ibra Transect, southeastern Oman Mountains, *J. Geophys. Res.*, *86*(B4), 2527–2544.
- Jaques, A. L., and D. H. Green (1980), Anhydrous melting of peridotite at 0–15 kb pressure and the genesis of tholeiitic basalts, *Contrib. Mineral. Petrol.*, *73*(3), 287–310.
- Johnson, K., H. J. Dick, and N. Shimizu (1990), Melting in the oceanic upper mantle: An ion microprobe study of diopsides in abyssal peridotites, *J. Geophys. Res.*, *95*(B3), 2661–2678.
- Kelemen, P. B. (1990), Reaction between ultramafic rock and fractionating basaltic magma I. Phase relations, the origin of calc-alkaline magma series, and the formation of discordant dunite, *J. Petrol.*, *31*(1), 51–98.
- Kelemen, P. B., D. B. Joyce, J. D. Webster, and J. R. Holloway (1990), Reaction between ultramafic rock and fractionating basaltic magma II. Experimental investigation of reaction between olivine tholeiite and harzburgite at 1150–1050 C and 5 kb, *J. Petrol.*, *31*(1), 99–134.
- Kelemen, P. B., N. Shimizu, and V. J. Salters (1995), Extraction of mid-ocean-ridge basalt from the upwelling mantle by focused flow of melt in dunite channels, *Nature*, *375*(6534), 747–753.
- Kelemen, P. B., G. Hirth, N. Shimizu, M. Spiegelman, and H. J. Dick (1997), A review of melt migration processes in the adiabatically upwelling mantle beneath oceanic spreading ridges, *Philos. Trans. R. Soc. London A*, *355*(1723), 283–318.
- Kinzler, R., and T. Grove (1992b), Primary magmas of mid-ocean ridge basalts 2. Applications, *J. Geophys. Res.*, *97*(B5), 6907–6926.
- Kinzler, R. J., and T. L. Grove (1992a), Primary magmas of mid-ocean ridge basalts 1. Experiments and methods, *J. Geophys. Res.*, *97*(B5), 6885–6906.
- Kinzler, R. J., and T. L. Grove (1993), Corrections and further discussion of the primary magmas of mid-ocean ridge basalts, 1 and 2, *J. Geophys. Res.*, *98*(B12), 22,339–22,347.
- Klein, E. M., and C. H. Langmuir (1987), Global correlations of ocean ridge basalt chemistry with axial depth and crustal thickness, *J. Geophys. Res.*, *92*(B8), 8089–8115.
- Langmuir, C. H., E. M. Klein, and T. Plank (1992), Petrological systematics of mid-ocean ridge basalts: Constraints on melt generation beneath ocean ridges, in *Mantle Flow and Melt Generation at Mid-Ocean Ridges*, *Geophys. Monogr. Ser.*, vol. 71, edited by J. P. Morgan, D. K. Blackman, J. M. Sinton, pp. 180–280, AGU, Washington, D. C.
- Lee, C. T. A., A. Harbert, and W. P. Leeman (2007), Extension of lattice strain theory to mineral/mineral rare-earth element partitioning: An approach for assessing disequilibrium and developing internally consistent partition coefficients between olivine, orthopyroxene, clinopyroxene and basaltic melt, *Geochim. Cosmochim. Acta*, *71*(2), 481–496.
- Lehnert, K., Y. Su, C. H. Langmuir, B. Sarbas, and U. Nohl (2000), A global geochemical database structure for rocks, *Geochem. Geophys. Geosyst.*, *1*(5), 1012, doi:10.1029/1999GC000026.
- Liang, Y., and E. M. Parmentier (2010), A two-porosity double lithology model for partial melting, melt transport and melt–rock reaction in the mantle: Mass conservation equations and trace element transport, *J. Petrol.*, *51*(1–2), 125–152, doi:10.1093/petrology/egp086.
- Lissenberg, C. J., and H. J. Dick (2008), Melt–rock reaction in the lower oceanic crust and its implications for the genesis of mid-ocean ridge basalt, *Earth Planet. Sci. Lett.*, *271*(1), 311–325.
- Lundstrom, C. C., J. Gill, Q. Williams, and M. R. Perfit (1995), Mantle melting and basalt extraction by equilibrium porous flow, *Science*, *270*(5244), 1958.
- Manhes, G., J. F. Minster, and C. J. Allegre (1978), Comparative uranium-thorium-lead and rubidium-strontium study of the Saint Severin amphoterite: Consequences for early solar system chronology, *Earth Planet. Sci. Lett.*, *39*(1), 14–24.
- McDonough, W. F., and S. S. Sun (1995), The composition of the Earth, *Chem. Geol.*, *120*(3), 223–253.
- Mével, C., et al. (1997), Sampling the Southwest Indian Ridge: First results of the EDUL cruise (R/V Marion Duffresne II, August 1997), *Inter-Ridge News*, *6*(2), 25–26.

- Meyzen, C. M., M. J. Toplis, E. Humler, J. N. Ludden, and C. Mével (2003), A discontinuity in mantle composition beneath the southwest Indian ridge, *Nature*, *421*(6924), 731–733.
- Meyzen, C. M., J. N. Ludden, E. Humler, B. Luais, M. J. Toplis, C. Mével, and M. Storey (2005), New insights into the origin and distribution of the DUPAL isotope anomaly in the Indian Ocean mantle from MORB of the Southwest Indian Ridge, *Geochem. Geophys. Geosyst.*, *6*, Q11K11, doi:10.1029/2005GC000979.
- Michael, P. J., and W. C. Cornell (1998), Influence of spreading rate and magma supply on crystallization and assimilation beneath mid-ocean ridges: Evidence from chlorine and major element chemistry of mid-ocean ridge basalts, *J. Geophys. Res.*, *103*(B8), 18,325–18,356.
- Miller, D. J., et al. (2009), Data report: microprobe analyses of primary mineral phases from Site U1309, Atlantis Massif, IODP Expedition 304/305, in edited by D. K. Blackman, et al., and the Expedition 304/305 Scientists, Proc. IODP (Integrated Ocean Drilling Program Management International, Inc.), 304/305, College Station, Tex., doi:10.2204/iodp.proc.304305.202.2009.
- Morishita, T., Y. Ishida, S. Arai, and M. Shirasaka (2005), Determination of multiple trace element compositions in thin (> 30  $\mu\text{m}$ ) layers of NIST SRM 614 and 616 using Laser Ablation-Inductively Coupled Plasma-Mass Spectrometry (LA-ICP-MS), *Geostand. Geoanal. Res.*, *29*(1), 107–122.
- Muller, M. R., T. A. Minshull, and R. S. White (1999), Segmentation and melt supply at the Southwest Indian Ridge, *Geology*, *27*(10), 867–870.
- Okubo, P. G., H. M. Benz, and B. A. Chouet (1997), Imaging the crustal magma sources beneath Mauna Loa and Kilauea volcanoes, Hawaii, *Geology*, *25*(10), 867–870.
- Ozawa, K., and N. Shimizu (1995), Open-system melting in the upper mantle: Constraints from the Hayachine-Miyamori ophiolite, northeastern Japan, *J. Geophys. Res.*, *100*(B11), 22,315–22,335.
- Ozawa, K., P. S. Meyer, and S. H. Bloomer (1991), Mineralogy and textures of iron-titanium oxide gabbros and associated olivine gabbros from Hole 735B, in *Proceedings of Ocean Drilling Program, Scientific Results*, vol. 118, edited by R. P. Von Herzen et al., pp. 41–73.
- Paquet, M., M. Cannat, C. Hamelin, and D. Brunelli (2014), The easternmost Southwest Indian Ridge: A laboratory to study MORB and oceanic gabbro petrogenesis in a very low melt supply context, Abstract V31B-4754 presented at 2010 Fall Meeting, AGU, San Francisco, Calif.
- Patriat, P., and J. Segoufin (1988), Reconstruction of the central Indian Ocean, *Tectonophysics*, *155*(1), 211–234.
- Pearce, N. J., W. T. Perkins, J. A. Westgate, M. P. Gorton, S. E. Jackson, C. R. Neal, and S. P. Chenerly (1997), A compilation of new and published major and trace element data for NIST SRM 610 and NIST SRM 612 glass reference materials, *Geostand. Newsl.*, *21*(1), 115–144.
- Pertermann, M., and M. M. Hirschmann (2003a), Partial melting experiments on a MORB-like pyroxenite between 2 and 3 GPa: Constraints on the presence of pyroxenite in basalt source regions from solidus location and melting rate, *J. Geophys. Res.*, *108*(B2), 2125, doi:10.1029/2000JB000118.
- Pertermann, M., and M. M. Hirschmann (2003b), Anhydrous partial melting experiments on MORB-like eclogite: Phase relations, phase compositions and mineral–melt partitioning of major elements at 2–3 GPa, *J. Petrol.*, *44*(12), 2173–2201.
- Quick, J. E. (1982), The origin and significance of large, tabular dunite bodies in the Trinity peridotite, northern California, *Contrib. Mineral. Petrol.*, *78*(4), 413–422.
- Rampone, E., P. Bottazzi, and L. Ottolini (1991), Complementary Ti and Zr anomalies in orthopyroxene and clinopyroxene from mantle peridotites, *Nature*, *354*, 518–520, doi:10.1038/354518a0
- Renna, M. R., and R. Tribuzio (2011), Olivine-rich troctolites from Ligurian ophiolites (Italy): Evidence for impregnation of replacive mantle conduits by MORB-type melts, *J. Petrol.*, *52*(9), 1763–1790.
- Ross, K., and D. Elthon (1997), Cumulus and postcumulus crystallization in the oceanic crust: Major- and trace-element geochemistry of Leg 153 gabbroic rocks, in *Proceedings of Ocean Drilling Program, Scientific Results*, vol. 153, edited by J. A. Karson, et al., pp. 333–350, Ocean Drill. Program, Natl. Sci. Found., College Station, Tex.
- Rubin, K. H., and J. M. Sinton (2007), Inferences on mid-ocean ridge thermal and magmatic structure from MORB compositions, *Earth Planet. Sci. Lett.*, *260*(1), 257–276.
- Salters, V. J., and H. J. Dick (2002), Mineralogy of the mid-ocean-ridge basalt source from neodymium isotopic composition of abyssal peridotites, *Nature*, *418*(6893), 68–72.
- Salters, V. J., and A. Stracke (2004), Composition of the depleted mantle, *Geochem. Geophys. Geosyst.*, *5*, Q05B07, doi:10.1029/2003GC000597.
- Sanfilippo, A., and R. Tribuzio, R. (2013), Origin of olivine-rich troctolites from the oceanic lithosphere: A comparison between the alpine Jurassic ophiolites and modern slow spreading ridges, *Ophiolite*, *38*(1), 89–99.
- Sanfilippo, A., H. J. Dick, and Y. Ohara (2013), Melt–rock reaction in the mantle: Mantle troctolites from the Parece Vela ancient back-arc spreading center, *J. Petrol.*, *54*(5), 861–885.
- Sanfilippo, A., R. Tribuzio, and M. Tiepolo (2014), Mantle–crust interactions in the oceanic lithosphere: Constraints from minor and trace elements in olivine, *Geochim. Cosmochim. Acta*, *141*, 423–439.
- Saper, L., and Y. Liang (2014), Formation of plagioclase-bearing peridotite and plagioclase-bearing wehrlite and gabbro suite through reactive crystallization: An experimental study, *Contrib. Mineral. Petrol.*, *167*(3), 1–16.
- Sauter, D., et al. (2013), Continuous exhumation of mantle-derived rocks at the Southwest Indian Ridge for 11 million years, *Nat. Geosci.*, *6*(4), 314–320.
- Schindwein, V., and F. Schmid (2016), Mid-ocean-ridge seismicity reveals extreme types of ocean lithosphere, *Nature*, *535*, 276–279.
- Seyler, M., M. Cannat, and C. Mével (2003), Evidence for major-element heterogeneity in the mantle source of abyssal peridotites from the Southwest Indian Ridge (52° to 68°E), *Geochem. Geophys. Geosyst.*, *4*(2), 9101, doi:10.1029/2002GC000305.
- Seyler, M., J. P. Lorand, H. J. Dick, and M. Drouin (2007), Pervasive melt percolation reactions in ultra-depleted refractory harzburgites at the Mid-Atlantic Ridge, 15°20' N: ODP Hole 1274A, *Contrib. Mineral. Petrol.*, *153*(3), 303–319.
- Seyler, M., D. Brunelli, M. J. Toplis, and C. Mével (2011), Multiscale chemical heterogeneities beneath the eastern Southwest Indian Ridge (52°E–68°E): Trace element compositions of along-axis dredged peridotites, *Geochem. Geophys. Geosyst.*, *12*, Q0AC15, doi:10.1029/2011GC003585.
- Shaw, D. M. (2000), Continuous (dynamic) melting theory revisited, *Can. Mineral.*, *38*(5), 1041–1063.
- Smith, D. K., and J. R. Cann (1999), Constructing the upper crust of the Mid-Atlantic Ridge: A reinterpretation based on the Puna Ridge, Kilauea Volcano, *J. Geophys. Res.*, *104*(B11), 25,379–25,399.
- Sobolev, A. V., et al. (2007), The amount of recycled crust in sources of mantle-derived melts, *Science*, *316*(5823), 412–417.
- Spiegelman, M., and P. B. Kelemen (2003), Extreme chemical variability as a consequence of channelized melt transport, *Geochem. Geophys. Geosyst.*, *4*(7), 1055, doi:10.1029/2002GC000336.

- Standish, J. J., H. J. Dick, P. J. Michael, W. G. Melson, and T. O'Hearn (2008), MORB generation beneath the ultraslow spreading Southwest Indian Ridge (9–25°E): Major element chemistry and the importance of process versus source, *Geochem. Geophys. Geosyst.*, *9*, Q05004, doi:10.1029/2008GC001959.
- Suhr, G. (1999), Significance of upper mantle hosted dunite bodies for melt migration and extraction under oceanic spreading centres: Inferences from reactive transport modelling, *J. Petrol.*, *40*, 575–599.
- Suhr, G., E. Hellebrand, K. Johnson, and D. Brunelli (2008), Stacked gabbro units and intervening mantle: A detailed look at a section of IODP Leg 305, Hole U1309D, *Geochem. Geophys. Geosyst.*, *9*, Q10007, doi:10.1029/2008GC002012.
- Tartarotti, P., S. Susini, P. Nimis, and L. Ottolini (2002), Melt migration in the upper mantle along the Romanche Fracture Zone (Equatorial Atlantic), *Lithos*, *63*(3), 125–149.
- Toomey, D. R., S. C. Solomon, and G. Purdy (1988), Microearthquakes beneath Median Valley of Mid-Atlantic Ridge near 23°N: Tomography and Tectonics, *J. Geophys. Res.*, *93* (B8), 9093–9112.
- Tormey, D. R., T. L. Grove, and W. B. Bryan (1987), Experimental petrology of normal MORB near the Kane Fracture Zone: 22–25°N, mid-Atlantic ridge. *Contributions to Mineralogy and Petrology*, *96*(2), 121–139.
- Tursack, E., and Y. Liang (2012), A comparative study of melt-rock reactions in the mantle: Laboratory dissolution experiments and geological field observations, *Contrib. Mineral. Petrol.*, *163*(5), 861–876.
- Van Acherberg, E., C. G. Ryan, S. E. Jackson, and W. Griffin (2001), Data reduction software for LA-ICP-MS, in *Laser Ablation ICP-MS in the Earth Science*, vol. 29, edited by P. Sylvester, pp. 239–243, Mineral. Assoc. of Can.
- Warren, J. M., and N. Shimizu (2010), Cryptic variations in abyssal peridotite compositions: Evidence for shallow-level melt infiltration in the oceanic lithosphere, *J. Petrol.*, *51*(1–2), 395–423.
- Wolfe, C. J., G. M. Purdy, D. R. Toomey, and S. C. Solomon (1995), Microearthquake characteristics and crustal velocity structure at 29° N on the Mid-Atlantic Ridge: The architecture of a slow spreading segment, *J. Geophys. Res.*, *100*(B12), 24,449–24,472.
- Workman, R. K., and S. R. Hart (2005), Major and trace element composition of the depleted MORB mantle (DMM), *Earth Planet. Sci. Lett.*, *231*(1), 53–72.